ZHANG, WENDI, Ph.D. Carbon Nanodots (CNDs): A Comprehensive Study of the Photoluminescence, Antioxidation and Cellular Uptake (2019)
Directed by Dr. Jianjun Wei. 138 pp.

Carbon Nanodots (CNDs) have attracted increasing attention owing to their excellent photoluminescence properties, antioxidation activity, lower toxicity and superior water solubility. These physiochemical properties make CNDs promising candidates for biomedical applications including bioimaging, antioxidative agent and drug delivery, etc. However, the lack of consistency of understanding the fluorescence emission and antioxidation reactions in CNDs impedes their practical development in biomedical applications. Moreover, for CNDs cellular uptake study, there are rare reports on the nucleus penetrability of CNDs. Most uptake mechanisms focus on different types of nanoparticles (e.g. metal NPs or quantum dots). Little is known about the cellular uptake of CNDs especially the concentration influence. This dissertation research attempts to address these issues focusing on three aspects. (1) A new approach combining fluorescence spectroscopy and electrochemistry and energy gap analysis are used to investigate the photoluminescence mechanism of CNDs. (2) Electrochemistry and spectroscopy measurement are performed to investigate the antioxidative activities of CNDs against free radical DPPH• and reactive oxygen species (ROS) generated by xanthine/xanthine oxidase (XO) reaction. (3) nucleus penetrability of CNDs cell uptake is investigated with respect to CNDs' concentration. We found that the excitation dependent fluorescence of the CNDs may be attributed to multiple energy gap levels arising from a combination of the Sp2 carbon core, surface functionalities (C=O, C–O, and COOH), and surface electronic state transitions. Regarding the antioxidative property, the result of

electrochemical study for DPPH• scavenging is consistent with UV-Vis absorbance dose dependent manner following a coupled hydrogen atom transfer (HAT) reaction mechanism by the CNDs. For the cellular uptake of CNDs, a three-stage mechanism is proposed to explain the observation of concentration-dependent behavior of the nucleus penetrability. Overall, this comprehensive study of the photoluminescence, antioxidation and cellular uptake of CNDs and the findings should aid future development of practical utilization in bioimaging, antioxidation and drug delivery, such as i*n-vitro* and *in-vivo* studies.

CARBON NANODOTS (CNDs): A COMPREHENSIVE STUDY OF THE PHOTOLUMINESCENCE, ANTIOXIDATION AND CELLULAR UPTAKE

by

Wendi Zhang

A Dissertation Submitted to
the Faculty of The Graduate School at
The University of North Carolina at Greensboro
in Partial Fulfillment
of the Requirements for the Degree
Doctor of Philosophy

Greensboro
2019

Approved by

Jianjun Wei
Committee Chair

APPROVAL PAGE

This dissertation written by Wendi Zhang has been approved by the following committee of the Faculty of The Graduate School at The University of North Carolina at Greensboro.

Committee Chair	Jianjun Wei
Committee Members	Joseph M. Starobin
	Dennis R. LaJeunesse
	Zhenquan Jia

_____
Date of Acceptance by Committee

02/28/2019
Date of Final Oral Examination

ACKNOWLEDGEMENTS

Firstly, I would like to express my wholehearted gratefulness to Dr. Jianjun Wei, my advisor for his persistent support of my Ph.D. study and research. Not only a great research advisor and educator, but also a mentor for giving lots of thoughtful advice for my study and life.

I would like to thank the rest of my thesis committee and other teachers. Dr. Dennis LaJeunesse, Dr. Joseph Starobin, Dr. Zhenquan Jia, not only for their sharing extensive knowledge in the field but also their insightful guidance and encouragement for expanding my research from various viewpoint. Dr. Daniel Herr and Dr. Shyam Aravamudhan for their guidance over the years.

I also want to thank all my senior lab mates and collaborators, Dr. Zheng Zeng now at Central South University and Dr. Yiyang Liu now at Zhengzhou University, not only for the collaborative work, but also for their help in my study from the very beginning in JSNN. In addition, I thank Dr. Bloom Brain for XPS measurement and Dr. David Waldeck for collaborations on carbon nanodots characterization from the University of Pittsburgh.

I am thankful to all my group members, I am grateful to have these lovely people as my lab mates and work with them, Dr. Taylor Mabe, Harish Chevva, Alex Sheardy, Durga Arvapalli, Zuowei Ji, Bhawna Bagra, Kokougan Allado, Ziyu Yin, Anitha Jayapalan and Mengxin Liu. I am looking forward to hearing every success in their research.

Special thanks to my family, my parents and my grandmother with their limitless love, encouragement and support.

Overall, I am thankful and proud to be a member at JSNN. The time I spent here is my most wonderful possession.

TABLE OF CONTENTS

Page

LIST OF TABLES

Page

LIST OF FIGURES

Page

CHAPTER I

INTRODUCTION

A lot of efforts have been put into novel carbonaceous nanomaterials study. Two dimensional carbonaceous nanomaterials including graphene and graphene quantum dots (GQDs),[1,2] One dimensional nanomaterial like cylindrical carbon nanotubes (CNTs)[3-5] and zero dimensional graphitic nanomaterials such as fullerene [6,7]and nanodiamond [8,9] have been broadly explored in last few years. However, these nanomaterials may exhibit some disadvantages in their high preparation cost, insufficient biocompatibility, poor water solubility and photoluminescence properties. [10-13]

CNDs are reported to be composed of polyatomic carbon domains surrounded by amorous carbon frames and have been prepared by chemical ablation, electrochemical carbonization, laser ablation, hydrothermal/ solvothermal treatment, and microwave irradiation techniques.[14,15] There is continued interest in CNDs because of their physicochemical properties of good solubility, low toxicity, and biocompatibility, along with their favorable optoelectronic properties of strong fluorescence, phosphorescence, chemiluminescence, and photoinduced electron transfer.[15-19] As such, CNDs have been found to have potential applications in biomedicine (bioimaging, biosensor, and biomedicine delivery system), chemical sensing, and photoelectric devices (solar cells, supercapacitors, photocatalysis and light-emitting devices).[15-17] My research is aimed to investigate the optoelectronic properties and antioxidation activity of CNDs in the opto-

electrochemical-biological system and this study should aid their development for the practical use in chemical sensing, photoelectric devices and biomedicine.

Photoluminescence study: CNDs usually display a strong UV-Vis absorbance and photoluminescence effect which may vary due to CNDs' surface state properties and size, occurring with many different synthetic routes used in their preparation. A variety of CNDs have the excitation-dependent photoluminescence properties. Pan et al. reported the excitation-dependent blue carbon nanoparticles synthesized by a one-step pyrolytic route with high quantum yield at 31.6%-40.6%.[20] In addition, some researchers also prepared the excitation independent carbon nanoparticles. Wang et al. reported one type of excitation independent carbon dots which can emit different color at different solvent solution.[21] Jiang's group developed the excitation independent carbon nanoparticles by the hydrothermal method with high quantum yield of 68%. [22]Moreover, the surface charge and pH value also play significant effects on the photoluminescence property and intensity of carbon nanoparticles.[23,24] Although much work has been operated to investigate the mechanism of fluorescence properties of CNDs, the explanations lack consistency and the underlying mechanisms are not fully understood. To get a better understanding of the fluorescence properties of CNDs, in this section, we investigated the optoelectronic properties of CNDs by a fluorescence-electrochemical study and analyzed the energy gap of CNDs by experimental measurements and theoretical calculation. First, a type of CNDs(U-dots) was prepared by the microwave assisted irradiation and followed by a series of characterization such as TEM and AFM for size identification, FTIR for surface functional groups recognition, XRD for crystal structure exploration and so on.

Ferricyanide can quench the fluorescence of U-dots and ferrocyanide doesn't have this phenomenon. To better understand this phenomenon, we coupled the electrochemistry work station and fluorescence spectrophotometer together to study the effect of redox couple (ferricyanide and ferrocyanide) on the fluorescence intensity of U-dots and investigate the redox reactions by the cyclic voltammetry simultaneously. The optoelectronic properties of U-dots were also inspected by examining the wavelength dependent photocurrent generation from immobilized U-dots-gold slide system via this novel fluorescence-based spectroelectrochemical technique. Moreover, the energy gap of U-dots was studied by three different methods such as optical band gap measurement, electrochemical HUMO-LUMO energy gap analysis and Hückel model for electronic energy level calculation. This fluorescence-electrochemical study and energy gap investigation provide a new perspective to understand the excitation-dependent fluorescence property which results from a combination of conjugated π states (C=C) with the functional groups (C=O, C-O, and COOH) associated with the surface electronic states. In all, this part study should facilitate CNDs development for practical use in biomedicine, chemical sensing, and photoelectric devices.

Antioxidation study: Besides the excellent biocompatibilities, CNDs can also work as electron either electron donors and electron acceptor which should facilitate their potential application as antioxidant agent.[25]This section is oriented to investigate the antioxidation capacity of CNDs by examining optical changes, radical-electrode electron transfer reaction as well as enzyme generated reactive oxygen species (ROS) scavenging. At first, we performed optical measurement and electrochemical study of the microwave

synthesized nitrogen doped CNDs (U-dots). During this study, we tested UV-Vis absorbance changes of 2,2-diphenyl-1picrylhydrazyl radical (DPPH•) to evaluate the antioxidation activity of U-dots. DPPH• has UV-Vis absorbance at 517 nm, when it reacts with antioxidant, the optical absorbance at this wavelength can decrease. Based on this principle, we performed optical study and demonstrated that the antioxidation property of microwave synthesized U-dots showed a dose dependent manner. However, the relationship between reserved DPPH• concentration and U-dots' incubated concentration is unclear. To solve this problem, then we utilized electrochemical measurement on the changes of redox peaks of the oxidation of DPPH• at gold electrodes with addition of different concentrations of a type of microwave-synthesized U-dots. Combined with standard heterogeneous electron-transfer rate constant analysis, electrochemical study gives a coupled hydrogen atom transfer (HAT) mechanism for DPPH• scavenging by the U-dots. This work provides a new perspective on the antioxidative study of the U-dots, which may aid their development for practical use in biomedicine. After this study, we prepared nitrogen and sulfur (N, S-) codoped CNDs by the hydrothermal method and performed a comprehensive study for exploring their antioxidation capacity using UV−vis absorption and electrochemistry measurements of 2,2-diphenyl-1-picrylhydrazyl radical (DPPH•), as well as a lucigenin chemiluminescence (lucigenin-CL) assay. Combined with the biocompatibility and bioimaging capabilities, these results provide promise for the development of alternative treatment options not possible with traditional pharmacological and ROS scavenger

approaches, suggesting a new “nanopharmacology” for more effective treatment of inflammatory disorders such as atherosclerosis.

Cellular uptake study: The tunable photoluminescence properties and good biocompatibilities make CNDs excellent candidates for bioimaging and drug delivery application. A lot of research has been performed. For example, Prato’s group coupled nitrogen-doped carbon nanodots with anticancer drug paclitaxel for bioimaging and drug carrier application.[26] Kuo et al. synthesized fluorescent nitrogen-doped carbon nanodots by the hydrothermal method and investigated their potential application in vivo bioimaging.[27] Chizhik et al. produced the dual-color fluorescent carbon nanodots and explored their potential utilization as nucleus label.[28]Although a lot of efforts have been made to investigate CNDs for biomedicine applications, it is lack of comprehensive understanding of how CNDs enter and leave the cells. And moreover, rare reports focused on the nucleus penetrability of nanoparticle and most uptake mechanisms are focused on the size, surface properties and morphology of the nanoparticle. In this section, the interaction between CNDs and cell nucleus were thoroughly studied by the dark field microscopy coupled with hyperspectral microscopy. The key is to quantitively determine the light signals of CNDs inside the cell nucleus by the hyperspectral microscopy. In this study, the concentration of incubated CNDs and incubation time played significant roles on the CNDs cellular uptake process. Moreover, the nucleus penetration process displayed a three-stage concentration-dependent manner and the analytical model was also established based on these results. With a halfway incubation concentration of 2.68 mg/mL, the three-stage mechanism was reported including the first

stage of CNDs penetration on the nuclear side boundary layer, the second stage of importins transportation, and the third stage of cessation of CNDs penetration into the nucleus.

References

1. Dinari M, Momeni MM, Goudarzirad M. J Mater Sci., 2016, 51:2964–2971.
2. Zubair M, Mustafa M, Ali A, Doh YH, Choi KH. J Mater Sci: Mater Electron, 2015, 26:3344–3351.
3. De Volder MFL, Tawfick SH, Baughman RH, Hart AJ. Science., 2013, 339:535–539
4. Wang Z, Yin L, Zhang M et al. J Mater Sci., 2014, 49:1585–1593.
5. Rud J, Lovell L, Senn J, Qiao Q, Mcleskey J Jr. J Mater Sci., 2005, 40:1455–1458.
6. Guldi DM, Illescas BM, Atienza CM, Wielopolskia M, Martin N. Chem Soc Rev., 2009 38:1587–1597
7. Liu J, Rinzler AG, Dai H et al. Science., 1998, 280:1253–1256
8. Laraoui A, Hodges JS, Meriles CA. Nano Lett., 2012, 12:3477–3482
9. Yu M, George C, Cao Y, Wootton D, Zhou J. J Mater Sci., 2014, 49:3629–3641.
10. P. C. Hsu, Z. Y. Shih, C. H. Lee and H. T. Chang, Green Chem., 2012, 14, 917–920.
11. S. Chandra, S. H. Pathan, S. Mitra, B. H. Modha, A. Goswami and P. Pramanik, RSC Adv., 2012, 2, 3602– 3606.
12. M. M. Liu and W. Chen, Nanoscale., 2013, 5, 12558–12564.
13. S. N. Baker and G. A. Baker, Angew. Chem., Int. Ed., 2010, 49, 6726–6744.
14. S. Zhu, Q. Meng, L. Wang, J. Zhang, Y. Song, H. Jin, K. Zhang, H. Sun, H. Wang and B. Yang, Angewandte Chemie International Edition., 2013, 52, 3953-3957.
15. S. Y. Lim, W. Shen and Z. Gao, Chemical Society Reviews., 2015, 44, 362-381.
16. X. T. Zheng, A. Ananthanarayanan, K. Q. Luo and P. Chen, *Small*, 2015, **11**, 1620-1636.
17. Y. Wang and A. Hu, Journal of Materials Chemistry C, 2014, 2, 6921-6939.
18. X. Li, M. Rui, J. Song, Z. Shen and H. Zeng, Advanced Functional Materials, 2015, 25, 4929-4947.

19. Q. Xu, J. Wei, J. Wang, Y. Liu, N. Li, Y. Chen, C. Gao, W. Zhang and T. S. Sreeprased, RSC Advances, 2016, 6, 28745-28750.

20. Pan, L., Sun, S., Zhang, A., Jiang, K., Zhang, L., Dong, C., ... & Lin, H. 2015, Advanced materials, 27(47), 7782-7787.

21. Wang, H., Sun, C., Chen, X., Zhang, Y., Colvin, V. L., Rice, Q., ... & William, W. Y. (2017). Nanoscale, 9(5), 1909-1915.

22. Guo, Y., Wang, Z., Shao, H., & Jiang, X. (2013). Carbon, 52, 583-589.

23. Pan, D., Zhang, J., Li, Z., Wu, C., Yan, X., & Wu, M. (2010). Chemical Communications, 46(21), 3681-3683.

24. Xu Q, Pu P, Zhao JG et al. J Mater Chem A.,2015, 3:542–546

25. Wang, J., & Qiu, J. Journal of materials science, 2016, 51(10), 4728-4738.

26. Gomez, I. J., Arnaiz, B., Cacioppo, M., Arcudi, F., & Prato, M. Journal of Materials Chemistry B., 2018, 6(35), 5540-5548.

27. Kuo, T. R., Sung, S. Y., Hsu, C. W., Chang, C. J., Chiu, T. C., & Hu, C. C. Analytical and bioanalytical chemistry., 2016, 408(1), 77-82.

28. Chizhik, A. M., Stein, S., Dekaliuk, M. O., Battle, C., Li, W., Huss, A., ... & Schmidt, C. F. Nano letters, 2015, 16(1), 237-242.

CHAPTER II

FLUORESCENCE-ELECTROCHEMICAL STUDY OF CARBON NANODOTS (CNDS) IN BIO- AND PHOTOELECTRONIC APPLICATIONS AND ENERGY GAP INVESTIGATION

This chapter has been published as: Zeng, Z., Zhang, W., Arvapalli, D. M., Bloom, B., Sheardy, A., Mabe, T., & Wei, J. (2017). A fluorescence-electrochemical study of carbon nanodots (CNDs) in bio-and photoelectronic applications and energy gap investigation. Physical Chemistry Chemical Physics, 19(30), 20101-20109.

Introduction

To explain the mechanism of light emission in CNDs,[1,2] some workers have proposed that the bandgap transitions responsible for fluorescence arise from conjugated p-domains consisting of sp2 hybridized islands rich in p-electrons, bond disorder induced energy gaps,[3,4] or giant red-edge effects that give rise to strong excitation wavelength dependent fluorescence.[5,6] These mechanisms are similar to those used to understand the emissive properties of single-layer graphene and graphene oxides.[7,8] Other workers ascribe the light emission characteristics to quantum confinement effects,[9] size dependent optical properties,[10] surface-related defect sites,[11] and radiative recombination of excited surface states.[12] A poor understanding of the structure of CNDs in terms of their functional groups, defects, adsorbates, and electronic structure continues to impede the development of an agreed upon mechanism.

This work uses a new combined fluorescence-electrochemical approach to investigate the optoelectronic properties of CNDs. Although numerous spectroelectrochemical techniques have been developed, such as electrochemical fluorescence spectroscopy,[13,14] electrochemical surface/tip-enhanced Raman spectroscopy,[15,16] and ultraviolet-visible (UV-Vis) absorption spectroelectrochemistry,[17,18] the simultaneous study of fluorescence and electrochemical measurements which focus on the effect of chemically reversible reactions on CNDs is rare. Here, water-soluble luminescent CNDs were synthesized by a simple one-step microwave route and were characterized by transmission electron microscopy (TEM), atomic force microscopy (AFM), X-ray photoelectron spectroscopy (XPS), Fourier transform infrared spectroscopy (FTIR), Raman spectroscopy, X-ray powder diffraction (XRD), UV-Vis spectroscopy, fluorescence spectroscopy, pH dependent zeta potential measurements, and quantum yield measurements. Their potential application in bioimaging was assessed from their excitation dependent fluorescence, and their potential use as chemiluminescent sensors was evaluated by examining the effect of the ferricyanide/ferrocyanide redox couple on their fluorescence spectrum. We also examined the excitation wavelength dependence of the photocurrent (action spectrum) generated by CNDs that were immobilized on gold slide electrodes to assess their potential application in photoelectric devices. Optical and electrochemical measurements were used to measure the energy gap of the CNDs, and Hückel level calculations of the HOMO (highest occupied molecular orbital) and LUMO (lowest unoccupied molecular orbital) were fitted to the energy gap measurements by treating a CND as a molecule.

Methods and Materials

Synthesis of CNDs: A microwave assisted synthesis of CNDs was performed using citric acid and urea as precursors.[19] Briefly, 1.0 g of urea (Aldrich) and 1.0 g of citric acid (ACROS Organics) were simultaneously added to 1.0 mL of deionized water to form a homogeneous solution and then heated in a microwave synthesizer (CEM Corp 908005 Microwave Reactor Discovery System) at a power of 150 W for 12 minutes. After cooling, the aqueous reactant mixture was purified using a centrifuge (Solvall Legend XFR Floor Model Centrifuge) at 3500 r/min for 20 min to remove large and aggregated particles. The dark-brown solution was further purified using a dialysis membrane (Scientific Fisher) with a molecular weight cut off of 1000 Da for 24 hours. To obtain the solid sample, the resulting solution was finally dried with a freeze dryer (Labconco Free Zone 6 Freeze Dryer) for 24 hours.

CNDs Characterization: Atomic force microscope (AFM, Agilent Technologies 5600 LS Series) and transmission electron microscopy (TEM, Carl Zeiss Libra 120 Plus) were used to study the size of the CNDs. Fourier transform infrared spectroscopy (FTIR, Varian 670), Raman spectroscopy (Horiba XploRA One Raman Confocal Microscope System), X-ray photoelectron spectroscopy (XPS, Thermo Fisher ESCALAB 250 Xi), and X-ray powder diffraction (XRD, Agilent Technologies Oxford Gemini) were used to determine the elemental composition and chemical structure of the CNDs. A Zetasizer nano-ZX (Malvern Instruments ZEN3600) was used to study the stability of the CNDs as a function of pH (Fisher Scientific pH 2100). Ultraviolet-visible spectroscopy (UV-Vis

spectroscopy, Varian Cary 6000i) and fluorescence spectroscopy (Varian Cary Eclipse) were used to investigate the absorbance and fluorescence properties of the CNDs, respectively.

Cell Culture and Bioimaging: HepG2 cells were obtained from American Type Culture Collection (ATCC) and cultured in an Eagle's Minimum Essential Medium [2 mM L-glutamine, 1 mM sodium pyruvate, and 1500 mg/L sodium bicarbonate] (ATCC) containing 10% Fatal Bovine Serum (Fisher Scientific, USA), 1% antibiotic with 100 UI/mL Penicillin and 100 µg/mL Streptomycin (Fisher Scientific, USA). The cells were incubated in a humidified incubator with 5% CO_2 at 37°C. Trypsin/EDTA (Fisher Scientific, USA) was used to passage the cells serially. The cells were seeded (150,000 cells/dish) in petri dishes with cover slips in the dish. After culturing for 24 hours, the cells were treated with CNDs at a concentration of 0.3 mg/mL. Untreated cells without CNDs were used as a control. The cells were imaged using a confocal microscope (Carl Zeiss Libra 120 Plus Z1) by mounting the cover slips onto the glass slides. All the images were taken at 10X magnification and at a scale bar of 20 µm.

Fluorescence Spectroelectrochemistry: The electrochemical-fluorescence technique comprises a Bio-logic VMP3 electrochemical workstation with a two-electrode testing system (a platinum wire as the counter electrode and a gold electrode for the fluorescence spectroelectrochemistry experiment (Fisher Scientific) as the working electrode (replaced by immobilized CNDs gold slide electrode for the photocurrent generation experiment) and the fluorescence spectrophotometer (the excitation wavelength could be varied from 200-700 nm by using a 450 W xenon lamp with an

excitation monochromator (the area of illumination is about 5 mm in diameter) and emission could be collected from 300-1000 nm by an emission monochromator, Agilent).

Preparation of Immobilized CNDs at Gold Slide Electrode Surfaces: The gold coated slides (20 nm Au deposited on 8 mm×8 mm glass slide by Physical Vapor Deposition (Kurt Lesker PVD75 E-Beam Evaporator System) were first cleaned with O_2 plasma (South Bay Technologies PC2000 Plasma Cleaner) for 15 minutes. The slides were then incubated in a mixture of 1 mM 11-mercaptodecanoic acid (HSC10COOH, Aldrich) and 8-mercapto-octanol (HSC8OH, Aldrich) in an absolute ethanol solution (ACROS Organics) with 1:5 mole ratio overnight to form a self-assembled monolayer (SAM) by alkyl thiols. After SAM formation, the gold slides were incubated in a 0.5 mM 1-(3-dimethylaminopropyl)-3-ethylcarbodiimide hydrochloride (EDC, TCI)/ N-hydroxysuccinimide (NHS, Aldrich) for 2 hours to activate the carboxylic acid groups.[20, 21]Next, the gold slides were rinsed with deionized water and immediately moved to a freshly prepared 3 mL solution containing 0.3 mg/mL of CNDs for 2 hours. The gold slides were rinsed with deionized water and dried before experiments.

Energy Gap and Molecular Orbital Energy Level Calculation: The optical band gap was determined using an indirect band gap calculation.[22] The UV-Vis absorption spectrum calculation was processed by plotting $\sqrt{Ah\nu}$ versus $h\nu$, where A is the measured absorbance, h is the Plank constant, ν is the frequency, and $h\nu$ is equal to 1240/wavelength in unit of eV. $\sqrt{Ah\nu}$ has a linear relationship with $h\nu$ with a slope of D and the optical band gap is the x-intercept. Cyclic voltammetry (CV) was used to obtain the HOMO and LUMO energy levels of the CNDs.[23] The electrochemical measurement

was performed using a three-electrode electrochemical cell with a gold working electrode, a Ag/AgCl reference electrode, and a platinum counter electrode (Fisher Scientific) in a 4.0 mL acetonitrile (Fisher Scientific) solution containing 0.1 M tetrabutylammonium hexafluorophosphate (Fisher Scientific) as the supporting electrolyte and 1 mL of deionized water containing 0.3 mg CNDs. Cyclic voltammetry of the sample was run at a scan rate of 100 mV/s under room temperature. The electrochemical data were used to determine the HOMO and LUMO energy levels; namely, $E_{HOMO} = -(E_{onset,ox}+4.66)eV$, and $E_{LUMO}=-(E_{onset,red}+4.66)eV$, where $E_{onset,ox}$ and $E_{onset,red}$ are the onset of the oxidation and reduction potentials,[23] respectively (Note that the formal potential of the Fc+/Fc redox couple was estimated as -5.06 eV in the Fermi scale when the formal potential of the Fc+/Fc redox is 0.40 V versus Ag/AgCl. See details in supplementary information). The Hückel method was used to reproduce the energy gap by assuming a molecular structure of CNDs and adjusting the coulomb and resonance integral values to obtain a HOMO-LUMO gap that is consistent with the energy gap values obtained from the spectral and electrochemical measurements.[24] These parameters were used to calculate the different molecular orbital energy levels.

Results and Discussion

CND synthesis and characterization: A one-step microwave route was used to synthesize CNDs from citric acid and urea.[19] Transmission electron microscopy (Fig 2.1A) and atomic force microscopy (Fig. 2.1B), indicate that the CNDs are spherical and well dispersed, and have an average size of about 3 nm. FTIR spectra of the CNDs (Fig

2.1C) display broad bands at 3100–3400 cm^{-1} which are assigned to ν(O-H) and ν(N-H); functionalities that help explain the hydrophilicity and stability of the CNDs in aqueous media. The IR transitions at 768, 1184, 1402 and 1566 cm^{-1} are assigned to ν(C-C), ν(C-O), ν(C=C) and ν(C=O), respectively.[25] The presence of these functionalities at the surfaces is corroborated by XPS data (Fig 2.1D) of the CNDs, which could be fitted by four components: C=C & C-C (49.8%, 284.8 eV), C=O (36.6%, 287.8 eV), C-O (7.3%, 286.5 eV), and COOH (6.3%, 289.0 eV). Raman spectra of the CNDs (Fig 2.1E) show both D bands at 1341 cm^{-1} (sp3-hybridized) and G bands at 1564 cm^{-1} (sp2-hybridized) with an intensity ratio ID/IG of about 1.06, suggesting the presence of a disordered graphite structure.[26,27] The main diffraction peak in the XRD spectrum (Figure 2.1F) appears at 25.2° with a full width at half maximum (FWHM) of about 3.2°, which corresponds to an interlayer distance of 0.35 nm between the planar carbon based sheets for the graphite structure region.[28] In summation, the structure of the CNDs in this study is spheroidal with an average size of 3 nm and consists of a disordered graphite structure with surrounding amorphous carbon frames and functional groups on the surfaces. Fig 2.1G shows the absorption spectrum of the CNDs over the spectral range of 200 to 600 nm. There is no obvious absorption feature found above 600 nm. A shoulder/peak in the spectrum at about 236 nm is consistent with π-π* transitions of C-C and C=C bonds in sp^2 hybrid regions and the main peak at 331 nm is consistent with n–p* transitions of the C=O moieties.[29,30] The emission of the CNDs occurs over a spectral region from 400 nm to wavelengths longer than 600 nm (see Fig 2.2A). Other than the lack of well-defined

vibronic structure, these spectra are consistent with that expected for large π-conjugated catacondensed hydrocarbons.

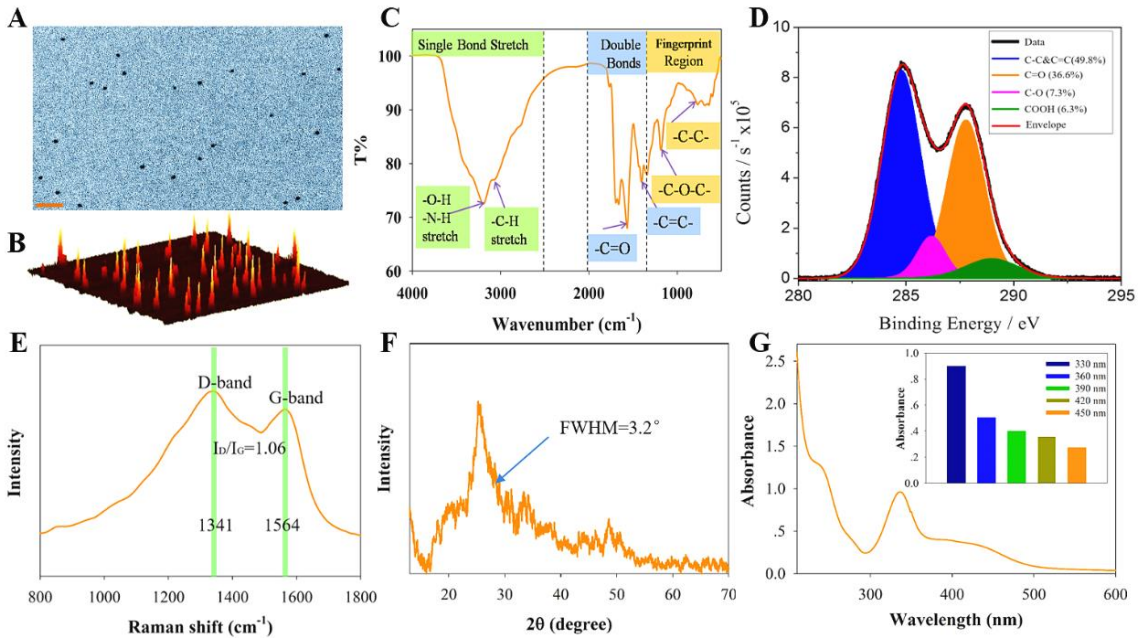

Figure 2.1 CNDs Characterization. The CNDs are characterized using different techniques: A) transmission electron micrograph (scale bar is 20 nm), B) atomic force microscopy profile of CNDs distributed on a mica surface, C) Fourier transform infrared spectrum, D) X-ray photoelectron spectrum (C1 signal), E) Raman spectrum, F) X-ray diffraction data, and G) UV-Vis absorption spectrum of CNDs.

CND fluorescence and cell imaging: CNDs can act as blue/green fluorophores in imaging applications.[31] Figure 2A shows the fluorescence emission spectra of the synthesized CNDs in deionized water at five different excitation wavelengths (λ_{ex}=330, 360, 390, 420, and 450 nm). The maximum emission intensity occurs with 360 nm excitation and has a peak emission at 454 nm. The apparent red-shift in the photoluminescence spectra with changing excitation wavelength is in agreement with other reports.[32,33] The potential application of CNDs as a bioimaging agent is confirmed

by the uptake of fluorescent CNDs by HepG2 cells.[34] Spinning disk confocal microscopy was used to monitor the cellular uptake phenomenon by HepG2 cells after treatment with CNDs for 24 hours (Figure 2.2). The strong blue and green fluorescence was consistent with a chromaticity coordinates calculation (CIE Chromaticity Diagram) that was performed after inputting the emission data obtained from excitation at 330 nm and 450 nm. These results suggest that the as-prepared CNDs are good candidates for use as cell imaging agents.

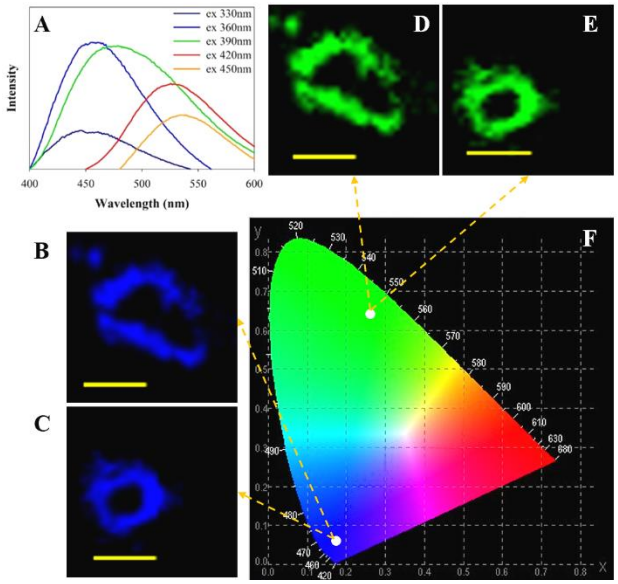

Figure 2.2. Fluorescence and Confocal Images. (A) Fluorescence emission spectra of CNDs in deionized water. (B, C) Confocal images of HepG2 cells that are cultured with CNDs (0.3 mg/mL) for 24 hours; taken at 330 nm excitation. All of the images have a scale bar of 20 µm. (D, E) Confocal images as in panels B and C, but with 450 nm excitation. (F) Calculation of chromaticity coordinates with the emission results under excitation wavelengths of 330 and 450 nm.

Fluorescence Spectroelectrochemistry: A ferricyanide/ferrocyanide redox couple was chosen as the redox probe for spectroelectrochemical measurements because it is a

reversible system with spectroscopically distinguishable redox forms.[35,36] Figure 2.3A shows cyclic voltammograms (CV) of a ferri-/ferrocyanide solution at scan rates of 10, 20, 50, and 100 mV/s. Figure 2.3B shows the fluorescence intensity of the CNDs solution (using 360 nm excitation) with increasing potassium ferricyanide ($K_3Fe(CN)_6$) concentration. At low concentrations (<33 μM) of $K_3Fe(CN)_6$ the fluorescence of the CNDs is not affected strongly; however, from 33 μM to 333 μM of $K_3Fe(CN)_6$, the fluorescence intensity of the CNDs decreases and the emission peak red-shifts. This fluorescence quenching can arise from two phenomena. The main one is arising from the reaction of CNDs with $Fe(CN)_6^{3-}$ ($CNDs+Fe(CN)_6^{3-} \rightarrow CNDs^*+Fe(CN)_6^{4-}$) which may influence the surface electronic state transitions caused by incomplete passivation. Since the energy gap of surface states is larger than that of the core states (details are shown in the energy gap calculation part) and smaller energy gap induces larger emission wavelength, hence, the red-shift of the fluorescence peaks present with increasing concentrations of $K_3Fe(CN)_6$.[37,38]

To record voltammograms for $K_4Fe(CN)_6$ and the concurrent, real-time influence of $K_3Fe(CN)_6$ on the fluorescence properties, a scan rate of 20 mV/s and 333 μM $K_4Fe(CN)_6$ were selected for the fluoro-electrochemical studies; see Figure 2.3C and 2.3D. Figure 2.3D shows the fluoroelectrochemical data for the redox cycling of ferrocyanide and ferricyanide. As the ferrocyanide is oxidized to ferricyanide near 0.45 V (vs. Ag/AgCl), the fluorescence peaks of the CNDs decrease (Figure 5D). In addition, the fluorescence peaks of the CNDs increase in the potential range from 0.45 to 0.2 V (vs. Ag/AgCl) on the reverse scan, suggesting the consumption of the electrogenerated

ferricyanide. In summary, these results demonstrate that the CNDs can be used as a chemiluminescence sensor for obtaining electrochemical properties using fluorescence spectrometry.

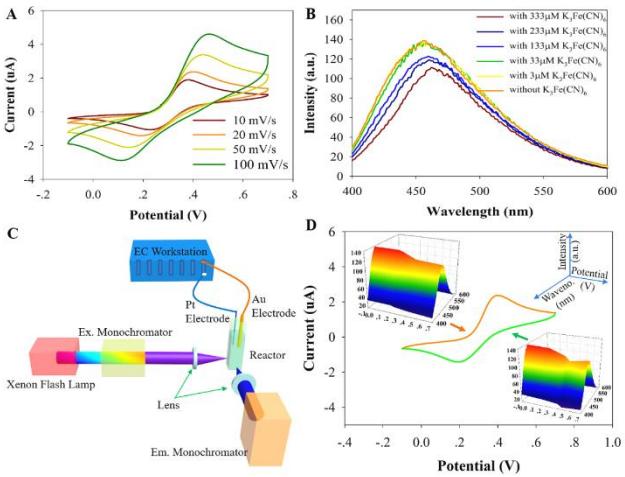

Figure 2.3. Fluorescence-Electrochemical Study. (A) Cyclic voltammogram (CV) of a mixture of 333 μM K4Fe (CN)6 and 0.1 M KCl solution between -0.1 V and 0.7 V at 10, 20, 50 and 100 mV/s scan rates. (B) Fluorescence spectrum of solution including 50 μg/mL CNDs and 0.1 M KCl after addition of K3Fe(CN)6 with different concentrations (3, 33, 133, 233, and 333 μM). (C) Schematic view of the setup used for coupling electrochemistry with a fluorescence spectrophotometer. (D) CV of 333 μM K4Fe (CN)6 in 0.1 M KCl between -0.1 V and 0.7 V at scan rate of 20 mV/s with the inserted three-dimensional spectra of fluorescence signal of CNDs during the CV experiment (solution includes 50 μg/mL CNDs, 333 μM K4Fe(CN)6, and 0.1 M KCl).

Photocurrent Generation from CNDs immobilized gold slide: The action spectrum of the CNDs immobilized on a gold slide electrode (Figure 2.4A) was obtained by measuring the photocurrent in a 3 mL 0.1 M Na_2SO_4 electrolyte solution under monochromatic light irradiation. The Na_2SO_4 based electrolyte solution was N_2-degassed before the photocurrent experiment. Figure 2.4B shows photocurrent measurements (at an applied voltage of 0.8 V) of the CNDs treated electrodes at five different irradiation

wavelengths. Note that the resulting current from the photo-excitation processes occurring at the electrode was monitored as a function of time by the CA measurement in which the potential of the working electrode from chronoamperometry is stepped, and after 50 seconds of the decay time from initial to steady-state current, we calculated the net photocurrent attributed by CNDs as Figure 2.4D shown by subtracting CA measurements with an applied voltage of 0.8 V of the gold slide electrode without CNDs immobilization from CA measurements of the gold slide electrode with CNDs immobilization before and after light irradiation with different incident wavelength (330-450 nm). The highest photocurrent (~2.5 μA) was obtained for an incident wavelength of 330 nm (corresponding to photon energy, E_e=3.76 eV) while the lowest photocurrent (~0.5 μA) was obtained for an incident wavelength of 450 nm (E_e=2.75 eV) (Figure 2.4C). Since no photocurrent was observed from the bare gold electrode under the irradation, the photocurrent action spectrum demonstrates that the CNDs are the photoactive species responsible for the photocurrent generation. Since the intensity of incident light is independent of its wavelength, the incident wavelength dependent photocurrent generation by CNDs may be arising from two likely factors. First is an increase in the incident photon to charge carrier efficiency that arises from higher light absorbance of CNDs at shorter wavelengths, as concluded from their absorption spectrum (Figure 2.1G insert),[39] and the second is the somewhat higher energy of the photoinjected electrons at shorter wavelengths.

In analogy to a semiconductor-electrolyte interface, CNDs generate electron-hole pairs (e^--h^+) that can then undergo various relaxation pathways, including electron-hole

pair radiative recombination, charge transfer to the substrate, and charge transfer to an acceptor in the electrolyte.[40-42] The photocurrent measured in this system, without a redox couple in solution, corresponds to a net electron transfer from the CNDs to the gold slide electrode; thus the photocurrent is anodic. Figure 2.4D shows that the voltage dependence of the photocurrent generated by the CNDs under excitation at 330 nm increases monotonically with increasing positive bias.

It was observed that photocurrent decays with time especially under the high energy incident light (330 nm) at high bias voltage (0.8V). To exam if there was a degradation of CND layer at the gold electrode, multiple photocurrent measurements were carried out at different times using the same electrode; no signifcant magnitude changes of the photocurrents were observed, suggesting the stability of the CND layer at the gold electrode. The decay of photocurrent with time (~ 50 s to get stable) may be attributed to the need for establishing an equilibriu satus of the semiconductor-electrolyte interface, because the higher energy light exciation, the more electron-hole pairs (e--h+) separation at the interface (coupling with a double layer capacitance behavior with an external electrical field) would take longer time to reach the equilibriu status for stable photocurrent generation. More insightful understanding (e.g. electron-hole pair generation and recombination, charge transfer, and analysis of mobilities in CNDs) of the photocurrent decay would be of great interest for a real photovoltaic device development, which, however, is beyond the scope of this study.

The increase in photocurrent at higher bias potentials can be explained using a Fowler-Nordheim model[43] for the photocurrent. In this model, the photocurrent is proportional to the following dimensionless tunnelling probability:[43]

$$I_p \propto \exp\left[-\frac{4}{3}\frac{\sqrt{2m^*}}{qh}\frac{\Phi_B^{3/2}L}{(V_0+\alpha V_a)}\right] \quad (1)$$

where I_p is the photocurrent, q is the electron charge, h is Planck's constant, m^* is the effective mass, ϕ_B is the tunnelling barrier height, V_0 is the open circuit voltage, αV_a is the fraction of the applied voltage across the barrier (thus affecting the electric field), and L is the length over which the electric field applies. Hence, higher applied bias voltages result in a higher photocurrent from the CNDs. The photoinduced excitation and subsequent charge transport to the gold slide electrode demonstrate the potential for CNDs to be used in photovoltaic and other optoelectronic device applications.

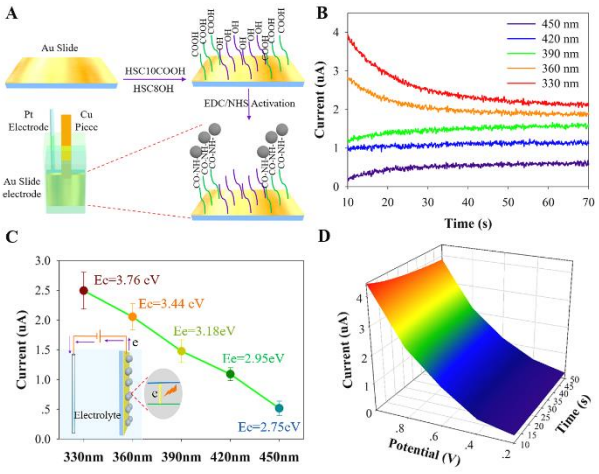

Figure 2.4. Photocurrent Generation. (A) Illustration of the protocol for the self-assembled monolayer (SAM) formation and CNDs immobilization on the gold slide

electrode. Note that the fluoro-electrochemical setup is the same as that in Figure 5C except the gold electrode was changed into the immobilized CNDs gold slide electrode which is electrically connected through a piece of copper tape. (B) Chronoamperometry (CA) photocurrent measurements of CNDs immobilized on the electrode at an applied voltage of 0.8 V. The different irradiation wavelengths are shown in the legend, ranging from 330-450 nm. (C) The long-time photocurrent of the CND films is plotted for the different incident wavelengths, with photon energy, $Ee=hc/\lambda$, indicated. The inset shows a schematic of photocurrent generation of CNDs upon excitation. (D) The chronoamperometry measurement with different applied bias potentials of the gold slide electrode with CNDs immobilization under an incident wavelength of 330 nm.

Energy Gap Investigation and Analysis: The electronic energy levels of the carbon atoms combine to form delocalized bands of energy states,[44] including a valence band maximum, (in analogy to HOMO), and conduction band minimum, (in analogy to LUMO). From the UV-Vis absorption spectrum (Figure 2.1G), the optical band gap E_o of the CNDs is estimated to be 2.13±0.06 eV (Figure 2.5A).[28] After adjusting for the exciton binding energy E_b (about 6.1-13.6 meV),[45, 46] the energy gap from the optical measurement is estimated to be about 2.12±0.06 eV. In addition, electrochemical measurements can be used to determine the HOMO and LUMO positions by treating an individual CND as a molecule. The onset of the reduction (E_{red}) and oxidation (E_{ox}) potentials for the CNDs give energies of -3.75±0.04 eV of LUMO energy level and -5.84±0.04 eV of HOMO energy level, respectively (Figure 2.5B, Fig S10). These values give an HOMO-LUMO energy gap for the CNDs of 2.09±0.08 eV,[23, 47] which is close to the energy gap value obtained from the spectral measurements.

The Hückel method[24] was used to calculate the molecular orbital levels, for common values of the coulomb and resonance integral values. The molecular structure of the CNDs (Figure 2.5C) was generated from a graphite structure surrounded by

amorphous carbon atoms and surface functional groups, which were chosen to correspond to the atomic ratio of C:O: N obtained by XPS. The core size was then increased until a HOMO-LUMO energy gap of 2.07 eV was reached. At the same given parameters, different orbital energy levels (LUMO+2, LUMO+1, LUMO, and HOMO, HOMO-1, HOMO-2) could be obtained).[24] The calculated LUMO (-3.71 eV) and HOMO (-5.78 eV) electronic state energies of the molecular CND are consistent with that obtained by the electrochemical experiments (about -3.75±0.04 and -5.84±0.04 eV).

The molecular orbital model has been applied to understand the fluorescence properties of graphene oxide nanodots previously,[48, 49] and the dominant fluorescence mechanism was found to originate from the electronic transitions among/between the non-oxidized carbon regions and the boundary of oxidized carbon atom regions involving the functionalized groups C-O, C=O and COOH. Compared to the graphene oxide quantum dots, previous studies indicate the CNDs have a less defined π-electron core and a larger proportion of functional groups, thus little quantum confinement effect on photoluminescence.[50] In this work, the π-core region of the CNDs is small, as determined from the XRD data, yet the CND size distribution is mostly uniform. The molecular orbital energy levels that are derived from Hückel theory show good agreement with the observed fluorescence of the CNDs between 400 nm (photo energy of 3.10 eV) and 600 nm (photo energy of 2.06 eV) (Figure 2.2A) which may correspond to the potential electronic transitions from LUMO to HOMO (gap of 2.07 eV), to HOMO-1 (energy difference of 3.92 eV), and to HOMO-2 (3.94 eV), and/or from LUMO+1 to HOMO (2.65 eV), and LUMO+2 to HOMO (2.66 eV). Here, the responsible atom groups include

non-oxidized carbon (C=C), the boundary oxidized carbon (C=O and C-O), and functionalized carbon (COOH), with electronic transition moments for C=C, C=O, C-O and O-H being 3.24 D, 2.93 D, 3.43 D and 2.30 D, respectively. Since the photoluminescence could be proposed to be proportional to the time constant and the number of electrons from high to low energy level, here, the Hückel model treatment combines the conjugated π states (C=C) with the functional groups (C=O, C-O, and O=C-OH), which can be dominant factors in the excitation-dependent emission of CNDs. Note that the electric vector is aligned parallel with (or perpendicular to) the transition moment of the bonds resulting in higher (or lower) light absorbance. This indirectly affects the electronic transition probability and photoluminescence properties.[48, 51] For the photoluminescence origin of amorphous CNDs, the light emission characteristics has been generally ascribed to surface-related defect sites, and radiative recombination of excited surface states.[50] In this study, based on the energy gap calculation and the observation of the fluorescence-based spectro-electrochemistry analysis, we propose that the photoluminescence arises from a combination of the C=C core regions, the surface functional groups (C=O, C-O, and COOH), and the surface electronic state transitions. However, the question regarding the effect of the C=C core-region, e.g. the size dependent quantum confinement, and its contribution to the origin of fluorescence from such microwave synthesized CNDs is open; and it may be explored by controlling the core sizes while maintaining the surface states.

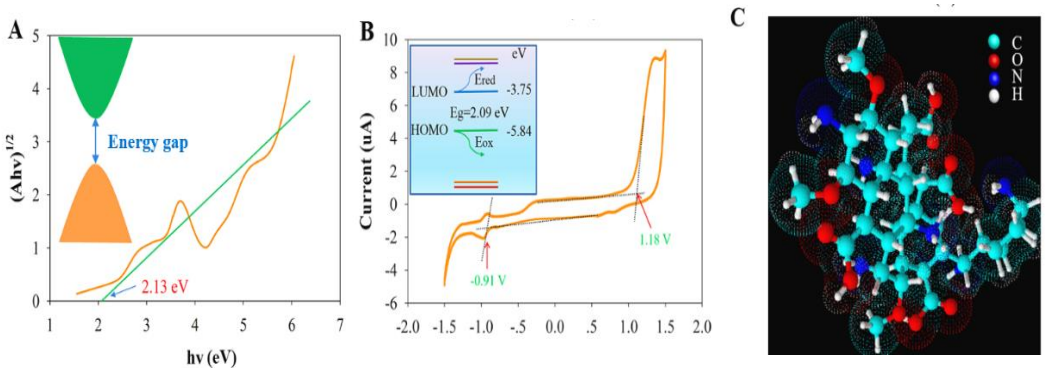

Figure 2.5. Energy Gap Analysis. (A) UV-Vis absorption spectrum of the CNDs used to estimate the optical band gap (E_0). (B) A cyclic voltammogram of the CNDs is shown, and the inset illustrates its relation to the energy levels. (C) A proposed molecule-like structure (with a formula $C_{36}H_{58}N_6O_{11}$) of individual CNDs based on the characterization results.

Conclusion

A new fluorescence spectroelectrochemistry approach was developed to investigate the real-time electrochemical-fluorescence properties of microwave synthesized CNDs, and a chemically reversible redox couple was used to reveal the influence of redox chemistry on the optoelectronic properties of the CNDs. The effect of different excitation wavelengths from a fluorescence spectrophotometer on the photocurrent generated by the CNDs modified gold slide electrodes upon different applied bias voltages was investigated systematically, suggesting wavelength dependence on photocurrent generation from the CNDs as electron donors to the gold electrode. The optical band gap of the CNDs obtained by the UV-Vis absorption spectrum is in reasonable agreement with the HOMO-LUMO energy gap found from electrochemical measurements. A theoretical Hückel model was adopted to obtain the molecular-like

CND structure and was fitted to match the experimental energy gap between HOMO and LUMO energy levels. From the both experimental and theoretical energy gap analysis and the observation of the fluorescence-based spectroelectrochemistry, the excitation dependent fluorescence of the CNDs may be attributed to a combination of the core C=C, surface functionalities (C=O, C-O, and COOH), and/or surface electronic state transitions. This study provides a new perspective on the optoelectronic properties of the CNDs, which should motivate and facilitate their broad applications in biomedicine (e.g. bioimaging, antioxidation) and photoelectric device

References

1. L. Wang, S.-J. Zhu, H.-Y. Wang, S.-N. Qu, Y.-L. Zhang, J.-H. Zhang, Q.-D. Chen, H.-L. Xu, W. Han, B. Yang and H.-B. Sun, ACS Nano, 2014, 8, 2541–2547.

2. K. Hola, A. B. Bourlinos, O. Kozak, K. Berka, K. M. Siskova, M. Havrdova, J. Tucek, K. Safarova, M. Otyepka, E. P. Giannelis and R. Zboril, Carbon, 2014, 70, 279–286.

3. Z. Luo, P. M. Vora, E. J. Mele, A. T. C. Johnson and J. M. Kikkawa, Appl. Phys. Lett., 2009, 94, 111909.

4. S. N. Baker and G. A. Baker, Angew. Chem., Int. Ed., 2010, 49, 6726–6744

5. S. K. Cushing, M. Li, F. Huang and N. Wu, ACS Nano, 2014, 8, 1002–1013

6. S. Zhu, J. Shao, Y. Song, X. Zhao, J. Du, L. Wang, H. Wang, K. Zhang, J. Zhang and B. Yang, Nanoscale, 2015, 7, 7927–7933.

7. G. Eda, Y.-Y.Lin, C.Mattevi,H.Yamaguchi,H.-A.Chen, I.S.Chen, C.-W. Chen and M. Chhowalla, Adv. Mater., 2010, 22, 505–509.

8. K. Krishnamoorthy, M. Veerapandian, R. Mohan and S.-J. Kim, Appl. Phys. A: Mater. Sci. Process., 2012, 106, 501–506.

9. H. Li, X. He, Z. Kang, H. Huang, Y. Liu, J. Liu, S. Lian, C. H. A. Tsang, X. Yang and S.-T. Lee, Angew. Chem., Int. Ed., 2010, 49, 4430–4434.

10. Y.-P. Sun, B. Zhou, Y. Lin, W. Wang, K. A. S. Fernando, P. Pathak, M. J. Meziani, B. A. Harruff, X. Wang, H. Wang, P. G. Luo, H. Yang, M. E. Kose, B. Chen, L. M. Veca and S.-Y. Xie, J. Am. Chem. Soc., 2006, 128, 7756–7757.

11. L. Cao, M. J. Meziani, S. Sahu and Y.-P. Sun, Acc. Chem. Res., 2013, 46, 171–180.

12. R. Liu, D. Wu, S. Liu, K. Koynov, W. Knoll and Q. Li, Angew. Chem., Int. Ed., 2009, 48, 4598–4601.

13. C. Lei, D. Hu and E. J. Ackerman, Chem. Commun., 2008, 5490–5492.

14. Y.-L. Chang, R. E. Palacios, F.-R. F. Fan, A. J. Bard and P. F. Barbara, J. Am. Chem. Soc., 2008, 130, 8906–8907.

15. S. Zaleski, M. F. Cardinal, J. M. Klingsporn and R. P. Van Duyne, J. Phys. Chem. C, 2015, 119, 28226–28234.

16. Z. Zeng, Y. Liu and J. Wei, TrAC, Trends Anal. Chem., 2016, 75, 162–173.

17. Y. Gründer, J. F. W. Mosselmans, S. L. M. Schroeder and R. A. W. Dryfe, The Journal of Physical Chemistry C, 2013, 117, 5765-5773.

18. B. Gadgil, P. Damlin, E. Dmitrieva, T. Aaritalo and C. Kvarnstrom, RSC Adv., 2015, 5, 42242–42249.

19. S. Qu, X. Wang, Q. Lu, X. Liu and L. Wang, Angew. Chem., Int. Ed., 2012, 51, 12215–12218.

20. M. Sanders, Y. Lin, J. Wei, T. Bono and R. G. Lindquist, Biosens. Bioelectron., 2014, 61, 95–101.

21. Z. Zeng, X. Shi, T. Mabe, S. Christie, G. Gilmore, A. W. Smith and J. Wei, Anal. Chem., 2017, 89, 5221–5229.

22. D. Yu, Y. Yang, M. Durstock, J.-B. Baek and L. Dai, ACS Nano, 2010, 4, 5633–5640.

23. C. M. Cardona, W. Li, A. E. Kaifer, D. Stockdale and G. C. Bazan, Adv. Mater., 2011, 23, 2367–2371.

24. Y. Liu, S. Jiang, K. Glusac, D. H. Powell, D. F. Anderson and K. S. Schanze, J. Am. Chem. Soc., 2002, 124, 12412–12413

25. H. Hou, C. E. Banks, M. Jing, Y. Zhang and X. Ji, Adv. Mater., 2015, 27, 7861–7866.

26. C. S. Lim, K. Hola, A. Ambrosi, R. Zboril and M. Pumera, Electrochemistry Communications, 2015, 52, 75-79.

27. S. Muthulingam, K. B. Bae, R. Khan, I.-H. Lee and P. Uthirakumar, RSC Adv., 2015, 5, 46247–46251.

28. Q. Cui, J. Xu, X. Wang, L. Li, M. Antonietti and M. Shalom, Angew. Chem., Int. Ed., 2016, 55, 3672–3676.

29. T.V. Cuong,V. H.Pham, Q.T. Tran,S.H.Hahn, J.S.Chung, E. W. Shin and E. J. Kim, Mater. Lett., 2010, 64, 399–401.

30. Z. Luo, Y. Lu, L. A. Somers and A. T. C. Johnson, J. Am. Chem. Soc., 2009, 131, 898–899.

31. S. K. Bhunia, A. Saha, A. R. Maity, S. C. Ray and N. R. Jana, Sci. Rep., 2013, 3, 1473.

32. X. Li, S. Zhang, S. A. Kulinich, Y. Liu and H. Zeng, Sci. Rep., 2014, 4, 4976.

33. M. Fu, F. Ehrat, Y. Wang, K. Z. Milowska, C. Reckmeier, A. L. Rogach, J. K. Stolarczyk, A. S. Urban and J. Feldmann, Nano Lett., 2015, 15, 6030–6035.

34. Z.-C. Yang, M. Wang, A. M. Yong, S. Y. Wong, X.-H. Zhang, H. Tan, A. Y. Chang, X. Li and J. Wang, Chem. Commun., 2011, 47, 11615–11617.

35. C. A. Schroll, S. Chatterjee, W. R. Heineman and S. A. Bryan, Anal. Chem., 2011, 83, 4214–4219.

36. D. Iban ˜ez, J. Garoz-Ruiz, A. Heras and A. Colina, Anal. Chem., 2016, 88, 8210–8217.

37. M. Amjadi, J. L. Manzoori, T. Hallaj and M. H. Sorouraddin, Spectrochim. Acta, Part A, 2014, 122, 715–720.

38. V. Strauss, J. T. Margraf, C. Dolle, B. Butz, T. J. Nacken, J. Walter, W. Bauer, W. Peukert, E. Spiecker, T. Clark and D. M. Guldi, J. Am. Chem. Soc., 2014, 136, 17308–17316.

39. A. Kongkanand, K. Tvrdy, K. Takechi, M. Kuno and P. V. Kamat, J. Am. Chem. Soc., 2008, 130, 4007–4015.

40. R. Miao, Z. Luo, W. Zhong, S.-Y. Chen, T. Jiang, B. Dutta, Y. Nasr, Y. Zhang and S. L. Suib, Appl. Catal., B, 2016, 189, 26–38.

41. W. Wu, L. Zhan, W. Fan, J. Song, X. Li, Z. Li, R. Wang, J. Zhang, J. Zheng, M. Wu and H. Zeng, Angew. Chem., 2015, 127, 6640–6644.

42. Y. Hao, Z. Gan, X. Zhu, T. Li, X. Wu and P. K. Chu, J. Phys. Chem. C, 2015, 119, 2956–2962.

43. A. Mohite, J.-T. Lin, G. Sumanasekera and B. W. Alphenaar, Nano Lett., 2006, 6, 1369–1373.

44. G. Likhtenshtein, Electron Spin Interactions in Chemistry and Biology, Springer International Publishing, 1st edn, 2016.

45. M. Harb, Phys. Chem. Chem. Phys., 2015, 17, 25244–25249.

46. D. Moses, J. Wang, A. J. Heeger, N. Kirova and S. Brazovski, Proc. Natl. Acad. Sci. U. S. A., 2001, 98, 13496–13500.

47. Y. Zou, A. Najari, P. Berrouard, S. Beaupré, B. Réda Aïch, Y. Tao and M. Leclerc, Journal of the American Chemical Society, 2010, **132**, 5330-5331.

48. J. Shang, L. Ma, J. Li, W. Ai, T. Yu and G. G. Gurzadyan, Sci. Rep., 2012, 2, 792.

49. C. Galande, A. D. Mohite, A. V. Naumov, W. Gao, L. Ci, A. Ajayan, H. Gao, A. Srivastava, R. B. Weisman and P. M. Ajayan, Scientific Reports, 2011, **1**, 85.

50. R. Miao, Z. Luo, W. Zhong, S.-Y. Chen, T. Jiang, B. Dutta, Y. Nasr, Y. Zhang and S. L. Suib, Appl. Catal., B, 2016, 189, 26–38.

51. W. Wu, L. Zhan, W. Fan, J. Song, X. Li, Z. Li, R. Wang, J. Zhang, J. Zheng, M. Wu and H. Zeng, Angew. Chem., 2015, 127, 6640–6644.

CHAPTER III

ELECTROCHEMICAL STUDY OF DPPH RADICAL SCAVENGING FOR EVALUATING THE ANTIOXIDANT CAPACITY OF CARBON NANODOTS

This chapter has been published as: Zhang, W., Zeng, Z., & Wei, J. (2017). Electrochemical study of DPPH radical scavenging for evaluating the antioxidant capacity of carbon nanodots. The Journal of Physical Chemistry C, 121(34), 18635-18642.

Introduction

Carbon nanodots (CNDs) have been prepared in several different ways, including chemical ablation, electrochemical carbonization, laser ablation, hydrothermal/solvothermal treatment, and microwave irradiation, and they have found applications in biomedicine, chemical sensing, and photoelectric devices.[1-4] Their physicochemical properties of good solubility, low toxicity, and biocompatibility and their optoelectronic properties of strong fluorescence, phosphorescence, chemiluminescence, and photoinduced electron transfer make them particularly desirable.[5–8] Reportedly, CNDs could act as antioxidants and prooxidants due to their roles as electron donors or electron acceptors.[9] Xu et al. studied the antioxidative ability of CNDs at the cellular level, which showed good potential for applying CNDs to protect cells against oxidative stress.[10] Das et al. used microwave-synthesized CNDs to scavenge reactive oxygen species like hydroxyl radicals and superoxides in a cellular

microenvironment.[11] The nitrogen-centered 2,2-diphenyl-1-picrylhydrazyl radical (DPPH•)-based assay has been one of the most commonly employed species to evaluate the antioxidant activity[12] because it can change its color from deep violet to light yellow in a dark environment when in contact with antioxidants due to the DPPH• being converted into a stable DPPH−H complex, which could be calculated by comparing the absorbance at 517 nm against the blank by ultraviolet−visible (UV−vis) specroscopy.[13] Although CNDs have experienced some research on their antioxidation properties via the DPPH•-based assay, UV−vis spectroscopy has been the only tool to test the absorbance change under different incubation concentrations of CNDs. A poor understanding about the relationship between the reserved DPPH• concentration and CNDs incubation concentration and underlying antioxidation reactions limits their potential applications in biology fields, especially in biomedicine.

Electrochemistry could be another powerful tool to determine the concentration relationship via the cyclic voltammetry method because redox peak currents and peak potentials are related to the parameters of bulk diffusion species, such as the bulk concentration, diffusion coefficient, number of electrons involved, and heterogeneous electron transfer rate constant. [14–16] This work reports an electrochemical study to investigate the change of redox peaks of the DPPH •−gold electrode system incubated with different concentrations of CNDs synthesized from citric acid and urea (named U-dots). Here, water-soluble U-dots were synthesized by a simple one-step microwave route and were characterized by transmission electron microscopy (TEM), atomic force microscope (AFM), X-ray photoelectron spectroscopy (XPS), Fourier transform infrared

spectroscopy (FTIR), Raman spectroscopy, X-ray powder diffraction (XRD), UV−vis spectroscopy, fluorescence spectroscopy, and quantum yield measurements. An analytical model was used to examine the reserved DPPH • concentration and standard heterogeneous electron-transfer rate constant changes in the DPPH •−gold electrode system incubated by different concentrations of U-dots. The results were compared with antioxidation activity changes measured by absorbance at 517 nm via UV−vis spectroscopy, which further activates the mechanism study of DPPH• scavenging by the U-dots.

Methods and Materials

Synthesis of U-dots: A microwave assisted synthesis of CNDs was performed using citric acid and urea as precursors.[17] Briefly, 1.0 g urea (Aldrich) and 1.0 g of citric acid (ACROS Organics) were simultaneously added to 1.0 mL deionized water to form a homogeneous solution and then heated in a microwave synthesizer (CEM Corp 908005 Microwave Reactor Discovery System) at a power of 300 W for 18 minutes. After cooling, the aqueous reaction mixture was purified using a centrifuge (Solvall Legend XFR Floor Model Centrifuge) at 3500 r/min for 20 min to remove large and aggregated particles. The dark-brown solution was further purified using a dialysis membrane (Scientific Fisher) with a molecular weight cut off of 1000 Da for 24 hours. To obtain the solid sample, the resultant solution was finally dried with a freeze dryer (Labconco Free Zone 6 Freeze Dryer) for 24 hours. We named this type of CNDs as U-dots.

U-dots characterization: Atomic force microscope (AFM, Agilent Technologies 5600 LS Series) was used to study the size of U-dots. XRD (Agilent Technologies Oxford Gemini), FTIR (Varian 670), XPS (Thermo Fisher ESCALAB 250 Xi), and Raman spectroscopy (Horiba XploRA One Raman Confocal Microscope System), were employed to analyze the elemental composition and chemical structure of the U-dots. UV-Vis spectroscopy (Varian Cary 6000i) and fluorescence spectroscopy (Varian Cary Eclipse) were used to investigate the absorbance and fluorescence properties of U-dots, respectively.

UV-Vis study of antioxidation activity: The antioxidation activity of U-dots to DPPH• (Alfa Aesar) was evaluated by monitoring the absorbance change at 517 nm via the UV-Vis spectroscopy.[18] For each measurement, the DPPH• was prepared with a final concentration of 0.02 mg/mL (52 nmol/mL) in absolute methanol incubated by different concentrations of U-dots in the dark environment for 1.5 h.

Electrochemistry study: The electrochemical measurements were performed using a three-electrode electrochemical cell with a gold working electrode (Fisher Scientific), a Ag/AgCl reference electrode (Fisher Scientific), and a platinum counter electrode (Fisher Scientific) in a 5.0 mL methanolic phosphate buffer (a 1:1 mixture of absolute methanol (Fisher Scientific) and phosphate buffer (Life Tech) with pH7.2 (Fisher Scientific pH 2100) solution containing 0.02 mg/mL (52 nmol/mL) DPPH• incubated by different concentrations of U-dots for 1.5 h under dark environment. Cyclic voltammetry of the samples was run at different scan rates under room temperature.

Results and Discussion

U-dots synthesis and characterization: An easy, economic, one-step microwave route was used to synthesize U-dots from citric acid and urea.[17] TEM (Figure 3.1A) and AFM (Figure 3.1B) studies indicate that the U-dots are well dispersed and have an average size of 2.4±0.3 nm. The main diffraction peak in the XRD spectrum (Figure 3.1C) appears at 22.9° with a full width at half maximum (FWHM) of about 3.7°, corresponding to an interlayer distance of 0.39 nm between the planar carbon based sheets for disordered graphite structure region,[19] which is further supported by the Raman spectra of the U-dots (Figure 3.1C inserted). The D bands at 1338 cm^{-1} (sp^3-hybridized) and G bands at 1568 cm^{-1} (sp^2-hybridized) present an intensity ratio I_D/I_G of about 1.04.[20-21] FTIR spectra of the U-dots (Figure 3.1D) display broad bands at 3100-3400 cm^{-1} which are assigned to ν(O-H) and ν(N-H). The IR transitions at 754, 1183, 1397 and 1576 cm^{-1} are assigned to ν(C-C), ν(C-O), ν(C=C) and ν(C=O), respectively,[22] which are also supported by XPS data (Figure 3.1E) of the U-dots. The XPS data demonstrate four components: C=C (39.9%, 284.2 eV), C-C (8.7%, 284.7 eV), C=O (42.1%, 287.6 eV), and C-O (7.9%, 286.2 eV). The presence of functionalities (-COOH and $-NH_3$) (Figure 3.1E) helps explain the hydrophilicity and stability of the CNDs in aqueous media.[23-25] From the characterization results, the structure of the as-prepared U-dots are spherical with an average size of 2.4±0.3 nm and composed of a disorder graphite structure with surrounding amorphous carbon frames and different functional groups on the surfaces.[26]

Figure 3.2A shows there is no obvious absorption feature found above 600 nm. The main peak at 337 nm comes from the n-π^* transition of the C=O bond. Figure 3.2B shows the fluorescence emission spectra of U-dots in deionized water at seven different excitation wavelengths (λ_{ex}=330, 360, 390, 420, 450, 480 and 510 nm). The maximum emission intensity occurs with 360 nm excitation and has a peak emission at 447 nm. The apparent red-shift in the photoluminescence spectra with changing excitation wavelength indicates U-dots can act as blue/green fluorophores in imaging applications, which is in agreement with other reports.[27-29] Furthermore, the quantum yield of U-dots was investigated according to established methods.[30] Quinine sulfate (quantum yield of 0.54 at 360 nm) dissolved in 0.1 M H_2SO_4 (refractive index=1.33) was chosen as the reference. The absorbance and photoluminescence intensity measurements via the UV-Vis spectrometer and photoluminescence spectrometer give a quantum yield of about 0.091 for the as-prepared U-dots.

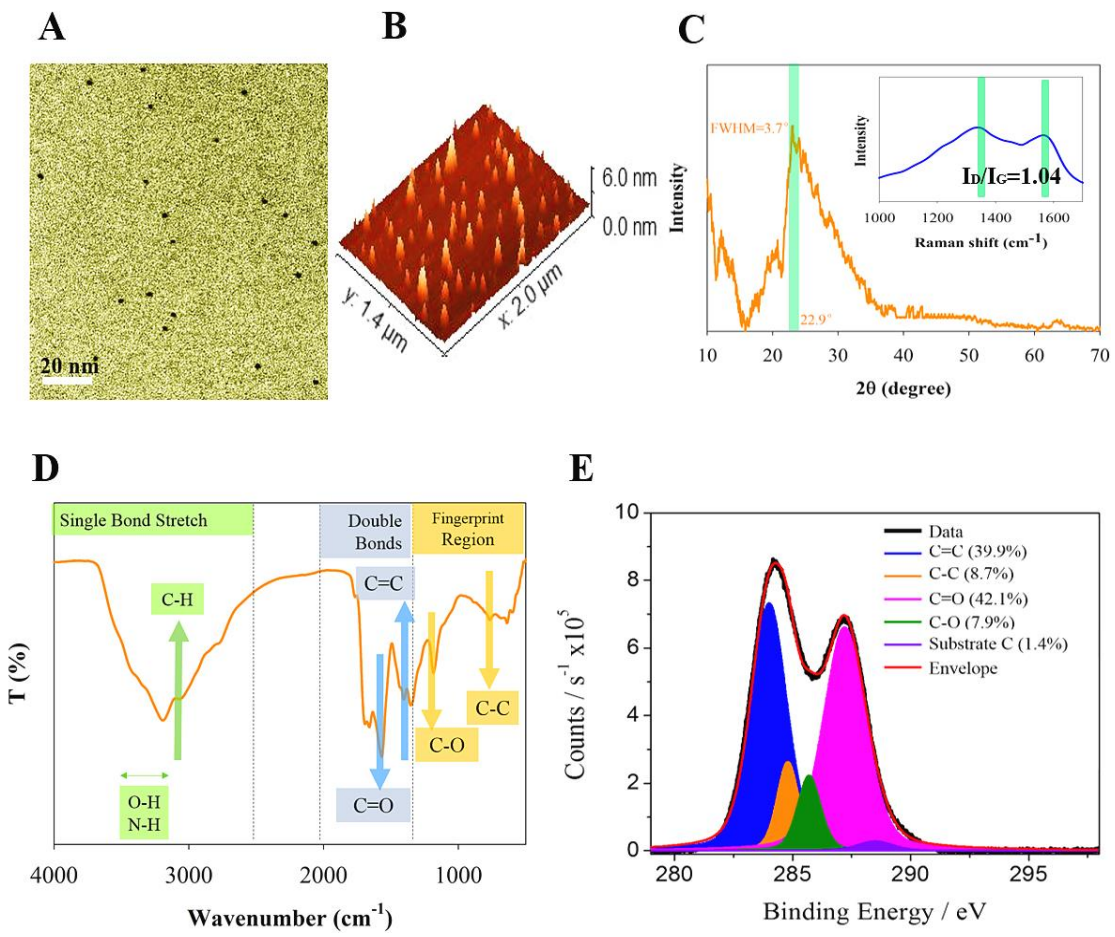

Figure 3.1. U-Dots Characterization. The U-dots are characterized using different techniques: transmission electron microscopy (A), atomic force microscope (B), X-ray diffraction data with Raman spectrum inserted (C), Fourier transform infrared spectrum (D), and X-ray photoelectron spectrum (C signal) (E).

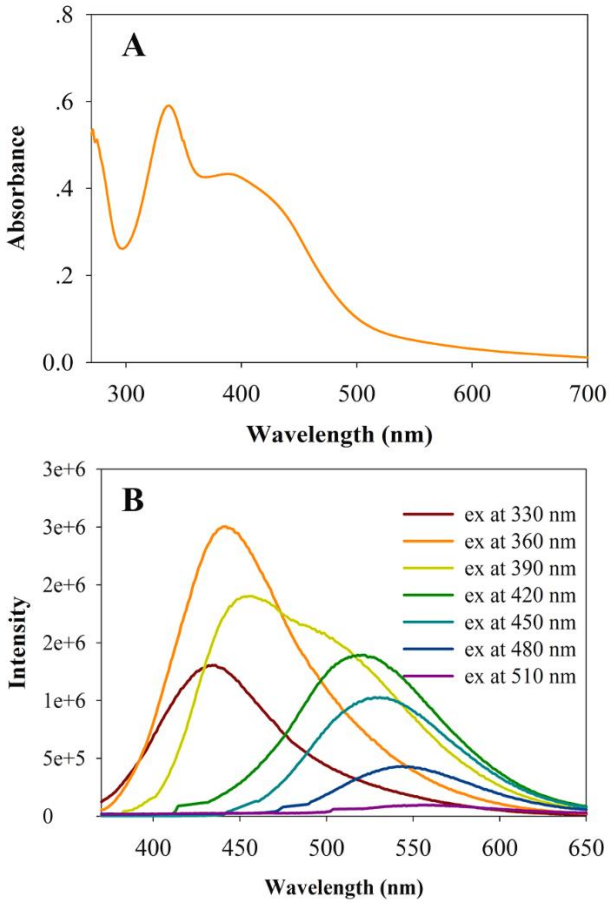

Figure 3.2. UV-Vis and Fluorescence. (A) UV-Vis absorption spectrum of U-dots. (B) Fluorescence emission spectra of U-dots in deionized water.

UV-Vis study of antioxidation activity of U-dots: The antioxidation activity was evaluated by using the DPPH• based array via the UV-Vis spectroscopy. DPPH• is known as a stable free radical resulted from delocalization of the spare electron, which shows a deep violet color in methanol solution.[31] However, upon addition of different concentrations of U-dots, the absorbance of DPPH• methanol solutions at 517 nm decreases as shown in Figure 3.3A and its color changes from deep violet to pale yellow. According to the following equation:

$$antioxidation \cdot activity = \frac{A_0 - A_c}{A_0} \times 100\% \quad (1)$$

where A_0 and Ac are the absorbance of DPPH• at 517 nm in the absence and presence of U-dots respectively, the antioxidation activity is obtained to be about 23.3, 52.4, 73.0, 82.4, and 87.3% at U-dots concentrations of 0.02, 0.04, 0.05, 0.07, and 0.09 mg/mL, respectively. A minimum of three trials of each concentration were measured, and the DPPH •−U-dots incubation reached its steady state after 1.5 h and was highly reproducible. The error bars are too minimal to see in Figure 3.3B. A subsequent increase in the antioxidant activity presents a dose-dependent manner, and the antioxidant activity is observed to have a plateau region at higher concentrations of U-dots (Figure 3.3B).

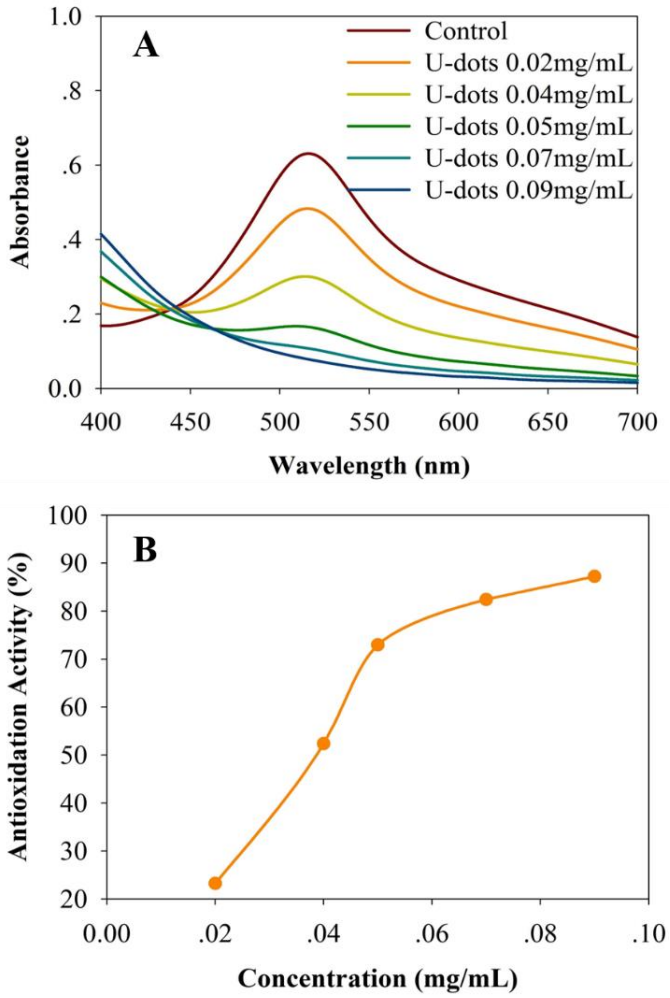

Figure 3.3. UV-Vis DPPH• Test. (A) Absorption spectra of 0.02 mg/mL DPPH• methanol solutions with increasing U-dots concentration from 0 to 0.09 mg/mL measured after incubation for 1.5 h under dark environment. (B) The calculated antioxidation activity versus U-dots concentration (very reproducible and error bar is too minimal to see).

Electrochemical Study of DPPH • Scavenging Activity of U-dots: The electrode reactions of DPPH• are of interest due to free radicals frequently being intermediates and products of electrode reactions, following reversible, one-electron reactions.[32] In general, the peaks of both redox couples (oxidation: α/α′ couple; reduction: β/β′ couple) could be

observed in most of the solutions during the cyclic voltammetry. However, in a 5.0 mL methanolic phosphate buffer solution using a gold working electrode, the β/β′ couple was found to be irreversible, suggesting that the reduction product is particularly unstable in this solution.[33] Hence, for the purpose of the electrochemical electron-transfer study in this work, we focus on the α/α′ redox reaction. The cyclic voltammograms of DPPH• incubated by different concentrations of U-dots at different scan rates show a pair of redox peaks (Figure 3.4). The cathodic peak resulted from the electrochemical reduction of DPPH• and the decrease in the intensity of the anodic and cathodic peaks present (Figures 4.4 and 4.5A) with increasing concentration of U-dots. Because no measurable redox peaks are shown for 0.05 mg/mL U-dots in a 5.0 mL methanolic phosphate buffer or the stable cyclic voltammograms of 0.01 mg/mL DPPH• in a 5.0 mL methanolic phosphate buffer (but lower peak currents compared to 0.02 mg/mL DPPH•) without U-dots incubation, the decrease in the intensity of the anodic and cathodic peaks for DPPH• incubated by different concentrations of U-dots is due to the decrease in the concentration of DPPH•. A similar method and results have been reposted for the scavenging of DPPH • by using Trolox in ethanolic phosphate buffer and flavonoids in an aprotic medium.[34,35] The fwhm of the reduction peak gives a value of about 116 mV, corresponding to a one-electron-transfer redox reaction (Figure 3.5A). In addition, the peak current, ip (A), is measured as a function of the square root of the voltage scan rate at different concentrations of U-dots and is found to exhibit a liner dependence (Figure 3.5B). The dependence of the peak current position on the square root of the voltage scan

rate for the DPPH • without U-dots incubation can be first used to characterize the diffusion coefficient (D0, cm ^{2}/s) of DPPH• through the Randles −Sevcik equation[36,37]

$$i_p = \left(2.69\times10^5\right) n^{3/2} A C D_0^{1/2} \nu^{1/2} \quad (2)$$

where n is the number of electrons exchanged, A is the active surface area of the gold electrode (0.043 cm ^{2}), C is the concentration of the DPPH • (mol/mL), and ν is the voltage scan rate (V/s). The diffusion coefficient of DPPH• is found to be about 1.24 × 10^{-5} cm^2/s. By using eq 2, this value can then be coupled with plots of the dependence at different concentrations of U-dots (Figure 3.5B) to extract the concentration of the DPPH • values for different systems (Figure 3.5C). The reserved DPPH• concentration is obtained to be about 32.3, 26.1, 24.5, 20.4, and 18.5 nmol/mL at U-dots concentrations of 0.02, 0.04, 0.05, 0.07, and 0.09 mg/mL (Table IV-1) with radical scavenging activity of about 38.1, 49.9, 256 53.1, 60.8, and 64.6%, respectively (Figure 3.5C inset) according to eq 3.

$$scavenging \cdot activity = \frac{C_0 - C_c}{C_0} \times 100\% \quad (3)$$

where C_0 and C_c are the concentration of DPPH• in the absence and presence of U-dots, respectively. The data are then best fitted by the following equation:

$$C_{DPPH\bullet} = \frac{0.0277}{1+\left(\frac{C_{U-dots}}{-0.1019}\right)^{0.5728}} - 0.0071 \quad (4)$$

where $C_{DPPH•}$ (mg/mL) and $C_{U\text{-}dots}$ (mg/mL) are the concentrations of reserved DPPH • and U-dots addition, respectively, which have the same trend as the antioxidation activity shown in Figure 3.3. Furthermore, the ratio of the anodic peak current to the cathodic one closes to 1 for each scan rate, suggesting that a heterogeneous electron transfer is present. Also, the slope of the linearization decreases with the increase of U-dots concentrations, indicating that U-dots weaken the electron transfer in the DPPH •−gold electrode system.

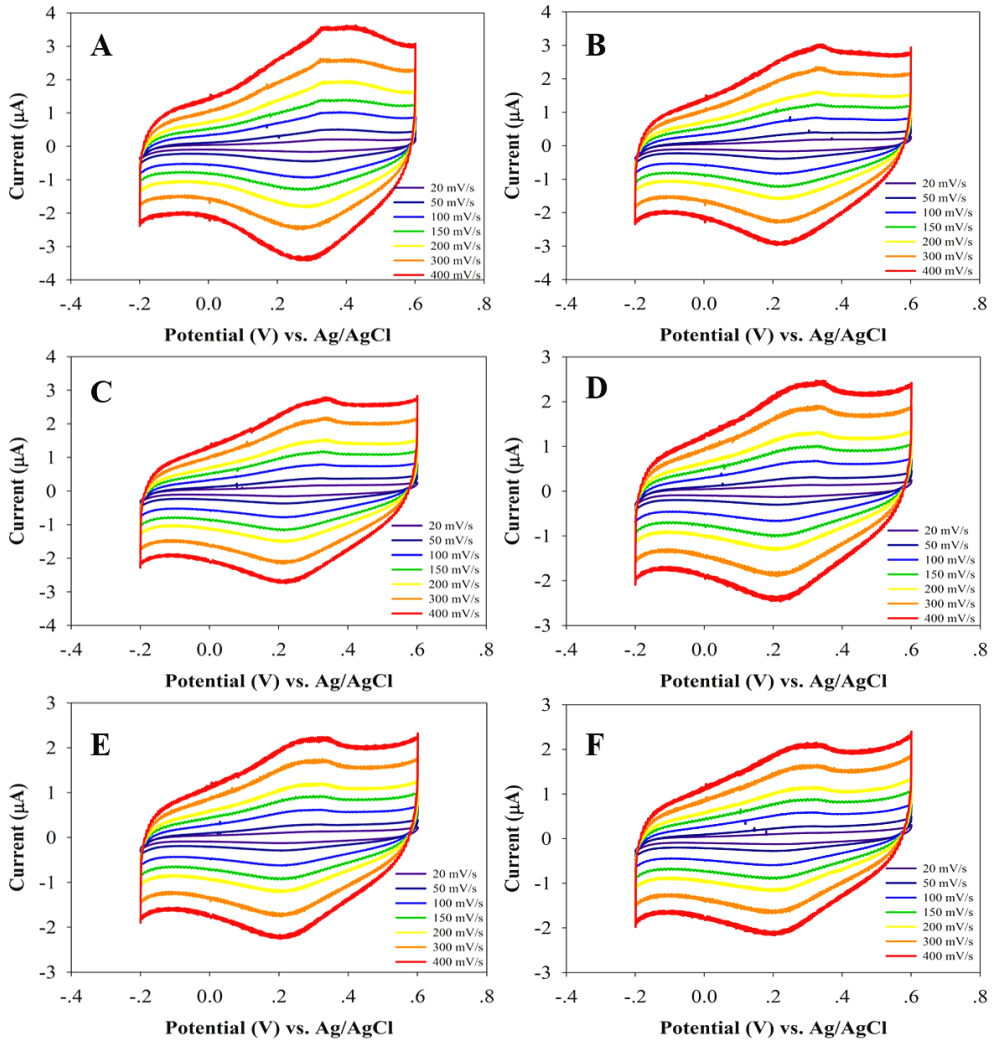

Figure 3.4. Cyclic Voltammograms Results. Cyclic voltammograms for the DPPH•-gold electrode system incubated by 0.00 mg/mL (A), 0.02 mg/mL (B), 0.04 mg/mL (C), 0.05 mg/mL (D), 0.07 mg/mL (E), and 0.09 mg/mL (F) of U-dots for 1.5 under dark environment at 20, 50, 100, 150, 200, 300 and 400 mV/s scan rates.

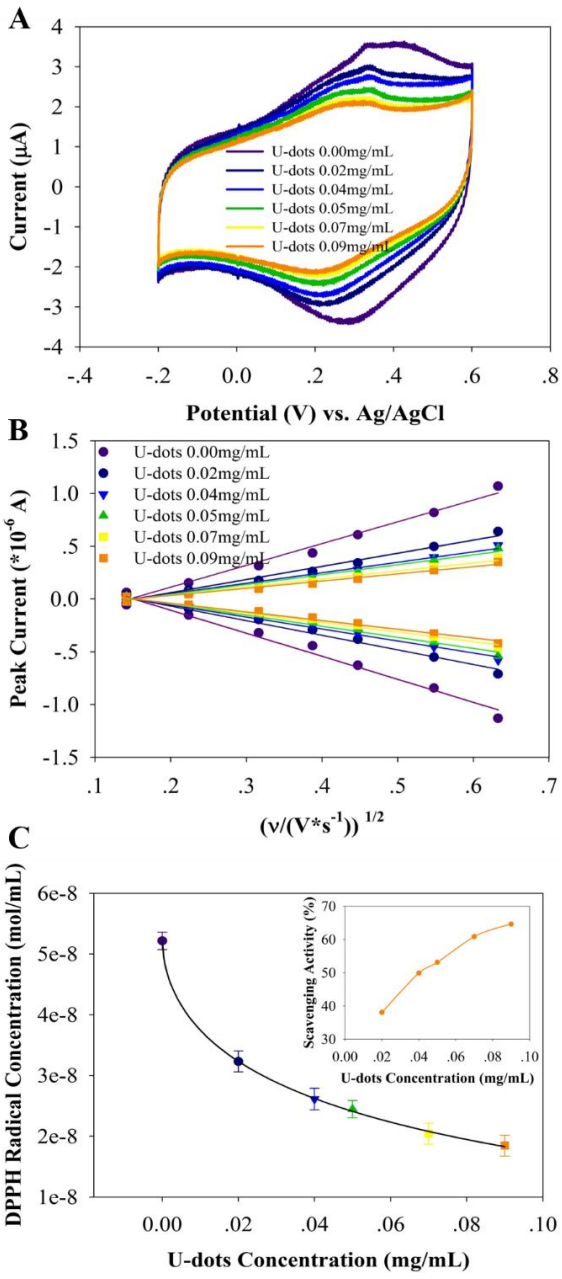

Figure 3.5. Reserved DPPH• Concentration. (A) Cyclic voltammograms for the DPPH•-gold electrode system incubated by different concentrations of U-dots at the scan rate of 400 mV/s. (B) The linear dependence of the peak current on the voltage scan rate incubated by different concentrations of U-dots. (C) The reserved DPPH• concentration estimation with the best fit after incubation with different concentrations of U-dots for 1.5 h under dark environment. The insert is calculated scavenging activity versus U-dots concentration.

Table 3.1 Results Obtained from Electrochemical Measurements

U-dots concentration (mg/mL)	**Antioxidation activity (%)**	**DPPH• Concentration (nmol/mL)**	**k^0 (cm/s)**
0.00	0	52.2±1.4	0.0093±0.0015
0.02	23.30±0.08	32.3±1.7	0.0061±0.0009
0.04	52.38±0.01	26.1±1.8	0.0058±0.0007
0.05	72.98±0.02	24.5±1.4	0.0055±0.0005
0.07	82.42±0.05	20.4±1.7	0.0049±0.0003
0.09	87.26±0.02	18.5±1.7	0.0046±0.0002

The dependence of the redox peak 's position on the voltage scan rate can be used to characterize the electron-transfer rate constant. The electron-transfer reaction can be written as eq 5 with the oxidation electron-transfer rate of k_{ox} from DPPH• to DPPH + and the reversed reduction electron-transfer rate of k_{red} from DPPH + to DPPH•

$$Red\text{-}e \underset{k_{red}}{\overset{\overrightarrow{k_{ox}}}{\rightleftharpoons}} Ox \tag{5}$$

where Red and Ox represent DPPH • and DPPH+, respectively. The Gibbs free energy of this reaction can be easily changed by the applied external potential; therefore, the electron-transfer rate k_{ox} or k_{red} is also subjected to the potential. In the case of the equilibrium state, $k_{ox} = k_{red} = k_0$ is the standard heterogeneous rate constant given by [38.]

$$k^0 = 2.18\left(\frac{\alpha D_0 nF\nu}{RT}\right)^{1/2} \exp\left[\frac{-\alpha^2 nF\left(E_{pa} - E_{pc}\right)}{RT}\right] \tag{6}$$

where α is the transfer coefficient, D_0 is the diffusion coefficient (cm^2/s), F is the Faraday's constant, R is the gas constant, T is temperature in Kelvin, E_{pa} *and* E_{pc} are the anodic and cathodic peak potentials, respectively. These calculations can then be compared to plots of the experimental Faradaic peak potential shift from apparent formal potential versus voltage scan rates (Figure 3.6A) to extract the k^0 values for different systems (Figure 3.6B). In the absence of U-dots, the standard heterogeneous electron-transfer rate constant (k^0) for DPPH•-gold electrode system is calculated to be ~0.0093 cm/s. After DPPH• incubation by U-dots for 1.5 h under dark environment, the k^0 is obtained to be about 0.0061, 0.0058, 0.0055, 0.0049, 0.0046 cm/s at U-dots concentration of 0.02, 0.04, 0.05, 0.07, 0.09 mg/mL which decreased by about 34.9%, 37.5%, 40.6%, 47.0%, 50.5%, respectively (Figure 3.6B inserted), compared to that without U-dots incubation. The standard heterogeneous electron-transfer rate constant decrease could be resulted from two phenomena: the first is a decrease in the mass transfer due to low concentration gradient according to the Fick's law resulted from DPPH• converted into a stable DPPH-H complex as mentioned above (Figure 3.5 and ~0.0063 cm/s for 0.01 mg/mL of DPPH•),[39] and the second is an increase of the diffusive mass and friction in the solution due to the DPPH•-U-dots complex formation along DPPH• diffusion direction), suggesting lower reserved concentration of DPPH• due to the U-dots incubation, which indirectly proves the DPPH• scavenging activity of U-dots.

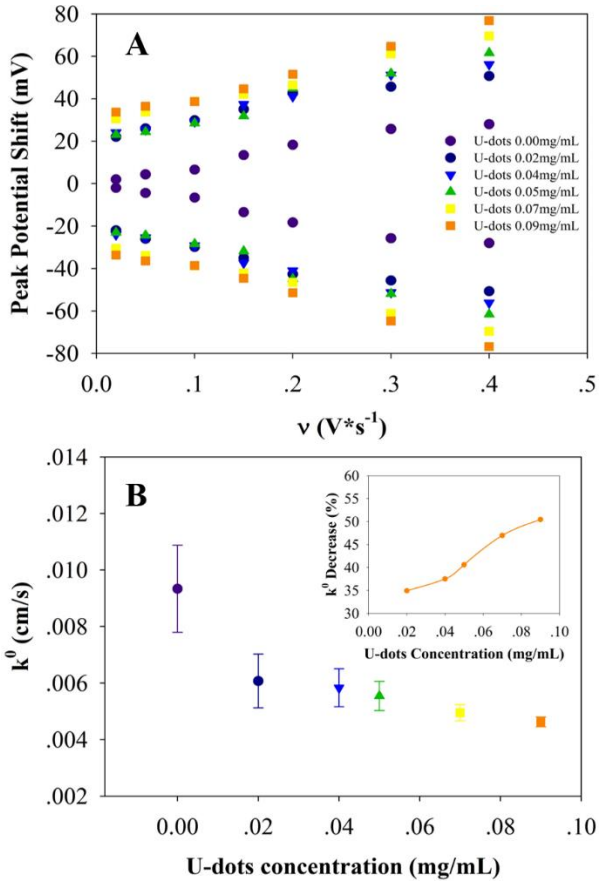

Figure 3.6. Heterogenous Electron Transfer Rate Constant. (A) The dependence of the peak potential shift on the scan rate is shown for the DPPH•-gold electrode system incubated by different concentrations of U-dots. (B) Plot of k^0 versus different concentrations of U-dots. The insert is k^0 decrease versus U-dots concentration.

The entire picture described above led us to understand how different concentrations of U-dots incubation affect the reserved concentration of DPPH• and electron transfer of the DPPH•-gold electrode system. As shown in Figure 7, in the absence of U-dots incubation, this general electrochemical process shows that the observed redox peak currents (α/α′ couple as highlighted) are dependent upon mass transport of DPPH• with diffusion coefficient of about 1.24×10^{-5} cm^2/s, which occurs in series with standard heterogeneous electron-transfer rate constant of 0.0093±0.0015 cm/s.

However, in the presence of U-dots incubation, a proton is taken up from the U-dots and the DPPH• is changed into DPPH-H (a neutral species) via a HAT mechanism, since U-dots have surface active groups like carboxyl group (-COOH) acting as proton donors.[40] Note that the electron cloud density between the hydrogen and oxygen in the carboxyl group is small due to the carboxyl group has an electron-withdrawing “carbonyl”, and -COO- is highly stable after deprotonation of carboxyl group. So, together with the standard heterogeneous electron-transfer rate constant analysis, higher concentrations of U-dots incubation results in lower reserved concentrations of DPPH• to conduct redox reaction as equ. 4 showing the relationship between reserved DPPH• concentration and U-dots incubation concentration, which highly supports the antioxidation activity test by the UV-Vis spectroscopy.

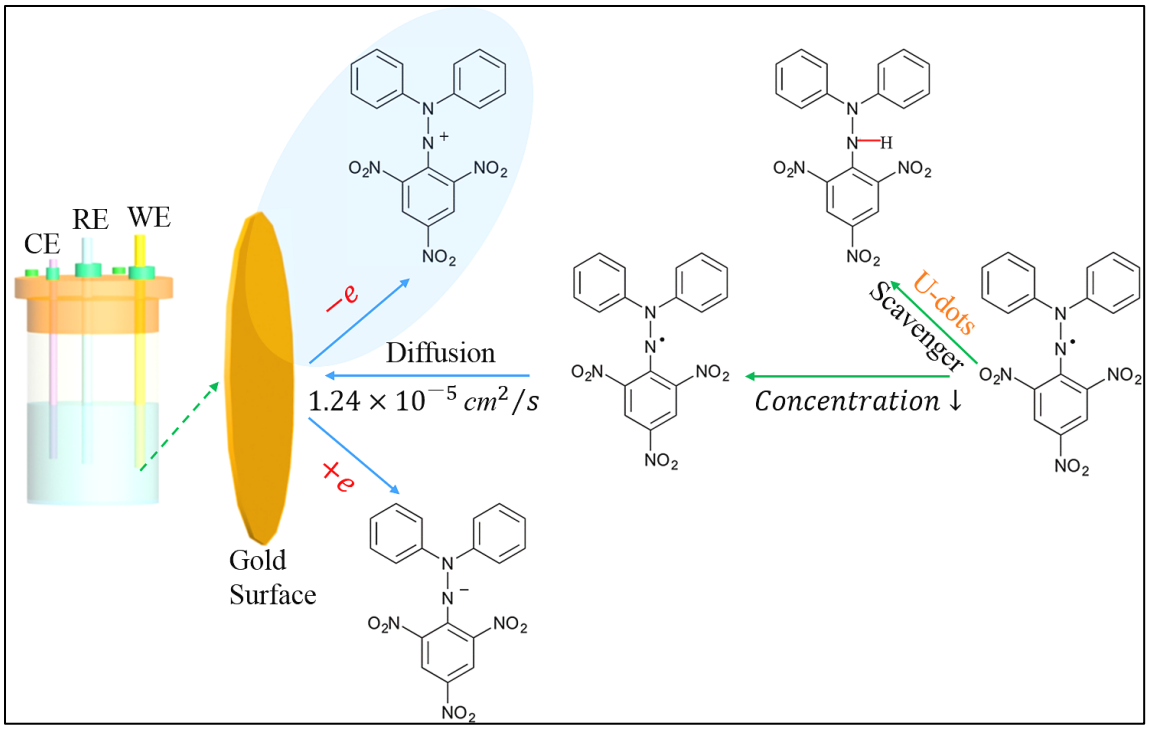

Figure 3.7. Mechanism for Electrochemical Study. Mechanism for electrochemical study of DPPH• scavenging by the U-dots incubation.

Conclusion

This work demonstrates a new strategy for exploring the antioxidation activity of U-dots by investigating reserved DPPH• concentration and standard heterogeneous electron-transfer rate constant changes in the DPPH•-gold electrode system with U-dots incubation. The relationship between reserved DPPH• concentration and CNDs incubation concentration supports the UV-Vis absorption dose-dependent results via a hydrogen atom transfer (HAT) mechanism, which should aid the development of this type of CNDs for practical use in biomedicine.

References

1. Zhu, S.; Meng, Q.; Wang, L.; Zhang, J.; Song, Y.; Jin, H.; Zhang, K.; Sun, H.; Wang, H.; Yang, B. Angew. Chem., Int. Ed. 2013, 52, 3953−3957.
2. Lim, S. Y.; Shen, W.; Gao, Z. Chem. Soc. Rev. 2015, 44, 362−381.
3. Zheng, X. T.; Ananthanarayanan, A.; Luo, K. Q.; Chen, P. Small 2015, 11, 1620−1636.
4. Liu, D.; Qu, F.; Zhao, X.; You, J. J. Phys. Chem. C 2015, 119, 17979−17987.
5. Wang, Y.; Hu, A. J. Mater. Chem. C 2014, 2, 6921−6939.
6. Li, X.; Rui, M.; Song, J.; Shen, Z.; Zeng, H. Adv. Funct. Mater. 2015, 25, 4929−4947.
7. Xu, Q.; Wei, J.; Wang, J.; Liu, Y.; Li, N.; Chen, Y.; Gao, C.; Zhang, W.; Sreeprased, T. S. RSC Adv. 2016, 6, 28745−28750.
8. Kumar, V. B.; Borenstein, A.; Markovsky, B.; Aurbach, D.; Gedanken, A.; Talianker, M.; Porat, Z. J. Phys. Chem. C 2016, 120, 13406−13413.
9. Jiang, H.; Chen, F.; Lagally, M. G.; Denes, F. S. Langmuir 4112010 , 26, 1991−1995.
10. Xu, Z.-Q.; Lan, J.-Y.; Jin, J.-C.; Dong, P.; Jiang, F.-L.; Liu, Y. ACS Appl. Mater. Interfaces 2015, 7, 28346−28352.
11. Das, B.; Dadhich, P.; Pal, P.; Srivas, P. K.; Bankoti, K.; Dhara, S. J. Mater. Chem. B 2014, 2 , 6839−6847.
12. Sachdev, A.; Gopinath, P. Analyst 2015, 140, 4260 −4269.
13. Zhao, S.; Lan, M.; Zhu, X.; Xue, H.; Ng, T.-W.; Meng, X.; Lee, 425C.-S.; Wang, P.; Zhang, W. ACS Appl. Mater. Interfaces 2015, 7, 17054− 17060.
14. Foti, M. C.; Daquino, C.; Geraci, C. J. Org. Chem. 2004, 69, 2309−2314.
15. Jha, N. S.; Mishra, S.; Jha, S. K.; Surolia, A. Electrochim. Acta 4352015 , 151, 574−583.
16. Khoshtariya, D. E.; Dolidze, T. D.; Zusman, L. D.; Waldeck, D. H. J. Phys. Chem. A 2001, 105, 1818 −1829.

17. Qu, S.; Wang, X.; Lu, Q.; Liu, X.; Wang, L. Angew. Chem., Int. Ed. 2012, 51, 12215−12218.

18. Garcia, E. J.; Oldoni, T. L. C.; Alencar, S. M. d.; Reis, A.; 446Loguercio, A. D.; Grande, R. H. M. Braz.Dent. J. 2012, 23, 22 −27.

19. Cui, Q.; Xu, J.; Wang, X.; Li, L.; Antonietti, M.; Shalom, M. Angew. Chem., Int. Ed. 2016, 55, 3672 −3676.

20. Lim, C. S.; Hola, K.; Ambrosi, A.; Zboril, R.; Pumera, M. Electrochem. Commun. 2015, 52, 75 −79.

21. Muthulingam, S.; Bae, K. B.; Khan, R.; Lee, I.-H.; Uthirakumar, P. RSC Adv. 2015, 5, 47−46251.

22. Hou, H.; Banks, C. E.; Jing, M.; Zhang, Y.; Ji, X. Adv. Mater. 2015, 27, 7861−7866.

23. Zhang, M.; Bai, L.; Shang, W.; Xie, W.; Ma, H.; Fu, Y.; Fang, D.; Sun, H.; Fan, L.; Han, M.; et al. J. Mater. Chem. 2012, 22, 7461−7467.

24. Zhang, J.; Abbasi, F.; Claverie, J. Chem. - Eur. J. 2015, 21, 15142−15147.

25. Feng, J.; Liu, G.; Yuan, S.; Ma, Y. Phys. Chem. Chem. Phys. 2017, 19, 4997−5003.

26. Zeng, Z.; Zhang, W.; Arvapalli, D.; Bloom, B.; Sheardy, A.; Mabe, T.; Liu, Y.; Chevva, H.; Waldeck, D. H.; Wei, J.; Ji, Z. Phys. Chem. Chem. Phys. 2017, 19, 20101.

27. Li, X.; Zhang, S.; Kulinich, S. A.; Liu, Y.; Zeng, H. Sci. Rep. 2015, 4, 4976.

28. Fu, M.; Ehrat, F.; Wang, Y.; Milowska, K. Z.; Reckmeier, C.; Rogach, A. L.; Stolarczyk, J. K.; Urban, A. S.; Feldmann, J. Nano Lett. 2015, 15, 6030−6035.

29. Loukanov, A.; Sekiya, R.; Yoshikawa, M.; Kobayashi, N.; Moriyasu, Y.; Nakabayashi, S. J. Phys. Chem. C 2016, 120, 15867−15874.

30. Zhu, H.; Wang, X.; Li, Y.; Wang, Z.; Yang, F.; Yang, X. Chem. Commun. 2009, 5118− 5120.

31. Bukman, L.; Martins, A. C.; Barizão, É. O.; Visentainer, J. V.; Almeida, V. d. C. Food Anal. Methods 2013, 6, 1424−1432.

32. Solon, E.; Bard, A. J. J. Am. Chem. Soc. 1964, 86, 1926−1928.

33. Taylor, A. W.; Puttick, S.; Licence, P. J. Am. Chem. Soc. 2012, 134, 15636−15639.

34. Andrei, V.; Bunea, A.-I.; Tudorache, A.; Gáspár, S.; Vasilescu, A. Electroanalysis 2014, 26, 2677−2685.

35. Ahmed, S.; Tabassum, S.; Shakeel, F.; Khan, A. Y. J. Electrochem. Soc. 2012, 159, F103−F109.

36. Bhatti, N. K.; Subhani, M. S.; Khan, A. Y.; Qureshi, R.; Rahman, Turk. J. Chem. 2006, 30, 165−180.

37. Muhammad, H.; Tahiri, I. A.; Muhammad, M.; Masood, Z.; Versiani, M. A.; Khaliq, O.; Latif, M.; Hanif, M. J. Electroanal. Chem. 2016, 775, 157−162.

38. Scharifker, B. R. J. Electroanal. Chem. Interfacial Electrochem. 1988, 240, 61−76.

39. Abdullah, S.; Kamarudin, S. K.; Hasran, U. A.; Masdar, M. S.; Daud, W. R. W. J. Power Sources 2016, 320 , 111−119.

40. Paradas, M.; Campaña, A. G.; Jiménez, T.; Robles, R.; Oltra, J. E.; Buñ uel, E.; Justicia, J.; Cárdenas, D. J.; Cuerva, J. M. J. Am. Chem. Soc. 2010, 132, 12748 −12756

CHAPTER IV

ANTIOXIDATION CAPACITY OF NITROGEN AND SULFUR CODOPED CARBON NANODOTS

This chapter has been published as: Zhang, W., Chavez, J., Zeng, Z., Bloom, B. P., Sheardy, A., Ji, Z., ... & Wei, J. (2018). Antioxidant Capacity of Nitrogen, Sulfur Co-doped Carbon Nanodots. ACS Applied Nano Materials.

Introduction

Carbon nanodots (CNDs) display desirable properties for applications, including low toxicity, excellent photoluminescence, and good biocompatibility.[1–5] Both bottom-up and top down approaches have been used for the synthesis of CNDs.[6] Top-down approaches include chemical ablation, electrochemistry-based carbonization, and laser ablation, while bottom-up approaches include microwave irradiation and hydro- or solvothermal methods.[7–9] CNDs have been used in bioimaging and biosensing because of their excellent fluorescence and low cytotoxicity.[10,11] Photoluminescence has been attributed to the CNDs' conjugated π states, functional groups, and surface electronic states,[12] and it can be tuned by changes in their compositions and structures, as well as by doping with other nonmetallic elements.[13] For instance, Zhang's group has improved quantum yields by doping the CNDs with nitrogen.[14] Prato's group has reported new procedures for the synthesis of size- and surface-controllable and structurally defined, highly fluorescent N-doped CNDs.[15]

Electron-rich N atoms can shift the CNDs' electronic states and create additional active sites, which enhances the CNDs' photoluminescence intensity.[16] Both S-doped and N, S-codoped 42CNDs show enhanced fluorescence and photoluminescence 43quantum yields in bioimaging and sensing applications.[13,17,18] CNDs also show promise for protecting cells from oxidative stress. For example, superoxide or hydroxyl radicals were reported to be scavenged by CNDs that were prepared by using date molasses through microwave irradiation techniques.[19] Recently, the antioxidation activity of the N-doped CNDs was studied by embedding the CNDs in ionic liquid solutions, and the radical scavenging activity was ascribed to their rich amino surface.[20] Chong et al. synthesized graphene quantum dots and studied the difference in their oxidation activity in cells, both with and without light.[21] While some additional studies exist on the CNDs' antioxidation activity using cellular and chemical assays,[22−24] a better understanding of the antioxidation properties of CNDs is needed in order to facilitate their potential applications in biomedicine. To help elucidate their mechanism of action, the antioxidation activities of N,S codoped CNDs and their underlying antioxidation behaviors are examined herein using optical, electrochemical, and biochemical superoxide scavenging assays. The DPPH•-based assay is a commonly used method to evaluate the antioxidant activity.[25] Upon reaction with antioxidants in a solution, the deep-violet color of a DPPH• solution changes to light yellow with its conversion to the DPPH-H complex. This reaction progress was monitored by measuring the absorbance changes at 517 nm,[26,27] and the unreacted DPPH• concentration as a function of the CND concentration was evaluated by cyclic voltammetry.[26] Lucigenin-derived

chemiluminescence (lucigenin-CL) measurement is another powerful tool to investigate the superoxide scavenging capability in vitro related to mitochondria-derived reactive oxygen species (ROS).[28] Xanthine can be oxidized to uric acid upon the addition of the enzyme xanthine oxidase (XO). This reaction causes the production of O2•−.[29] Thus, XO is regarded as a biological superoxide radical source that plays a role in generating oxidative stress.[30] In the experiments presented herein, the xanthine/XO system is combined with lucigenin-CL measurements to evaluate the N, S-codoped CNDs' superoxide scavenging activity. We used a hydrothermal method to prepare the N, S codoped CNDs from three precursor molecules (α-lipoic acid + citric acid + urea). The purified CNDs were characterized with regard to morphology, elemental content, and optical properties. It is expected that the N and S doping in CNDs plays a synergistic role that enhances the fluorescence intensity of CNDs and increases their antioxidative activity because of the increase in the π-system electron density, which enhances the CNDs' electron-donating ability.[22] Compared with the aforementioned radical scavenging studies of CNDs,[19−26] this work reports some new findings on the antioxidation capacity of N,S-codoped CNDs for DPPH• free radicals and an unprecedented scavenging activity for ROS generated by the xanthine/XO system. The mechanistic reaction pathways for antioxidation are proposed based on their underlying reactivity and multiple assays using UV−vis spectroscopy and electrochemistry with DPPH• and lucigenin-CL. Additionally, the bioimaging of cells was performed using the CNDs'fluorescence at different excitation wavelengths, and the CNDs' biocompatibility was evaluated by a cytotoxicity study.

Methods and Matrials

Synthesis of N, S-Codoped CNDs: Figure 4.1 shows a general route to obtaining N, S-codoped CNDs. A hydrothermal method is applied to synthesize the CNDs using α-lipoic acid + citric acid + and urea as precursors. Briefly, deionized water (20 mL) was used to dissolve sodium hydroxide (0.36 g, Aldrich) to get a basic solution. Then, citric acid (0.2 g, 99%, Acros Organics), α-lipoic acid (0.6 g, 99%, Aldrich), and urea (1.0 g, 99.5%, Aldrich) were simultaneously added to the basic solution, forming a homogeneous yellow solution. This yellow solution was transferred to a Teflon reactor (50 mL volume, PPL-lined vessel chamber kettle, 250 °C) and heated to 230 °C for 18 h. Next, the aqueous reaction solution was cooled to room temperature, and it was purified using dialysis (1000 MWCO, Fisher Scientific) against deionized water for 24 h. The water was changed three times in order to aid in the dialysis. Last, a freeze-drying method (24 h in FreeZone 6, Labconco) was used to dry the resulting product. The final N, S-codoped CNDs' yield was measured to be 41.5 mg.

Characterization of N, S-Codoped CNDs: We used transmission electron microscopy (TEM; Carl Zeiss Libra 120 PLUS) and atomic force microscopy (AFM; Agilent 5600LS) to quantify the size and evaluate the morphology of the N, S-codoped CNDs (on a copper grid coated with carbon for TEM and a fresh mica for AFM). Fourier transform infrared spectroscopy (FTIR; Varian 670), Raman spectroscopy (Horiba XploRA ONE), and X-ray photoelectron spectroscopy (XPS; Thermo Fisher ESCALAB 250Xi) were used to examine the chemical structure and elemental content of the N, S-

codoped CNDs. UV−vis spectroscopy (Agilent Cary 6000i) and fluorescence spectroscopy (Agilent Cary Eclipse) were employed to study the optical properties of the N, S-codoped CNDs.

DPPH•: UV−Vis Spectroscopy-Based Assay: We used a UV−vis spectrometer to monitor the absorbance change at 517 nm and then to calculate the antioxidation activity of the N,S-codoped CNDs to DPPH• (Alfa Aesar).31 DPPH• was added into absolute methanol to obtain a solution concentration of 0.02 mg/mL for each measurement. Then, N,S-codoped CNDs with different concentrations were added into the DPPH• solutions and allowed to incubate in the dark for 2 h.

DPPH•: Electrochemistry-Based Assay: A three-electrode electrochemical cell (a gold working electrode, an Ag/AgCl reference electrode, and a platinum counter electrode; Fisher Scientific) was used to conduct the cyclic voltammetry under room temperature at different scan rates. The studied solutions (at pH = 7.4, 5 mL) contained 0.02 mg/mL DPPH• to which N, S-codoped CNDs were added at different concentrations, which was prepared using a 1:1 mixture solution by volume of absolute methanol (Fisher Scientific) and phosphate-buffered (PBS; pH = 7.0, Life Tech). As with the UV− vis studies, the DPPH• solution was incubated with N, S-codoped CNDs for 2 h in the dark prior to measurement.

Lucigenin-CL Study: Chemiluminescence (CL) was monitored with a BioTek microplate reader (Winooski, VT) at 37 °C for 30 min. For the enzyme system, the reaction mixture contained 100 μM xanthine (99%, Aldrich) and 10 mM XO (grade I, Aldrich) in 1 mL of a PBS solution (pH = 7.4) containing 0.1 mM

diethylenetriaminepentaacetic acid, and the reaction was initialized by adding 5 μL of lucigenin (5 μM). The superoxide scavenging activities of the N, S-codoped CNDs were analyzed by adding the N, S-codoped CNDs at different concentrations into the xanthine/XO system to quench the Lucigenin-CL emission intensity.

3-(4,5-Dimethylthiazol-2yl)-2,5-diphenyltetrazolium Bromide (MTT)-Based Assay: EA hy926 endothelial cells from ATCC (Manassas, VA) were cultured with Dulbecco's modified Eagle's medium (DMEM; Life Tech) containing fetal bovine serum (FBS; 10%) and penicillin−streptomycin (1%) at 37 °C in 5% CO 2 for 24 h. A 48-well culture plate was used to seed the cells, and their density was 1.5 × 105 per well. Then, Hank's balanced salt solution (HBSS media) was used to replace the culture medium containing different doses of N, S-codoped CNDs to culture cells for another 24 h. Afterward, 300 μL of a 0.2 mg/mL MTT (99%, Fisher Scientific) solution was added to each well culture plate. After incubation for 2 h at 37 °C, the cell culture plate was rinsed twice with 200 μL of PBS for each well and 300 μL of dimethyl sulfoxide was added. At room temperature, the resulting solution was shaken for 10 min. Finally, we measured the absorption at 570 nm with a BioTek microplate reader.

Multicolor Bioimaging: EA hy926 endothelial cells were seeded in an 8-chamber slide with DMEM containing 1% penicillin− streptomycin and 10% FBS at 37 °C in a 5% CO2 incubator for 24 h. DMEM was then removed, followed by the addition of the mixture of N,S-codoped CNDs (100 μg/mL) and the DMEM medium containing 0.5% FBS into each chamber, and the solution was allowed to incubate for 24 h. After that, the slide was rinsed by PBS twice to remove an extra medium and the N,S-codoped CNDs.

The CND incubated cells were fixed with 4% paraformaldehyde (Fisher Scientific). Cellular fluorescent images were obtained using an Olympus IX70 inverted fluorescence microscope.

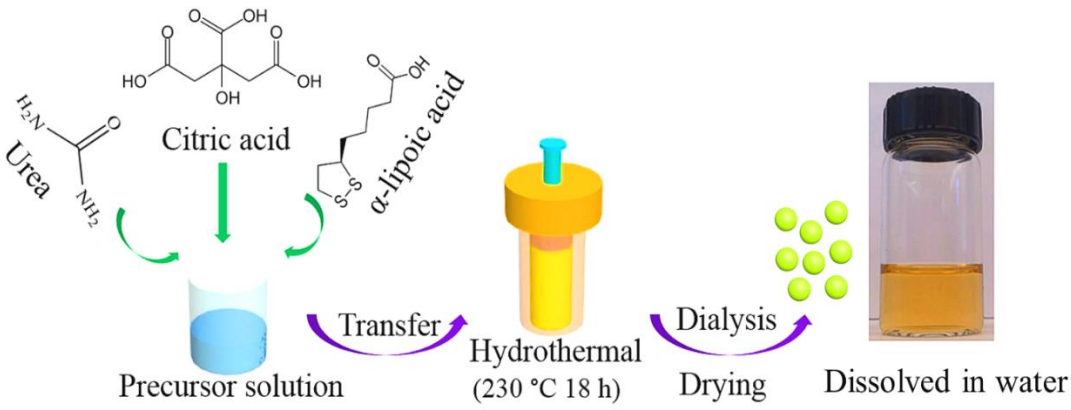

Figure 4.1 N, S Co-Doped CNDs Synthesis Scheme.

Results and Discussion

N, S co-doped CNDs synthesis and characterization**:** Transmission electron microscopy data (Figure 4.2A) and the associated size distribution (Figure 4.2B) indicate that the CNDs have an average size of about 3 nm. This finding is supported by atomic force microscopy data (Figure 4.2C) and the associated height profile analyses (Figure 4.2D). The FTIR spectra of the CNDs (Figure 4.2E) display broad bands at 3100-3400 cm^{-1}which are assigned to ν(N-H) and ν(O-H) stretching motions. The OH and NH functionalities add hydrophilicity to the CNDs, making them stable in aqueous solution. The FTIR signals at 764 (C-C), 1002 (C-S), 1179 (C-O), 1413 (C=C) and 1565 (C=O) cm^{-1} were assigned.[32-33] The Raman spectra (Figure 4.2F) give an I_D/I_G ratio of about

0.98, obtained from the intensities at 1347 cm^{-1} (D-bands, sp^3-hybridized) and 1562 cm^{-1} (G-bands, sp^2-hybridized), and this finding is consistent with a disordered graphite structure for the CNDs.[34] A C-S stretch transition was assigned to the 653 cm^{-1} transition.[35] XPS data (Figure 4.2G, 5.2H) corroborate the functionalities of the CNDs. Based on the C1s XPS spectra, five components were detected at 289.0 (O=C-OH), 287.8 (C=N & C=O), 286.6 (C-N & C-O), 285.6 (C-S), and 284.8 (C=C & C-C) eV, repectively.[36-37] The S 2p XPS spectrum was fitted to a sum of two doublets at 165.0 (C-S $S2p_{1/2}$), 163.7 (C-S $S2p_{3/2}$), 163.0 (S^{2-} $S2p_{1/2}$), and 161.7 (S^{2-} $S2p_{3/2}$) eV.[38-39] Altogether, these data indicate that the N,S co-doped CNDs have a spherical morphology with an average size of ~3 nm, that they possess a graphitic structure doped with N and S, and that they display surface functionalities of carboxylates and amines/amides. The 270 nm band in the absorption spectrum of Figure 4.2I, is assigned to the π-π^* transition of C=N bonds,[40-41] and the feature between 300 nm and 350 nm is attributed to surface states.[32, 42] Using a quinine sulfate reference for photoluminescence quantum yield measurements,[12] the relative quantum yield was measured to be 11% for the N, S co-doped CNDs.

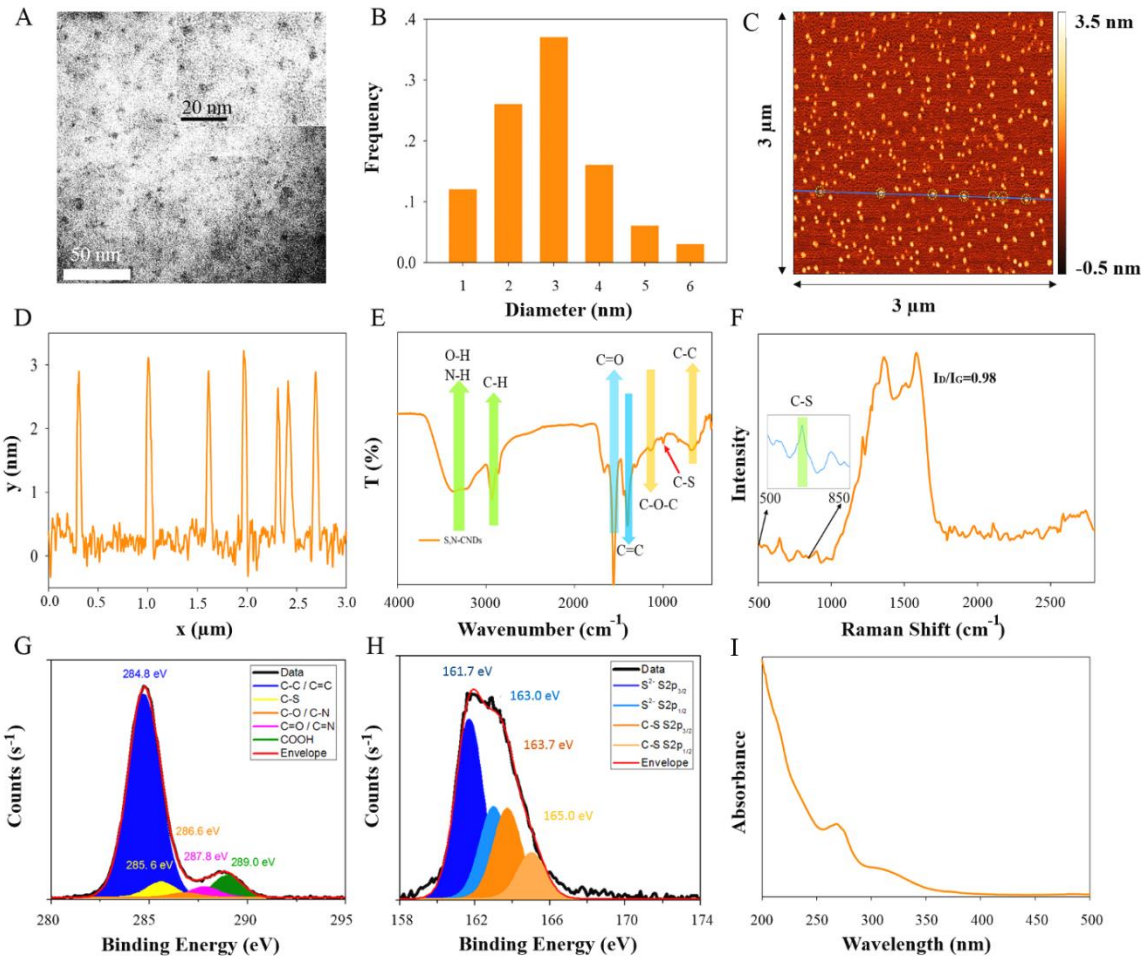

Figure 4.2 N, S Co-Doped CNDs Characterization Techniques. A) TEM images, B) size distribution based on the TEM image, C) AFM topography image, D) a representative height profile from the AFM image, E) FTIR spectra, F) Raman spectra, G-H) XPS spectrum (C 1s, S 2p), and I) UV-Vis absorption spectra.

DPPH• - UV-Vis based assay**:** UV-Vis spectroscopy of DPPH• was used to evaluate the antioxidation activity of the CNDs. In methanol solution, DPPH• is radical and the solution presents a dense violet color.[27] Upon addition of N, S co-doped CNDs, the solution color changes ; i.e., the absorbance intensity of the DPPH• methanol

solutions at 517 nm decreases (Figure 4.3A). The antioxidant activity can be calculated from the equation:

$$antioxidation \cdot activity = \frac{A_0 - A_c}{A_0} \times 100\% \quad (1)$$

in which, A_0 and A_c represent the absorbances of DPPH• at 517 nm without and with the N, S co-doped CNDs, respectively. The antioxidation activities of 16.2%, 39.0%, 70.0%, 88.4%, 92.9% are obtained (averaged value based on three trials) at the N, S co-doped CNDs concentration of 0.02, 0.03, 0.05, 0.07, 0.10 mg/mL, respectively. The DPPH• with the N, S co-doped CNDs incubation reaches its steady-state after 2 hours, and the solution's antioxidant activity increases when the concentration of N, S co-doped CNDs increases from 0.02 to 0.07 mg/mL. A plateau in the activity is found at higher concentrations of N, S co-doped CNDs (> 0.07 mg/mL) (Figure 4.3B). The concentration dependence of N, S co-doped CNDs is consistent with that of graphene quantum dots and some other types of CNDs.[21, 24, 26] Using the same hydrothermal method, CNDs from citric acid (CNDs without N, S doping) and from urea + citric acid (N doped CNDs) were prepared and evaluated by the DPPH• test . It was found that the N, S co-doped CNDs have the highest antioxidation activity. For example, at a 0.10 mg/mL incubation concentration, the antioxidation activity order is N, S co-doped CNDs (~92.9%, Figure 4.3B) > N doped CNDs (~71.1%) > CNDs without N, S doping (~34.6 %). Because the electronegativity of nitrogen (3.04 in Pauling scale) is larger than that of carbon (2.55 in Pauling scale), doping N onto carbon framework creates a high positive charge density on

the C atom,[43] facilitating the interaction between the N doped CNDs and DPPH•. Furthermore, the atomic radii of N (~0.65 Å) and C (~0.70 Å) are significantly smaller than that of S (~1.10 Å); such a significant size difference may induce Stone-Wales defects and strain in the carbon framework.[44] It has been reported that more catalytic sites could be generated for the oxygen reduction reaction due to the Stone-Wales defect generation in the carbon framework by doping S onto the reduced graphene oxide.[45] The defects generated in the carbon crystal lattice may serve as sites for the radical scavenging reduction reactions. Moreover, considering that the addition of S increases the CNDs' polarizability (N, S co-doped CNDs polarizability > N doped CNDs polarizability),[46] the N, S co-doped CNDs may act as a stronger electron donor, further facilitating the radical scavenging activity. Hence, one may conclude that the high antioxidation activity of the N, S doping may result from a synergistic effect of the electronegativity difference between C and N, S-induced active defect generation, and the high polarizability of S.

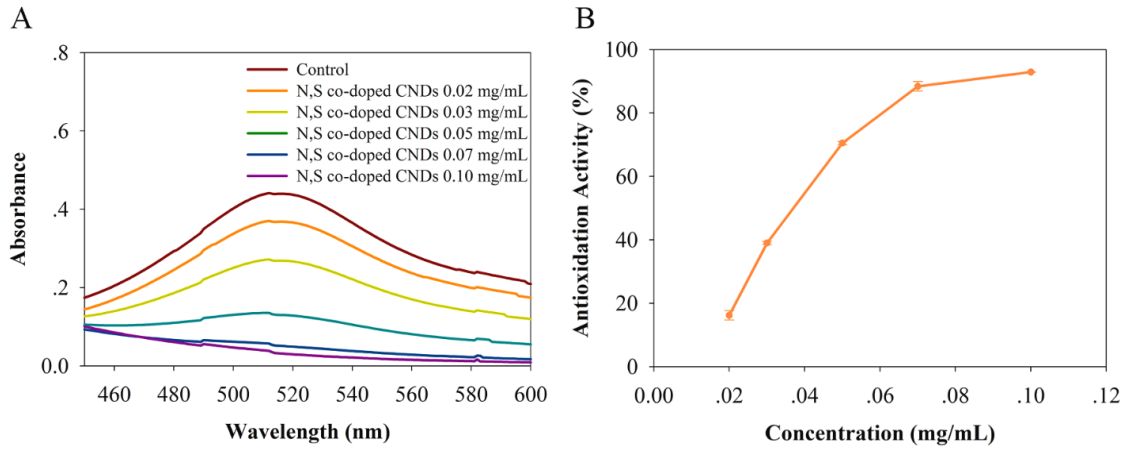

Figure 4.3. Optical DPPH• Test. (A) UV-Vis absorption spectra after incubating the N, S co-doped CNDs (from 0 to 0.10 mg/mL) into DPPH• solutions (0.02 mg/mL). (B) The antioxidation activity curve as a function of N, S co-doped CNDs concentration. The error bars are smaller than the symbol size.

DPPH-H is formed from the DPPH• by taking up a proton from the CNDs. This process can occur through a mechanism of hydrogen atom transfer (HAT),[26] involving the surface functional groups, like -COOH, of the CNDs acting as proton donors. Higher concentrations of CNDs, but below 0.1 mg/mL, decrease the concentrations of the free radical DPPH• as the redox species in the electrolyte.[26]

After incubation with different N, S co-doped CNDs, the cyclic voltammograms of DPPH• present different redox peak currents in the methanolic phosphate buffer solution (Figure 4.4). Control experiments, in the absence of DPPH•, do not show redox peaks in a methanolic PBS solution of 0.05 mg/mL N, S co-doped CNDs over the potential window (vs. Ag/AgCl) ranging from 0.0 to 0.7 V. This result agrees with recent studies on the redox properties and electronic states of CNDs whose redox reactions usually occur at more negative (less than -1.0 V) or more positive (> 0.7 V) potentials.[48-

[49] Hence, the redox peaks in Figure 4.4 result from an electrochemical reaction with DPPH•.[26] In another control experiment which used a DPPH• solution without CNDs, the cyclic voltammograms show that the redox peak currents obtained from DPPH• at a concentration of 0.01 mg/mL is much lower than that obtained from a solution with a DPPH• concentration of 0.02 mg/mL. The anodic/cathodic peak current magnitudes decrease as the concentration of N, S co-doped CNDs increase in solution; further substantiating our claim that N, S co-doped CNDs react with DPPH•. Note that a one-electron transfer process is supported by the full-width-at-half-maximum (FWHM) value of about 110 mV in the faradaic waves. A diffusion coefficient (D_0, cm^2/s) was extracted according to the relationship between the peak current, i_p (A), and the scan rate (V/s) by using the Randles-Sevcik formula; namely[50-51]

$$i_p = \left(2.69\times10^5\right) n^{3/2} A C D_0^{1/2} \nu^{1/2} \qquad (2)$$

where n is the number of electrons exchanged, A is electrode active area (0.043 cm^2), C represents DPPH• concentration (mol/mL), and ν is the voltage scan rate (V/s). D_0, the diffusion coefficient of DPPH•, was found to be 2.0×10^{-5} cm^2/s. The N, S co-doped CNDs concentration dependent slopes in Figure 4.5A and the diffusion coefficient determined by Eq. 2 were used to calculate the unreacted DPPH• concentrations in different solutions (Figure 4.5B). The free DPPH• concentration was found to be 31.8, 24.8, 18.2, 12.1, 6.6 nmol/mL at the N, S co-doped CNDs concentration of 0.02, 0.03, 0.05, 0.07, 0.10 mg/mL, respectively. In the end, we calculated the scavenging activity using the equation:

$$scavenging \cdot activity = \frac{C_0 - C_c}{C_0} \times 100\% \quad (3)$$

in which C_0 and C_c are the concentration of DPPH• without and with the incubation of N, S co-doped CNDs. The scavenging activity was calculated to be 38.9%, 52.2%, 65.1%, 76.7%, and 87.4%, (Figure 4.5C) for 0.02, 0.03, 0.05, 0.07, and 0.10 mg/mL concentrations of CNDs, respectively. These findings are corroborated by the antioxidation activity results shown in the UV-Vis spectroscopy experiments.

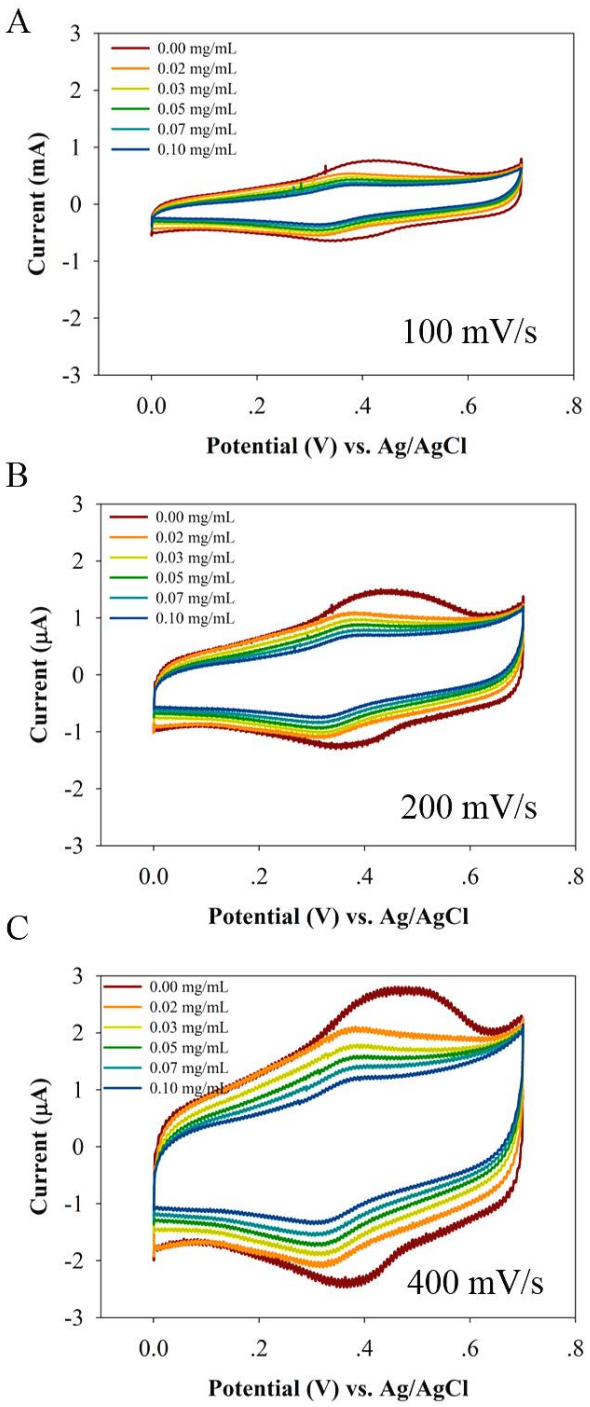

Figure 4.4 Electrochemistry Study. Cyclic voltammograms for the DPPH•-gold electrode system are shown as at different scan rates for different concentrations of N, S co-doped CNDs: 0.00, 0.02, 0.03, 0.05, 0.07, and 0.10 mg/mL.

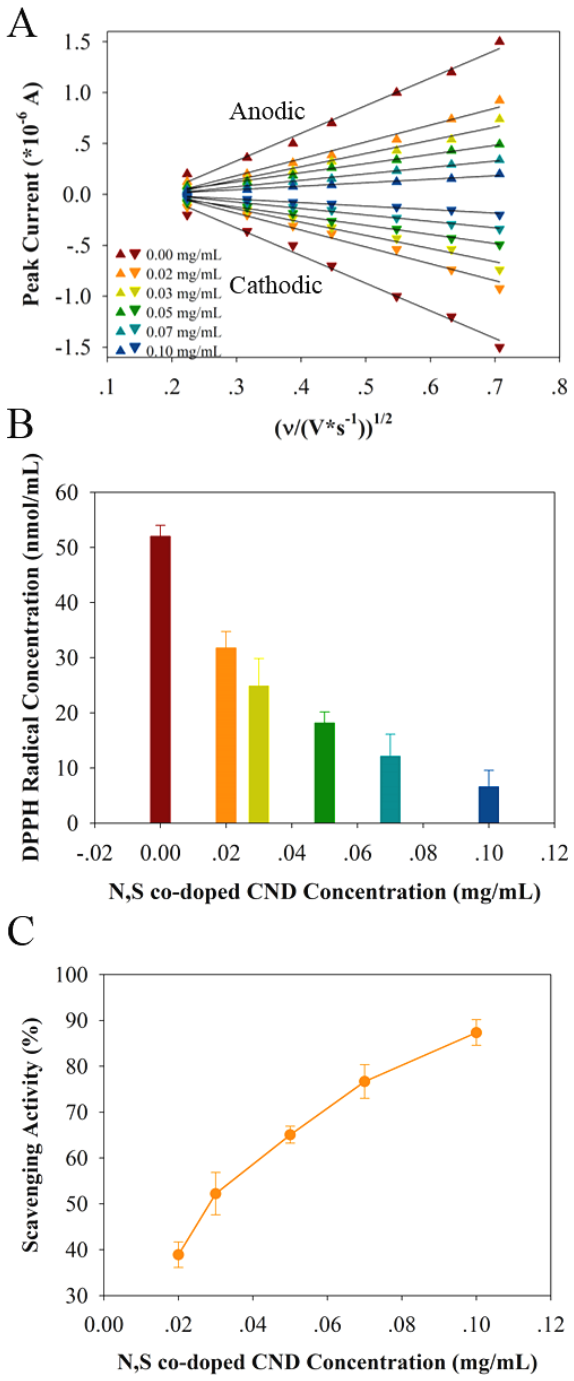

Figure 4.5 Unreacted DPPH• Concentration. (A) The linear dependence of peak currents on scan rates incubated with different N, S co-doped CND concentrations. (B) The reserved DPPH• concentration at different N, S co-doped CNDs concentrations. (C) Calculated scavenging activity versus N, S co-doped CNDs concentration.

Lucigenin-CL study for N, S co-doped CNDs: Lucigenin derived chemiluminescence has been widely used for biological and enzyme assays, especially for *in vitro* and *in vivo* superoxide detection.[52-53] XO can catalyze the oxidation of xanthine to uric acid and superoxide; a reaction believed to be involved in inflammatory disease.[54] Lucigenin is one of the chemiluminescence probes used for detecting superoxide production in various cellular systems.[28] Here, we used lucigenin as a chemiluminescence probe and XO as a ROS production source for measuring the superoxide scavenging activity of N, S co-doped CNDs. Figure 4.6A shows the lucigenin chemiluminescence quenching as a function of N, S co-doped CND concentration. The lucigenin-derived chemiluminescence intensity decreases with increasing N, S co-doped CND concentration until it reaches a plateau at concentrations of 0.05 mg/mL and higher for N, S co-doped CNDs. The intensity of lucigenin-CL is quenched by about 59% at 0.10 mg/mL of N, S co-doped CNDs (Figure 4.6B). The antioxidation activity that is found for N, S co-doped CNDs in DPPH• solution from UV-Vis and electrochemical studies is more efficient than the scavenging activity for ROS that is observed in the lucigenin-CL experiments (e.g. 90% vs. ~ 59% for N, S co-doped CNDs concentration of 0.10 mg/mL).

Figure 4.7 illustrates the proposed antioxidation reaction pathways for the lucigenin-CL quenching by CNDs. Univalent reduction of lucigenin generates the lucigenin cation radical, and it may react with XO derived ROS (i.e. the superoxide $O_2^{\bullet-}$) to generate the lucigenin dioxetane.[55] Two N-methylacridone molecules can be formed by the decomposition of this unstable dioxetane intermediate; one of them forms as the

electronically excited state and can emit a photon to relax to the ground state.[56] It is anticipated that the synergistic effect of N (electronegativity difference induced high electron density) and S (size difference induced defects generation and high polarization of S) doping promotes the conjugated π-system to act as an electron donor (Figure5.7),[22] allowing the N, S co-doped CNDs to work as superoxide scavengers and reduce the concentration of XO derived $O_2^{\bullet-}$ superoxide (Figure 4.7, step 1). This process will inhibit the reaction between the lucigenin cation radical and the superoxide, decreasing the formation of the dioxetane intermediate (Figure 4.7, step 2). Consequently, the lucigenin chemiluminescence is quenched by the addition of N, S co-doped CNDs (Figure 4.7, step 3). Because higher concentrations of N, S co-doped CNDs result in higher superoxide scavenging activity, a lower intensity of lucigenin-CL is observed. These results are corroborated by the DPPH assay. To the best of our knowledge, this is the first instance where N, S co-doped CNDs have been shown to act as an antioxidant in enzyme generated ROS scavenging.

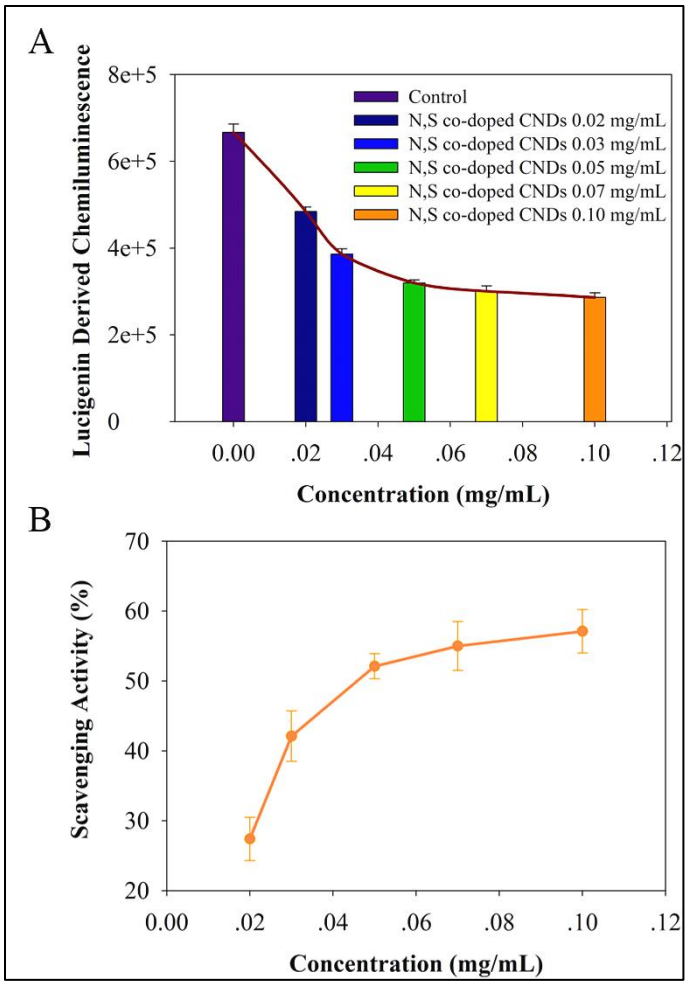

Figure 4.6. Superoxide Scavenging. (A) Superoxide scavenging activities of different concentrations of N, S co-doped CNDs measured by xanthine/XO system induced Lucigenin-CL, the control is without N, S co-doped CNDs treatment. (B) The calculated scavenging activity versus N, S co-doped CNDs concentration.

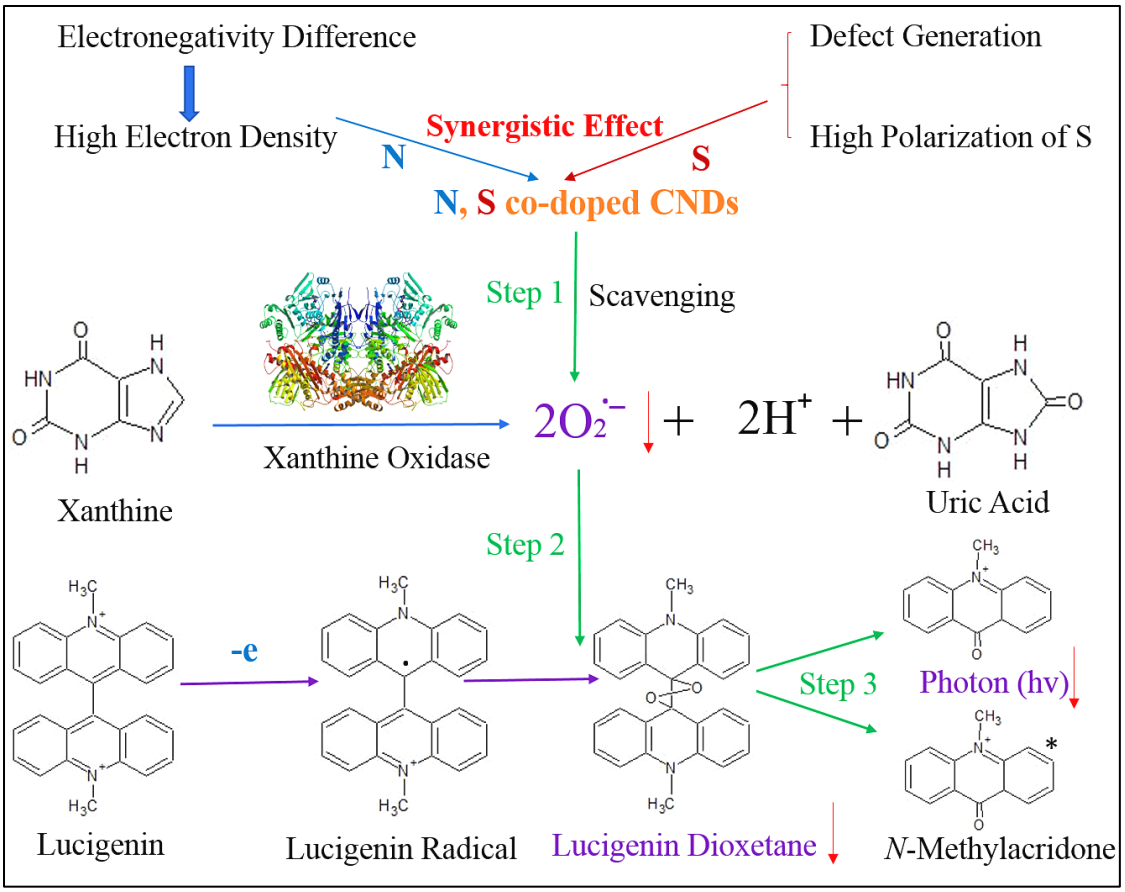

Figure 4.7. Lucigenin-CL Quenching Pathway. Schematic illustration of the reaction pathways of ROS scavenging by N, S co-doped CNDs in the xanthine /XO system and Lucigenin-CL quenching process.

N, S co-doped CNDs cytotoxicity study: The biocompatibility of N, S co-doped CNDs was evaluated by an MTT based assay. For this system, mitochondrial activity is indicated by the MTT conversion to formazan crystals by living cells.[57] We performed the MTT assay in EA. hy926 endothelial cells incubated with 0.02, 0.03, 0.05, 0.07, or 0.10 mg/mL of N, S co-doped CNDs. Figure 4.8A shows high cell viability (>90%) when incubated with 0.1 mg/mL N, S co-doped CNDs for 24 hours. Figure 4.8B shows the formation of formazan crystals in the cells in the absence of N, S co-doped CNDs

treatment. When the N, S co-doped CNDs were added, however, the number density of formazan crystals in the images does not change much, both for low (Figure 4.8C) and high (Figure 4.8D) concentrations of N, S co-doped CNDs concentrations. These observations indicate that the N, S co-doped CNDs exhibit good biocompatibility.

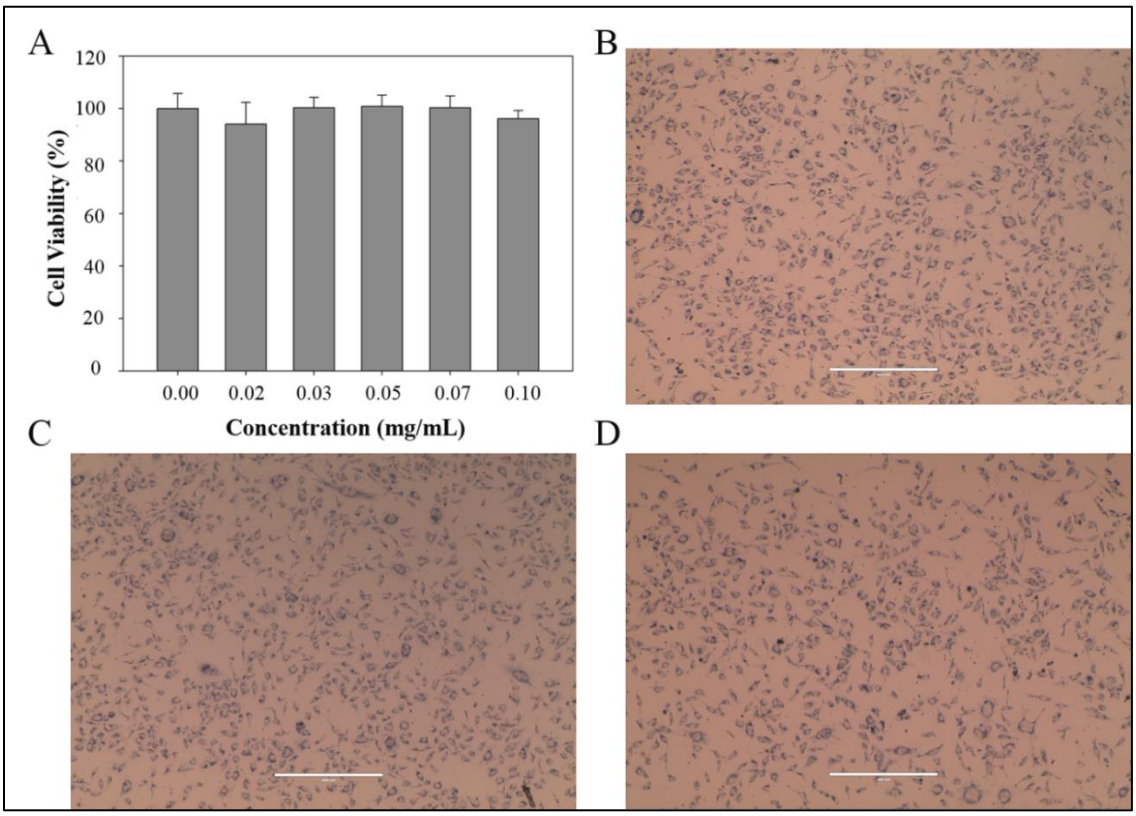

Figure 4.8. MTT Assay. (A) For cell viability value (%) measured at different concentrations of N, S co-doped CNDs treatment to EA. hy926 endothelial cells for 24 hours. EA. hy926 endothelial cells under MTT assay images were taken via microscope with different concentrations of N, S co-doped CNDs incubation, (B) cells without N, S co-doped CNDs incubation (C) cells with 0.02 mg/mL N, S co-doped CNDs incubation (D) cells with 0.10 mg/mL N, S co-doped CNDs incubation. All scale bars represent 200 μm.

N, S co-doped CNDs fluorescence and cell imaging**:** CNDs have been used as a fluorescent label in bioimaging applications because of their excitation-dependent photoluminescence.[58-59] Figure 4.9A shows the fluorescence emission spectra of the dissolved N, S co-doped CNDs in deionized water as a function of the excitation wavelengths. The maximum emission peak at 408 nm occurs for an excitation wavelength of 350 nm. Longer wavelength excitation renders a red-shift in the fluorescence emission spectra, which has been investigated by others.[60-61] Microscopy is an essential tool for biological and biomedical imaging studies,[62] and in this study, an Olympus IX70 inverted fluorescence microscope was used to monitor the cellular uptake of N, S co-doped CNDs by EA. hy926 endothelial cells after incubation with 0.10 mg/mL N, S co-doped CNDs for 24 hours (Figure 4.9B-D). According to the MTT assay results, the cell viability is still over 90% after 24 hours with 0.10 mg/mL N, S co-doped CNDs. The strong blue fluorescence indicates that N, S co-doped CNDs are internalized by the EA. hy926 endothelial cells. The intensity of the green fluorescence and red fluorescence from cells is weaker because the intensity of emission for N, S co-doped CNDs weakens as the observation wavelength is red-shifted.

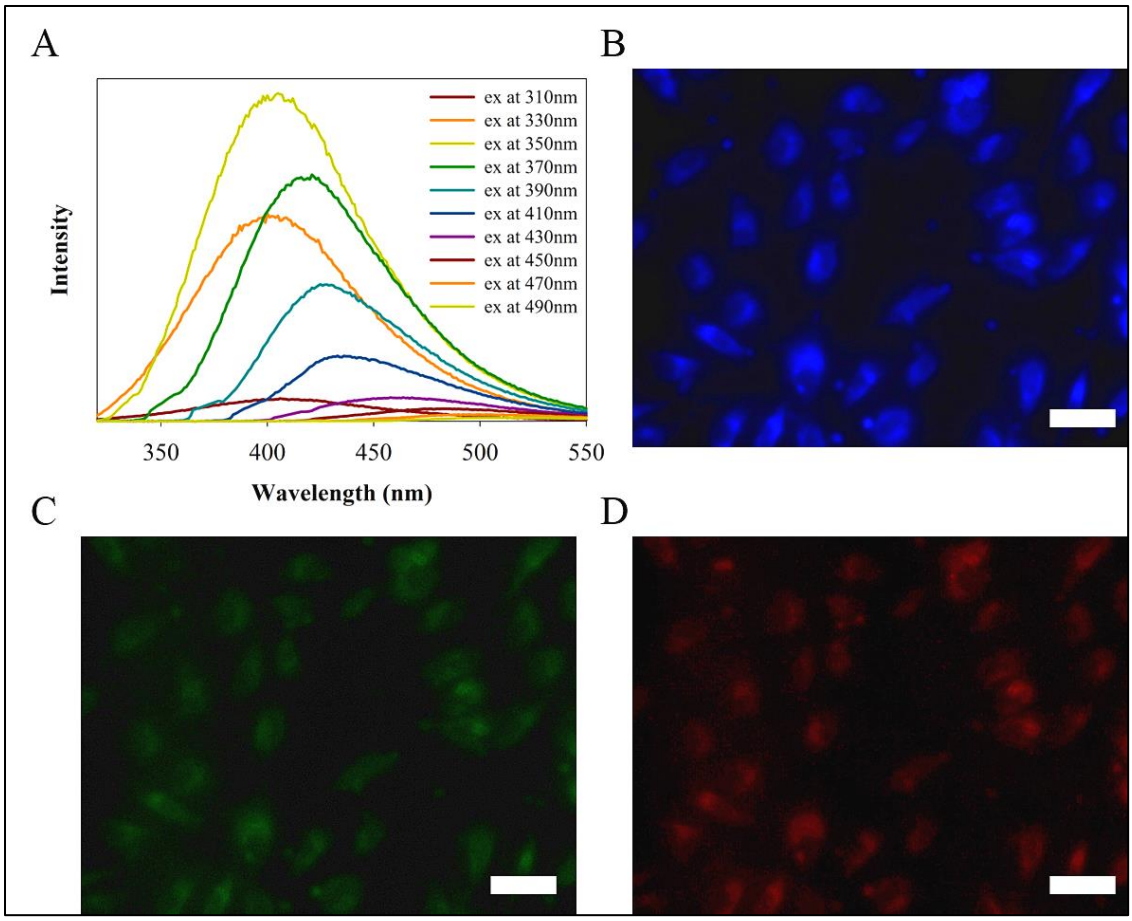

Figure 4.9. Fluorescence Microscopy Images. (A) Fluorescence emission spectra of the N, S co-doped CNDs in deionized water. Fluorescence images of EA. (B-D) Optical images of hy926 endothelial cells with the treatment (24 hours) of 100 μg/mL N, S co-doped CNDs at the excitation wavelength of 360 nm (B), 470 nm (C), and 560 nm (D). All scale bars represent 50 μm.

Conclusion

This work explored the antioxidation activity of N, S co-doped CNDs by three different methods: UV-Vis absorption of DPPH•, electrochemistry using DPPH•, and lucigenin-CL assay of enzyme generated ROS. The electrochemically-derived relationship between unreacted DPPH• and the CND concentration agrees reasonably

well with the UV-Vis absorption dose-dependent results, and the redox reaction is explained by the HAT mechanism. We also proposed a reaction pathway for the xanthine /XO system induced lucigenin-CL quenching by the ROS scavenging reaction of N, S co-doped CNDs. Combined with the biocompatibility and bioimaging capabilities, these results provide promise for development of alternative treatment options not possible with traditional pharmacological and ROS scavenger approaches, suggesting a new "nanopharmacology" for more effective treatment of inflammatory disorders such as atherosclerosis.

References

1. Zhu, S.; Meng, Q.; Wang, L.; Zhang, J.; Song, Y.; Jin, H.; Zhang, K.; Sun, H.; Wang, H.; Yang, B. Angew. Chem., Int. Ed. 2013, 52, 3953−3957.
2. Lim, S. Y.; Shen, W.; Gao, Z. Chem. Soc. Rev. 2015, 44, 362−381.
3. Zheng, X. T.; Ananthanarayanan, A.; Luo, K. Q.; Chen, P. Small 2015, 11, 1620−1636.
4. Liu, D.; Qu, F.; Zhao, X.; You, J. J. Phys. Chem. C 2015, 119, 17979−17987.
5. Wang, Y.; Hu, A. J. Mater. Chem. C 2014, 2, 6921−6939.
6. Li, X.; Rui, M.; Song, J.; Shen, Z.; Zeng, H. Adv. Funct. Mater. 2015, 25, 4929−4947.
7. Xu, Q.; Wei, J.; Wang, J.; Liu, Y.; Li, N.; Chen, Y.; Gao, C.; Zhang, W.; Sreeprased, T. S. RSC Adv. 2016, 6, 28745−28750.
8. Kumar, V. B.; Borenstein, A.; Markovsky, B.; Aurbach, D.; Gedanken, A.; Talianker, M.; Porat, Z. J. Phys. Chem. C 2016, 120, 13406−13413.
9. Jiang, H.; Chen, F.; Lagally, M. G.; Denes, F. S. Langmuir 4112010 , 26, 1991−1995.
10. Xu, Z.-Q.; Lan, J.-Y.; Jin, J.-C.; Dong, P.; Jiang, F.-L.; Liu, Y. ACS Appl. Mater. Interfaces 2015, 7, 28346−28352.
11. Das, B.; Dadhich, P.; Pal, P.; Srivas, P. K.; Bankoti, K.; Dhara, S. J. Mater. Chem. B 2014, 2 , 6839−6847.
12. Sachdev, A.; Gopinath, P. Analyst 2015, 140, 4260 −4269.
13. Zhao, S.; Lan, M.; Zhu, X.; Xue, H.; Ng, T.-W.; Meng, X.; Lee, 425C.-S.; Wang, P.; Zhang, W. ACS Appl. Mater. Interfaces 2015, 7, 17054− 17060.
14. Foti, M. C.; Daquino, C.; Geraci, C. J. Org. Chem. 2004, 69, 2309−2314.
15. Jha, N. S.; Mishra, S.; Jha, S. K.; Surolia, A. Electrochim. Acta 4352015 , 151, 574−583.
16. Khoshtariya, D. E.; Dolidze, T. D.; Zusman, L. D.; Waldeck, D. H. J. Phys. Chem. A 2001, 105, 1818 −1829.

17. Qu, S.; Wang, X.; Lu, Q.; Liu, X.; Wang, L. Angew. Chem., Int. Ed. 2012, 51, 12215−12218.

18. Garcia, E. J.; Oldoni, T. L. C.; Alencar, S. M. d.; Reis, A.; 446Loguercio, A. D.; Grande, R. H. M. Braz.Dent. J. 2012, 23, 22 −27.

19. Cui, Q.; Xu, J.; Wang, X.; Li, L.; Antonietti, M.; Shalom, M. Angew. Chem., Int. Ed. 2016, 55, 3672 −3676.

20. Lim, C. S.; Hola, K.; Ambrosi, A.; Zboril, R.; Pumera, M. Electrochem. Commun. 2015, 52, 75 −79.

21. Muthulingam, S.; Bae, K. B.; Khan, R.; Lee, I.-H.; Uthirakumar, P. RSC Adv. 2015, 5, 47−46251.

22. Hou, H.; Banks, C. E.; Jing, M.; Zhang, Y.; Ji, X. Adv. Mater. 2015, 27, 7861−7866.

23. Zhang, M.; Bai, L.; Shang, W.; Xie, W.; Ma, H.; Fu, Y.; Fang, D.; Sun, H.; Fan, L.; Han, M.; et al. J. Mater. Chem. 2012, 22, 7461−7467.

24. Zhang, J.; Abbasi, F.; Claverie, J. Chem. - Eur. J. 2015, 21, 15142−15147.

25. Feng, J.; Liu, G.; Yuan, S.; Ma, Y. Phys. Chem. Chem. Phys. 2017, 19, 4997−5003.

26. Zeng, Z.; Zhang, W.; Arvapalli, D.; Bloom, B.; Sheardy, A.; Mabe, T.; Liu, Y.; Chevva, H.; Waldeck, D. H.; Wei, J.; Ji, Z. Phys. Chem. Chem. Phys. 2017, 19, 20101.

27. Li, X.; Zhang, S.; Kulinich, S. A.; Liu, Y.; Zeng, H. Sci. Rep. 2015, 4, 4976.

28. Fu, M.; Ehrat, F.; Wang, Y.; Milowska, K. Z.; Reckmeier, C.; Rogach, A. L.; Stolarczyk, J. K.; Urban, A. S.; Feldmann, J. Nano Lett. 2015, 15, 6030−6035.

29. Loukanov, A.; Sekiya, R.; Yoshikawa, M.; Kobayashi, N.; Moriyasu, Y.; Nakabayashi, S. J. Phys. Chem. C 2016, 120, 15867−15874.

30. Zhu, H.; Wang, X.; Li, Y.; Wang, Z.; Yang, F.; Yang, X. Chem. Commun. 2009, 5118− 5120.

31. Bukman, L.; Martins, A. C.; Barizão, É. O.; Visentainer, J. V.; Almeida, V. d. C. Food Anal. Methods 2013, 6, 1424−1432.

32. Solon, E.; Bard, A. J. J. Am. Chem. Soc. 1964, 86, 1926−1928.

33. Taylor, A. W.; Puttick, S.; Licence, P. J. Am. Chem. Soc. 2012, 134, 15636−15639.

34. Andrei, V.; Bunea, A.-I.; Tudorache, A.; Gáspár, S.; Vasilescu, A. Electroanalysis 2014, 26, 2677−2685.

35. Ahmed, S.; Tabassum, S.; Shakeel, F.; Khan, A. Y. J. Electrochem. Soc. 2012, 159, F103−F109.

36. Bhatti, N. K.; Subhani, M. S.; Khan, A. Y.; Qureshi, R.; Rahman, Turk. J. Chem. 2006, 30, 165−180.

37. Muhammad, H.; Tahiri, I. A.; Muhammad, M.; Masood, Z.; Versiani, M. A.; Khaliq, O.; Latif, M.; Hanif, M. J. Electroanal. Chem. 2016, 775, 157−162.

38. Scharifker, B. R. J. Electroanal. Chem. Interfacial Electrochem. 1988, 240, 61−76.

39. Abdullah, S.; Kamarudin, S. K.; Hasran, U. A.; Masdar, M. S.; Daud, W. R. W. J. Power Sources 2016, 320 , 111−119.

40. Paradas, M.; Campaña, A. G.; Jiménez, T.; Robles, R.; Oltra, J. E.; Buñ uel, E.; Justicia, J.; Cárdenas, D. J.; Cuerva, J. M. J. Am. Chem. Soc. 2010, 132, 12748 −12756.

CHAPTER V

A STUDY OF CELLULAR UPTAKE OF CARBON NANODOTS: TIME AND CONCETRATION DEPENDENT NULCEAR PENETRABILITY

Introduction

Carbon nanodots (CNDs) are composed of functional groups, amorphous carbon frames and polyatomic carbon domains.[1-2] CNDs can be synthesized by the techniques of microwave irradiation, hydrothermal or solvothermal treatment, laser ablation, electrochemical carbonization and chemical ablation.[3-4] CNDs are reported to have potential applications in photoelectric devices, chemical sensing, and biomedicine owing to their superior water solubility, biocompatibility, tunable photoluminescence and opto-electronic properties.[5-7]

A lot of efforts have been made to investigate CNDs for biomedicine applications. Wu et al. developed a multi-functionalized CNDs targeting lung cancer cells which performed good anti-cancer effect.[8] Nandi's group reported single molecule detection in nucleus using CNDs.[9] Dekaliuk's lab used CNDs to visualize cellular functioning process such as apoptosis.[10] For such biomedical applications, the interaction of the CNDs with cells is critical for improving the performance; Recent reports concluded that targeted nuclear delivery would show enhanced therapeutic effects.[11] Some kinds of nanoparticles sizing between 10 and 100 nm (gold, silver, silicon, etc.) have been studied and the conclusion of nanoparticles with the diameter of 50 nm showed the highest cell uptake

has been pointed out.[12-15] Due to a good fit with the cellular pore size, other kinds of nanoparticles with size of 5 nm to 10 nm (gold, silver, silicon, etc.) obtain a higher cellular penetration.[16-18] More importantly, small nanoparticles can be located in endosomes, lysosomes, cell cytoplasm and nucleus.[19] The mechanisms of CNDs uptake maybe different due to smaller size of CNDs (1-5nm).

Fluorescence microscopy, among other techniques, is an useful tool that enables the tracking of nanoparticles uptake and mapping out their trafficking route during analysis of cell-nanoparticle interaction.[20] This technique uses specific excitation wavelength of a sample, which can be either fluorescently marked or intrinsically fluorescent, to generate the emission signal.[21] The emission wavelength of CNDs, which ranges from blue to red, can be modified by 1) adjusting preparation conditions, 2) increasing surface oxidation degree, 3) doping different elements or 4) controlling the size. Fluorescence microscopy has been widely used in the imaging of the CNDs incubated cells.[22-24] However, limitations of fluorescence microscopy exist: the fluorescent labels might be quenched or bleached,[25] the characteristic of the labeled nanoparticles may change,[26] cross talk may happen between different channels when multiple channels are used to observe the nanoparticles and cellular comparts.[27] To avoid these potential problems and get a better understanding of CNDs cellular uptake, we used an enhanced dark field microscope with hyperspectral imaging software.

In this study, we demonstrate the effects of incubation time and concentration of CNDs on their penetrations into cell nucleus with a hyperspectral microscopy technology and quantitatively determine the light signals in the nucleus. The mechanism behind

CNDs penetration is also discussed based on their concentration-dependency. These findings represent a significant contribution to applications of CNDs in drug delivery system, single molecule detection and live cell imaging.

Methods and Materials

Synthesis of CNDs: Ethylenediamine and citric acid can be used as nitrogen and carbon precursors in CNDs synthesis[28]. They were used to synthesize CNDs by a microwave-assisted method. Citric acid (0.96 g, 99%, ACROS Organics) and ethylenediamine (1mL, 99%, Alfa Aesar) were mixed together in 1.0 mL deionized water to form a homogenous solution. We then use a microwave synthesizer (CEM Corp 908005) to heat the solution with 300 W for 15 minutes. We then used a dialysis membrane (1000 MWCO, Fisher Scientific) against deionized water to purify the reddish-brown solution for 24 h, we changed the dialysis water three times. Lastly, we used a freeze-dryer (FreeZone 6, Labconco) to dry the resultant solution for 24 h to obtain the solid sample.

Characterization of CNDs: We used an atomic force microscope (5600LS AFM, Agilent) to test the size and morphology of the CNDs on a fresh mica. We then studied the chemical structure and elemental content of the CNDs with Fourier transform infrared spectroscopy (670 FTIR, Varian), X-ray photoelectron spectroscopy (XPS, Thermo Fisher ESCALAB 250 Xi) and X-ray powder diffraction (XRD, Agilent Technologies Oxford Gemini). We studied the optical properties of the CNDs with UV-Vis

spectroscopy (Cary 6000i, Agilent) and fluorescence spectroscopy (Cary Eclipse, Agilent).

Cell culture: Human A549 cells (ATCC, CCL-185) were seeded in the growth medium F-12K (Kaighn's Modification of Ham's F-12 medium) (ATCC, 30-2004) supplemented with 10% fetal bovine serum (Sigma Aldrich) and 1% streptomycin-penicillin (Fisher Scientific) in a T-75 flask at 37 °C and 5% CO_2 in a cell incubator for 70%~90% confluent. The cells were then grown on coverslips in a 12 well plate in cell incubator at 37 °C and 5% CO_2 for 24 h to allow them to fully spread. After that, we treated the cells on each well plate with 750 μg/mL CNDs for durations of 0 h, 0.5 h, 2 h, 6 h, 10 h and 24 h respectively. For the concentration-dependent experiments, we treated the cells for 24 h and with different CNDs doses ((0 μg/mL, 75 μg/mL, 225 μg/mL, 450 μg/mL, 750 μg/mL and 1200 μg/mL).

Sample fixation: Once the cells were treated, each well were washed by PBS (Thermo fisher, pH 7.4) twice, then the cells cultured on the coverslips were fixed with 4% Paraformaldehyde solution for 15 minutes at room temperature. We rinsed off the paraformaldehyde by washing with PBS for three times. We mounted coverslips on glass slides by using a small drop of mounting media (Polysciences, *Inc*.). The samples were stored at 4 °C in dark environment before imaging).

Optical imaging and hyperspectral imaging: Enhanced dark field microscope optics (CytoViva, Inc., Alabama) can enable users to image nanomaterials by improving signal-to-noise ratio more than ten times compared to standard dark field microscope. This microscope was used to observe CNDs uptake of A549 cells. The images were

obtained by a 60X immersion oil objective. The hyperspectral signal was then acquired at the same glass slide position with a CCD camera under a wide light source. The hyperspectral signal for data analysis was output via the ENVI software and the optical images were obtained with the Ocular software.

Results and Discussion

CNDs characterization**:** Atomic force microscopy data (Figure 5.1A) indicates that the CNDs have an averaged size of about 2 nm. According to the FTIR spectra (Figure 5.1B), ν(O-H) and ν(N-H) can be obtained due to the presence of broad bands (from 3100 cm^{-1} to 3400 cm^{-1}), which is evidence that the CNDs are hydrophilic and stable in aqueous solution.[29] The FTIR signals at 690 (C-C), 1185 (C-O),1375 (C=C) and 1550 (C=O) cm^{-1} can also be assigned respectively.[30-31] Four components could be obtained by the XPS data (Figure 5.1C): C-C and C=C (284.8 eV, 67.3%), C-O and C-N (286.4 eV, 23.6%,), C=O and C=N (287.8 eV, 5.7%), and COOH (289.0 eV, 3.4%).[7] A graphite structure is also present as indicated by the full width at half maximum (FWHM) of about 4.1° in the main diffraction peak that appeas at 22.8° in the XRD spectrum (Figure 5.1D). Figure 5.1E shows the absorption features. The π -π* transitions of C-C and C=C and n-π* transition of the C=O moieties can be seen at about 235 nm and 350 nm respectively[32] and the feature between 400 nm and 500 nm is attributed to surface states.[33] Under different excitation conditions (λ_{ex} in the range of 290 - 410 nm), Figure 5.1F shows the fluorescence emission spectra by dissolving CNDs in deionized water.

The peak intensity at 450 nm occurs when the excitation wavelength is at 370 nm. Note that the concentration of CNDs for UV-Vis and fluorescence is 0.05 mg/mL.

Light intensity measurements under CNDs incubation with different time: The light intensity measurements for the CNDs penetration is based on the CytoViva technology with high signal-to-noise optimized darkfield based images created with an oblique angle lighting.[34] Different from the super-resolution fluorescence microscopy, transmission electron microscopy, atomic force microscopy and scanning electron microscopy used to probe the cellular interactions of nanoparticles, spectra from the CNDs can be automatically captured by the integrated CytoViva hyperspectral imaging system in order to record and determine whether CNDs are present in the nucleus region. The cells were incubated with a concentration of 750 μg/mL of CNDs with different incubation times.

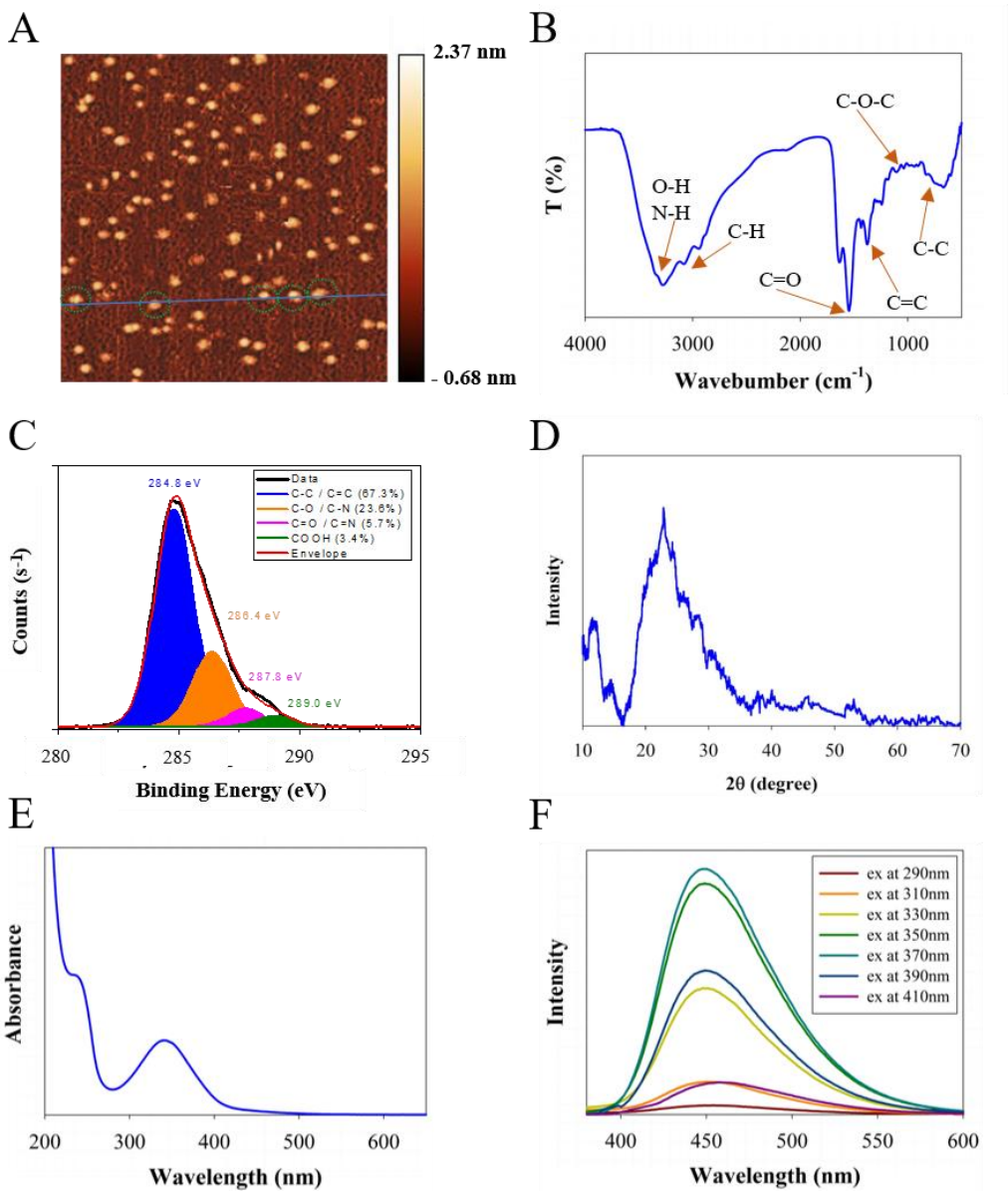

Figure 5.1. CNDs Characterization Results. A) AFM topography image, B) FTIR spectra, C) XPS signal (C 1s), D) XRD data, E) UV-Vis absorption spectra, and F) fluorescence emission spectra.

The nucleus structure can be clearly seen in the cells without CNDs incubation (Figure 5.2A). It is hypothesized that, without regulation, the CNDs can enter the nucleus, forming bright region in the nucleus, shown in the dark-field images, due to the

high scattering cross-section. The ethylenediamine and citric acid precursors introduce amino and carboxyl groups to the CNDs, which allows the CNDs to distribute more uniformly in the incubation process and to cover the nuclear pore complex (NPC) for penetration. There are three basic mechanisms for CNDs entering cells: 1) endocytosis, 2) penetration through channels and 3) direct diffusion across the plasma membrane.[35-36] An analysis of CNDs penetration into the nucleus was conducted with a concentration of 750 μg/mL for various times ranging from 0.5 h to 24 h after the cells were washed by PBS (pH 7.4) twice for each well and then fixed with 4% Paraformaldehyde solution for 15 minutes at room temperature. The nucleus' structure and the presence of CNDs were indicated by the bright colors on black background (Figure 5.2B-F). When penetration starts, weak light signals form at the center of the cells and were uniformly distributed (Figure 5.2B-C). As the process continues, the light signals intensify at the center of the cells (Figure 5.2D-F).

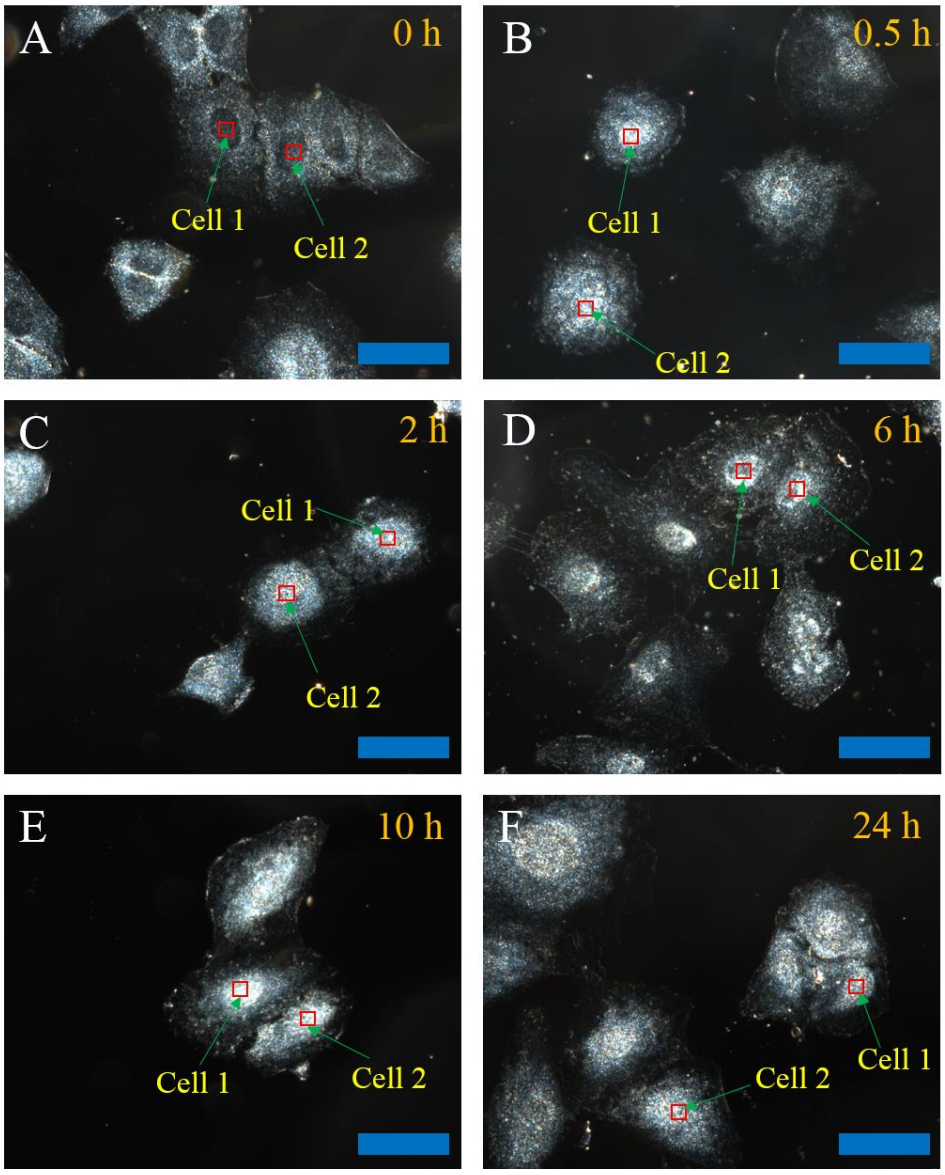

Figure 5.2. Time Dependent Dark Field Images. Dark-field images of cells incubated without CNDs (A) or with 750 μg/mL of CNDs for different incubation times from 0.5 h to 24 h (B-F). All of the scale bars are 4 μm.

In order to quantitatively determine the light signals in the nucleus, we measured the hyperspectral signal via the ENVI software (Figure 5.3) based on 10 points in two cells as marked in Figure 5.2 and recorded the peak light intensities as shown in Figure

5.4. The data analysis shows a monotonic increase in nuclear concentration of CNDs with the increase of the incubation time (Figure 5.3A-F). After incubation for 0.5 h, the background light intensity is enhanced by the addition of CNDs increases from 89 a.u to 380 a.u. (Figure 5.4). CNDs penetration in the range of 0-6 h incubation time shows an increase in light intensity but does not show obvious increase beyond 6 h incubation time, a feature that is consistent with another report[37] using fluorescence imaging. The hyperspectral signal via the ENVI software focusing on the nucleus in a control group, where no CNDs were used, were collected. These data corroborate the inference that the CNDs can penetrate the nucleus and the largest signal with 750 μg/mL of CNDs is obtained with 6 h incubation time.

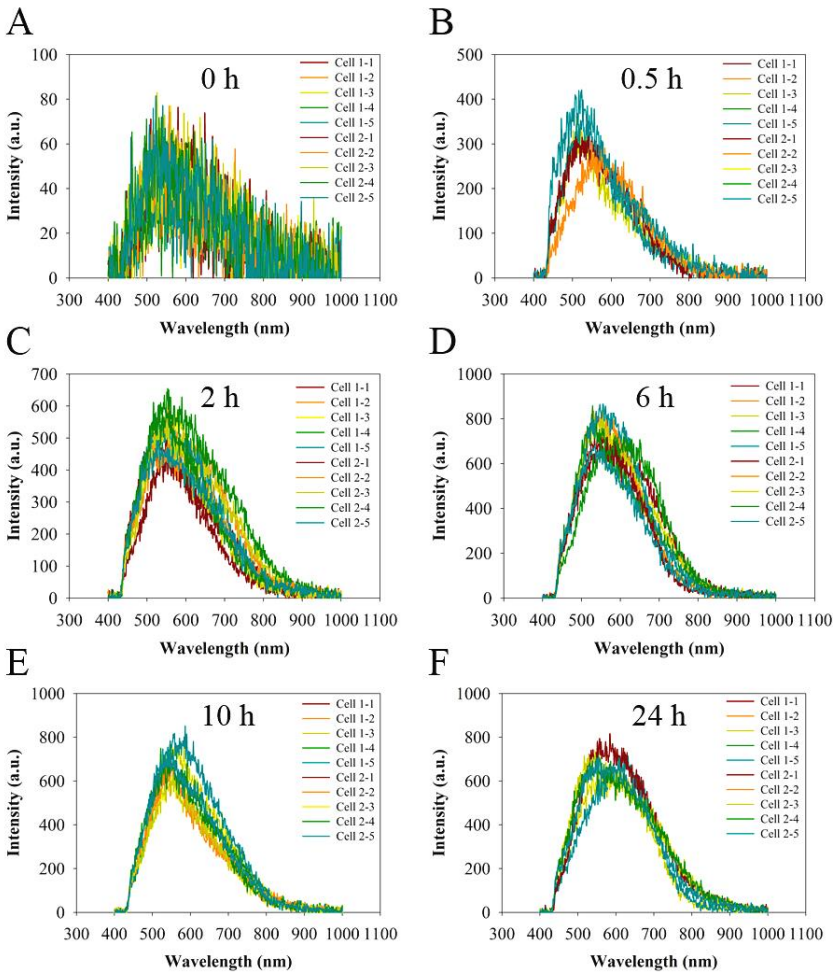

Figure 5.3. Time Dependent Light Signal Measurement. Light intensity measurements of cells without CNDs (A) or with 750 μg/mL of CNDs for different incubation times from 0.5 h to 24 h (B-F).

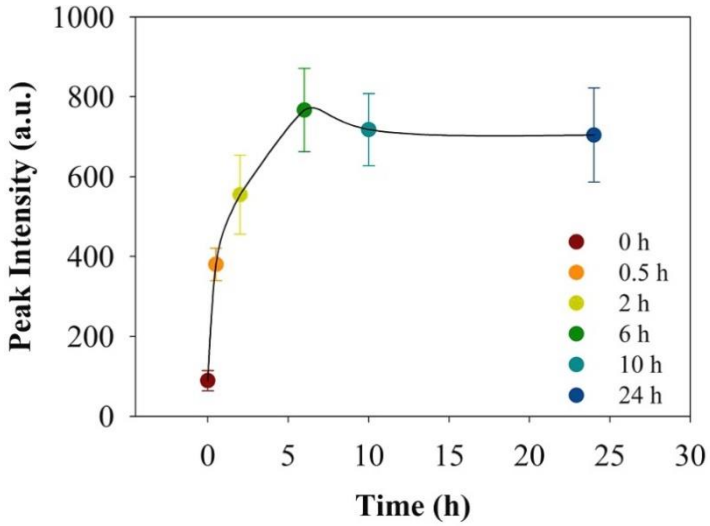

Figure 5.4. Time Dependent Data Analysis. Nuclear penetrability of CNDs.

Light intensity measurements under CNDs incubation with different concentrations: To investigate the effect of CNDs' concentration on their penetration into the nucleus, the cells were incubated under an incubation time of 24 h with different CNDs concentrations. With the background image (Figure 5.5A) without CNDs treated in the same way. Bright colors were used to characterize the nucleus' structure and presence of CNDs (Figure 5.5B-F). At a low CNDs concentration at 75 μg/mL, weak light signals form in the boundary region of the nucleus close to the cytoplasm (Figure 5.5B). As the CNDs concentration increases, the light signals become stronger at the center of the cells and again uniformly distribute in the cells (Figure 5.5C-F). Beyond 1200 μg/mL, the dark field images clearly show white signals corresponding to the incubated CNDs and without significant changes compared to that for 750 μg/mL.

The quantitative determination of the light signals (10 points in two cells) in the nucleus was also performed by measuring the hyperspectral signal via the ENVI software (Figure 5.5) as shown in Figure 5.6. The light intensity also shows a monotonic increase with the increase of the incubation concentration (Figure 5.6A-F). In the range of CNDs concentration of 0-225 μg/mL, the light intensity is slightly increased by about 65 a.u. After incubation concentration of 450 μg/mL, CNDs penetration shows an obvious increase in light intensity. Meanwhile, a feature is also observed that CNDs penetration does not show obvious increase beyond 750 μg/mL incubation concentration.

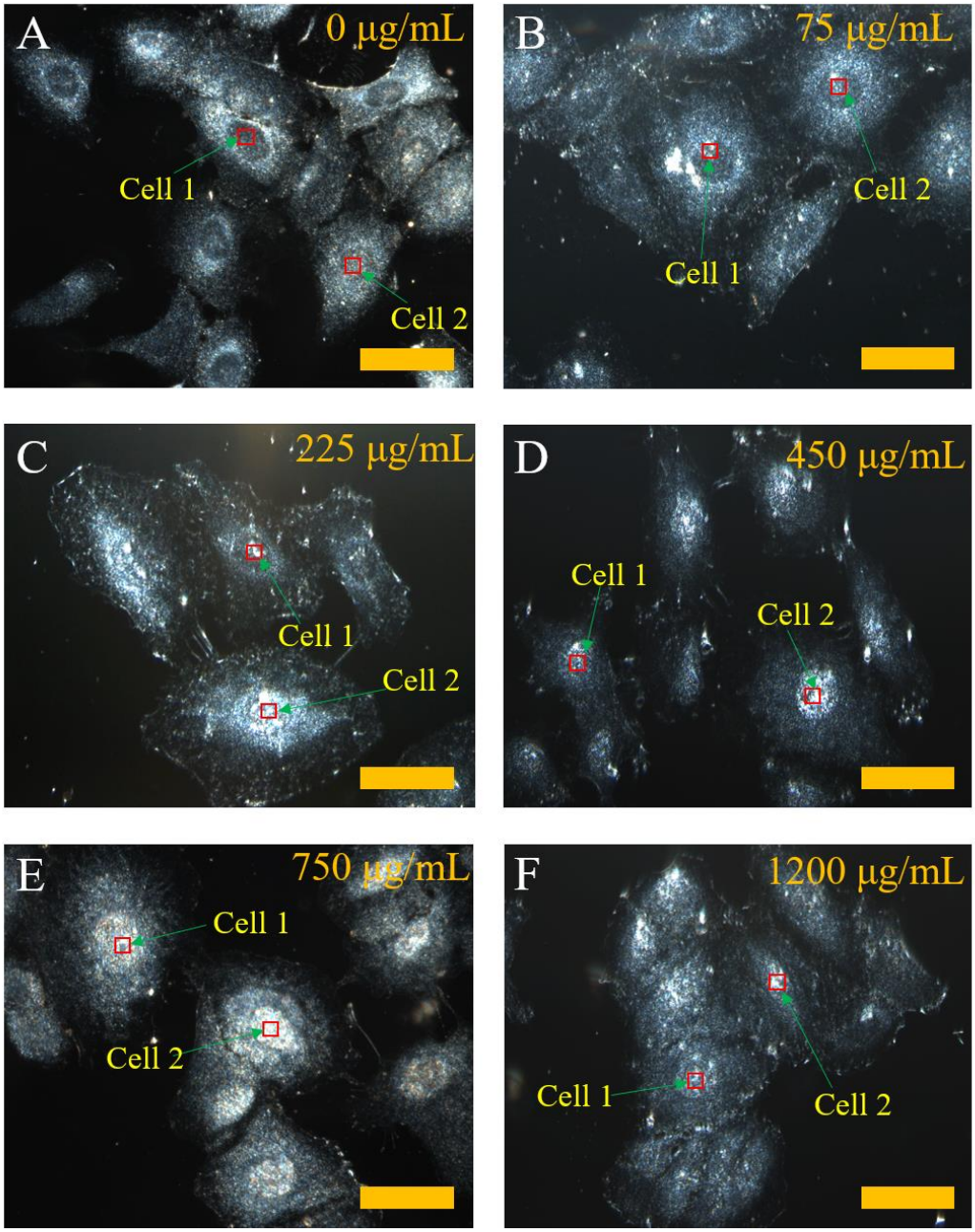

Figure 5.5. Concentration Dependent Dark Field Images. Dark-field images of cells incubated without CNDs (A) or with CNDs for 24 h using different concentrations from 75 µg/mL to 1200 µg/mL (B-F). All of the scale bars are 4 µm.

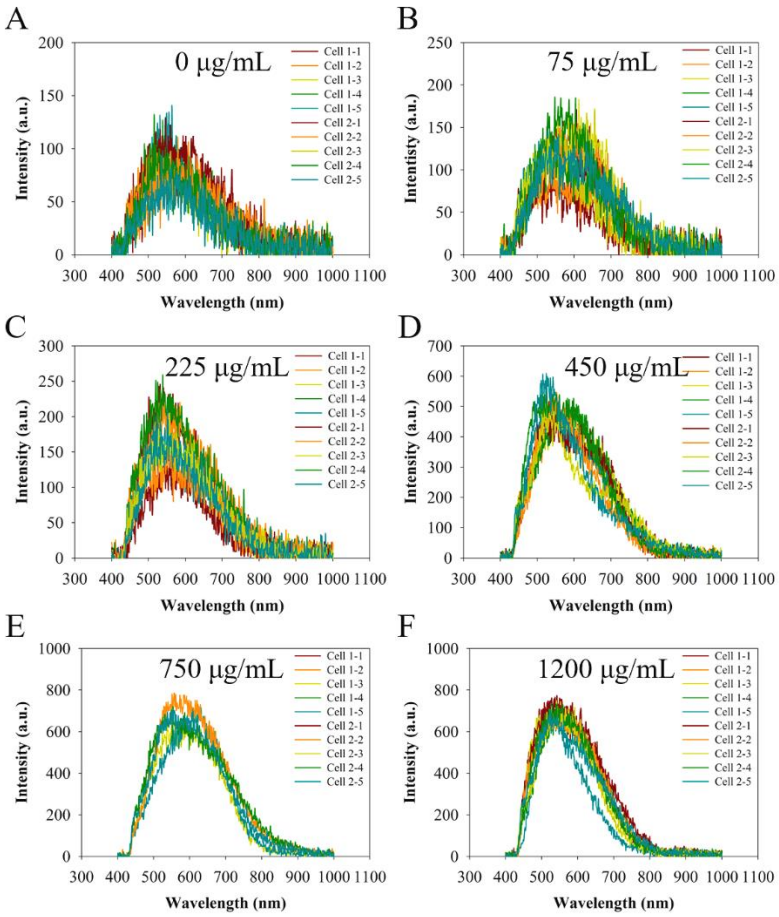

Figure 5.6. Concentration Dependent Light Signal Measurement. Light intensity measurements of cells incubated without CNDs (A) or with CNDs for 24 h using different concentrations from 75 μg/mL to 1200 μg/mL (B-F).

The penetration of CNDs into the cells involves the synergistic effects of CNDs direct diffusion across the plasma membrane, receptor mediated or fluid phase endocytosis, and going through the channels in the plasma membrane, followed by CNDs nuclear penetration though the large proteinaceous assembly (NPC) (Figure 5.7). The nuclear membrane embeds the NPCs, resulting in selective channels for the transport of molecules and mediation of nucleocytoplasmic exchange.[38-39] The NPC, with 125 million

Dalton, 50- 70 nm in thickness, and 100- 150 nm in diameter, has an octagonal symmetry.[40] To across the NPC, although the nuclear localization sequences (specific amino acid sequences) are required for the transport of macromolecules and an active transport process is required for large nanoparticles (> 39 nm) entering into the nucleus associated with importins, no regulation is needed for the smaller nanoparticles (< 9 nm) entering into the nucleus.[41] Moreover, the pore gate for the transport of CNDs can open up to about 30 nm, serving as a dynamic structure.[42] In this case, under the same incubation time, the concentration-dependent nuclear penetration analysis suggests a three-stage mechanism. The first stage involves CNDs penetration on the nuclear side boundary layer of the NPC (0-160 μg/mL of CNDs incubation). The second step involves association with importins to transport the aggregated CNDs with larger sizes and then comprehensively distribute in the nucleus due to the presence of dissociation between the aggregated CNDs and importins originating from the conformation change in the importins (160-750 μg/mL CNDs incubation)[43] The third stage involves the cessation of CNDs penetration into the nucleus even increasing CNDs concentrations (>750 μg/mL of CNDs incubation).

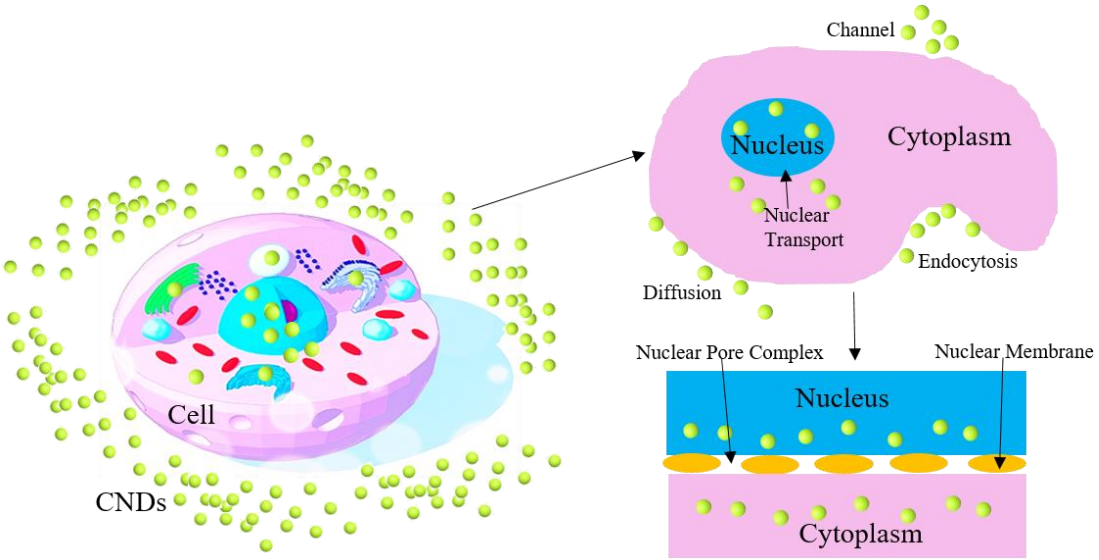

Figure 5.7 Mechanistic View of the Nuclear Penetrability of CNDs.

Conforming to the experimental results, the nuclear penetration of CNDs can be controlled by the incubation concentration (Figure 5.8). Herein, we build a model to describe the relationship between the light intensity and incubation CNDs concentration as the following equations. Note that all of the equations are dimensionless, since we correlate the light signals with the number of CNDs.

$$dI/dt = \alpha\left(C - C_s\right) \tag{1}$$

where *dI/dt* is the rate of nuclear penetration of CNDs, α is the assumed penetration flux, C is the incubation concentration, and C_s is the saturation CNDs concentration to balance the inlet and outlet CNDs.[16] A nonlinear exponential relationship with two characteristic constants (β and ε) has been built for the nuclear penetration of CNDs and the radius of the nucleus structure for a single cell (r):[27, 44-45]

$$C = \beta \exp\left(\varepsilon r / I\right) \tag{2}$$

Based on the nonlinear relationship between incubation concentration and light intensity, the saturation of light intensity is thus given by the equation:

$$I_{\max} = \varepsilon r \Big/ \left(\ln\left(C_s / \beta\right)\right) \tag{3}$$

thus, the following equation could be obtained to conduct a best fit of the light intensity versus incubation concentration data:

$$I = I_{\min} + (I_{\max} - I_{\min}) \Big/ (1 + 10^{(C_{0.5} - C)}) \left(C > 0\right) \tag{4}$$

with an I_{min} of about 31 a.u., I_{max} of about 609 a.u. and a halfway incubation concentration ($C_{0.5}$) of about 479 μg/mL. From 75 μg/mL to 1200 μg/mL, the light intensity firstly increases in a concentration-dependent manner (from 75 μg/mL to 750 μg/mL) until the CNDs penetration is observed to plateau after 750 μg/mL of incubation concentration, corresponding to a three-stage mechanism for the nuclear penetration of CNDs.

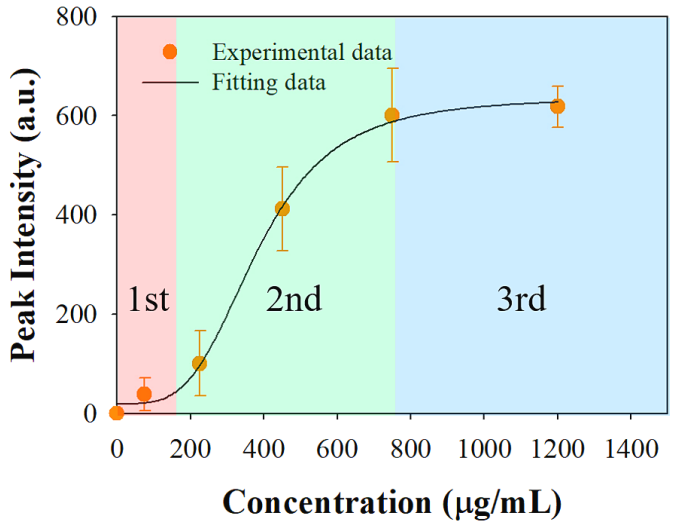

Figure 5.8. Concentration Dependent Modeling. The concentration-dependent data analysis of the nuclear penetrability of CNDs.

Conclusion

This study demonstrates that CNDs can penetrate into the cell and the change in the mechanism of CNDs penetration with respect to the incubation concentration was investigated. In contrast to earlier studies focusing on the fluorescence techniques, this study was conducted with a CytoViva technology to quantitatively determine the light signals in the nucleus. CNDs penetration proceeds with a three-stage concentration-dependency with a halfway incubation concentration of 479 μg/mL. These findings represent a significant contribution in drug delivery carriers, single molecule detection and live cell imaging.

References

1. Zhu, S.; Meng, Q.; Wang, L.; Zhang, J.; Song, Y.; Jin, H.; Zhang, K.; Sun, H.; Wang, H.; Yang, B. Angewandte Chemie International Edition 2013, 52 (14), 3953-3957.

2. Lim, S. Y.; Shen, W.; Gao, Z. Chemical Society Reviews 2015, 44 (1), 362-381.

3. Li, H.; Kang, Z.; Liu, Y.; Lee, S.-T. Journal of Materials Chemistry 2012, 22 (46), 24230-24253.

4. Roy, P.; Chen, P.-C.; Periasamy, A. P.; Chen, Y.-N.; Chang, H.-T. Materials Today 2015, 18 (8), 447-458.

5. Zheng, X. T.; Ananthanarayanan, A.; Luo, K. Q.; Chen, P. Small 2014, 11 (14), 1620-1636.

6. Wang, Y.; Hu, A.. Journal of Materials Chemistry C 2014, 2 (34), 6921-6939.

7. Zeng, Z.; Zhang, W.; Arvapalli, D. M.; Bloom, B.; Sheardy, A.; Mabe, T.; Liu, Y.; Ji, Z.; Chevva, H.; Waldeck, D. H.; Wei, J. Physical Chemistry Chemical Physics 2017, 19 (30), 20101-20109.

8. Wu, Y.-F.; Wu, H.-C.; Kuan, C.-H.; Lin, C.-J.; Wang, L.-W.; Chang, C.-W.; Wang, T.-W. Scientific Reports 2016, 6, 21170.

9. Khan, S.; Verma, N. C.; Chethana; Nandi, C. K. ACS Applied Nano Materials 2018, 1 (2), 483-487.

10. Dekaliuk, M.; Pyrshev, K.; Demchenko, A. Journal of Nanobiotechnology 2015, 13 (1), 86.

11. Yang, C., Neshatian, M., van Prooijen, M., & Chithrani, D. B. Journal of nanoscience and nanotechnology, 2014. 14(7), 4813-4819.

12. Shukla, R.; Bansal, V.; Chaudhary, M.; Basu, A.; Bhonde, R. R.; Sastry, M. Langmuir 2005, 21 (23), 10644-10654.

13. Abadeer, N. S.; Murphy, C. J. The Journal of Physical Chemistry C 2016, 120 (9), 4691-4716.

14. Ma, X.; Hartmann, R.; Jimenez de Aberasturi, D.; Yang, F.; Soenen, S. J. H.; Manshian, B. B.; Franz, J.; Valdeperez, D.; Pelaz, B.; Feliu, N.; Hampp, N.;

Riethmüller, C.; Vieker, H.; Frese, N.; Gölzhäuser, A.; Simonich, M.; Tanguay, R. L.; Liang, X.-J.; Parak, W. J. ACS Nano 2017, 11 (8), 7807-7820.

15. Dimitriou, N. M.; Tsekenis, G.; Balanikas, E. C.; Pavlopoulou, A.; Mitsiogianni, M.; Mantso, T.; Pashos, G.; Boudouvis, A. G.; Lykakis, I. N.; Tsigaridas, G.; Panayiotidis, M. I.; Yannopapas, V.; Georgakilas, A. G. Pharmacology & Therapeutics 2017, 178, 1-17.

16. Gao, Y., Li, M., Chen, B., Shen, Z., Guo, P., Wientjes, M. G., & Au, J. L. S. The AAPS journal, 2013, 15(3), 816-831.

17. Zhang, X. D., Wu, D., Shen, X., Chen, J., Sun, Y. M., Liu, P. X., & Liang, X. J. Biomaterials, 2012, 33(27), 6408-6419.

18. Jia, L., Shen, J., Li, Z., Zhang, D., Zhang, Q., Duan, C., ... & Tian, X. International journal of pharmaceutics, 2012, 439(1-2), 81-91.

19. Yang, C., Uertz, J., Yohan, D., & Chithrani, B. D. Nanoscale, 2014, 6(20), 12026-12033.

20. Jin, H.; Heller, D. A.; Sharma, R.; Strano, M. S. ACS Nano 2009, 3 (1), 149-158.

21. Combs, C. A. Current Protocols in Neuroscience 2010, 50 (1), 2.1.1-2.1.14.

22. Papaioannou, N.; Marinovic, A.; Yoshizawa, N.; Goode, A. E.; Fay, M.; Khlobystov, A.; Titirici, M.-M.; Sapelkin, Scientific Reports 2018, 8 (1), 6559.

23. Lu, S.; Sui, L.; Liu, J.; Zhu, S.; Chen, A.; Jin, M.; Yang, B. Advanced Materials 2017, 29 (15), 1603443.

24. Ong, W.-J.; Putri, L. K.; Tan, Y.-C.; Tan, L.-L.; Li, N.; Ng, Y. H.; Wen, X.; Chai, S.-P. Nano Research 2017, 10 (5), 1673-1696.

25. Elsaesser, A.; Taylor, A.; de Yanés, G. S.; McKerr, G.; Kim, E.-M.; O'Hare, E.; Howard, C. V. Nanomedicine 2010, 5 (9), 1447-1457.

26. Wolfbeis, O. S. Chemical Society Reviews 2015, 44 (14), 4743-4768.

27. Ivask, A.; Mitchell, A. J.; Malysheva, A.; Voelcker, N. H.; Lombi, E. Wiley Interdisciplinary Reviews: Nanomedicine and Nanobiotechnology 2017, 10 (3), e1486.

28. Hu, Q.; Paau, M. C.; Zhang, Y.; Chan, W.; Gong, X.; Zhang, L.; Choi, M. M. F. Journal of Chromatography A 2013, 1304, 234-240.

29. Essner, J. B.; Kist, J. A.; Polo-Parada, L.; Baker, G. A. Chemistry of Materials 2018, 30 (6), 1878-1887.

30. Zhang, W.; Zeng, Z.; Wei, J. The Journal of Physical Chemistry C 2017, 121 (34), 18635-18642.

31. Li, W.; Zhang, Z.; Kong, B.; Feng, S.; Wang, J.; Wang, L.; Yang, J.; Zhang, F.; Wu, P.; Zhao, D. Angewandte Chemie International Edition 2013, 52 (31), 8151-8155.

32. Wang, Y., Kalytchuk, S., Zhang, Y., Shi, H., Kershaw, S. V., & Rogach, A. L. (2014). Thickness-dependent full-color emission tunability in a flexible carbon dot ionogel. The journal of physical chemistry letters, 5(8), 1412-1420.

33. Zhu, S.; Song, Y.; Zhao, X.; Shao, J.; Zhang, J.; Yang, B. Nano Research 2015, 8 (2), 355-381.

34. Oh, E. S., Heo, C., Kim, J. S., Suh, M., Lee, Y. H., & Kim, J. M. Journal of biomedical optics, 2013, 19(5), 051207.

35. Puri, V.; Watanabe, R.; Singh, R. D.; Dominguez, M.; Brown, J. C.; Wheatley, C. L.; Marks, D. L.; Pagano, R. E. The Journal of Cell Biology 2001, 154 (3), 535.

36. Zhou, N.; Zhu, S.; Maharjan, S.; Hao, Z.; Song, Y.; Zhao, X.; Jiang, Y.; Yang, B.; Lu, L. RSC Advances 2014, 4 (107), 62086-62095.

37. Mao, Q.-X.; E, S.; Xia, J.-M.; Song, R.-S.; Shu, Y.; Chen, X.-W.; Wang, J.-H. Langmuir 2016, 32 (46), 12221-12229.

38. Fernandez-Martinez, J.; Rout, M. Nuclear pore complex biogenesis. Curr Opin Cell Biol, 2009; Vol. 21, p 603-12.

39. Suntharalingam, M.; Wente, S. R. Developmental Cell 2003, 4 (6), 775-789.

40. Wente, S. R.; Rout, M. P. Cold Spring Harbor Perspectives in Biology 2010, 2 (10).

41. Yang, C.; Uertz, J.; Yohan, D.; Chithrani, B. D. Nanoscale 2014, 6 (20), 12026-12033,

42. Pavelka, M., & Roth, J. Functional ultrastructure: atlas of tissue biology and pathology. Springer. 2015.

43. Görlich, D. Nuclear protein import, 1997; Vol. 9, p 412-9.

44. Belli, V.; Guarnieri, D.; Biondi, M.; della Sala, F.; Netti, P. A. Colloids and Surfaces B: Biointerfaces 2017, 149, 7-15.

45. Goodman, T. T.; Chen, J.; Matveev, K.; Pun, S. H. Biotechnology and bioengineering 2008, 101 (2), 388-39

CHAPTER VI

CONCLUSIONS

Chapter 2 demonstrates a novel fluorescence spectroelectrochemistry approach that applied to investigate the real time effect of chemically reversible redox couple on the optoelectronic properties of microwave synthesized CNDs. The photocurrent generation from CNDs immobilized on the gold slide was also investigated at different excitation wavelengths from fluorescence spectrophotometer upon varied applied bias voltage by this fluorescence spectroelectrochemical study, indicating wavelength dependence on photocurrent generation from the CNDs as electron donors to the gold electrode. The optical band gap of CNDs calculated by the UV-Vis absorbance spectrum is in accord with HOMO-LUMO energy gap obtained by the electrochemical measurement. We also used a theoretical Hückel model to get molecular-like structure of CNDs and then we fitted the structure to match the HOMO-LUMO energy gap obtained by the experimental measurements. Based on the experimental and theoretical analysis of energy gap and the fluorescence based spectroelectrochemical study, the excitation dependent photoluminescence property of CNDs is ascribed to multifactor combination such as the core C=C, surface functionalities (C=O, C-O, and COOH), and/or surface electronic state transitions. This study representes a new perspective of optoelectronic properties of CNDs which may pave the way to their development in bioimaging and optoelectronic devices.

In Chapter 3, a new strategy was demonstrated to explore the antioxidation property of one type of microwave synthesized CNDs(U-dots) based on the reserved DPPH• concentration and standard heterogeneous electron-transfer rate constant changes in the DPPH•-gold electrode system at different U-dots incubated concentration. The relationship between reserved DPPH• concentration and U-dots incubated concentration was established by the electrochemical measurement which is consistent with UV-Vis absorbance concentration-dependent results, suggesting CNDs antioxidation process may rely on a hydrogen atom transfer (HAT) mechanism. This study opens a new avenue to investigate the antioxidation property of CNDs and should aid their development in nanomedicine.

In Chapter 4, three different methods including UV-Vis absorbance of DPPH•, electrochemical test on DPPH• and lucigenin derived chemiluminescence enzymatic assay are utilized to investigate the antioxidation capacity of a N, S co-doped CNDs. The electrochemical measurements are in reasonably agreement with UV-Vis absorbance results, which indicated the redox reaction undergoes by a HAT mechanism. Meanwhile, the xanthine /XO system induced lucigenin- CL quenching by different concentrations of N, S co-doped CNDs was attributed to the ROS scavenging property of N, S co-doped CNDs. In combination with biocompatibility and bioimaging properties study, these results indicate that a novel nanoparticle based medical treatment for ROS induced inflammatory disease such as atherosclerosis.

Chapter 5 presented the CNDs cell nucleus penetration process upon different incubation time and incubated CNDs concentration. In this study, a dark field microscopy

combined with hyperspectral technique was adopted to investigate the interaction between CNDs and cell nucleus versus traditional fluorescence microscopy. The cell nucleus penetration behaviour was studied quantitively by examining the reflected light signal of CNDs inside the cells via hyperspectral technique. CNDs penetration process shows a three-stage concentration dependent manner with a halfway incubation concentration of 2.68 mg/mL. This finding should facilitate the potential applications of CNDs in biomedicine (drug delivery and live cell imaging) and single molecule detection.

APPENDIX A

A FLUORESCENCE-ELECTROCHEMICAL STUDY OF CNDS

Characterization of AFM Image and profile:

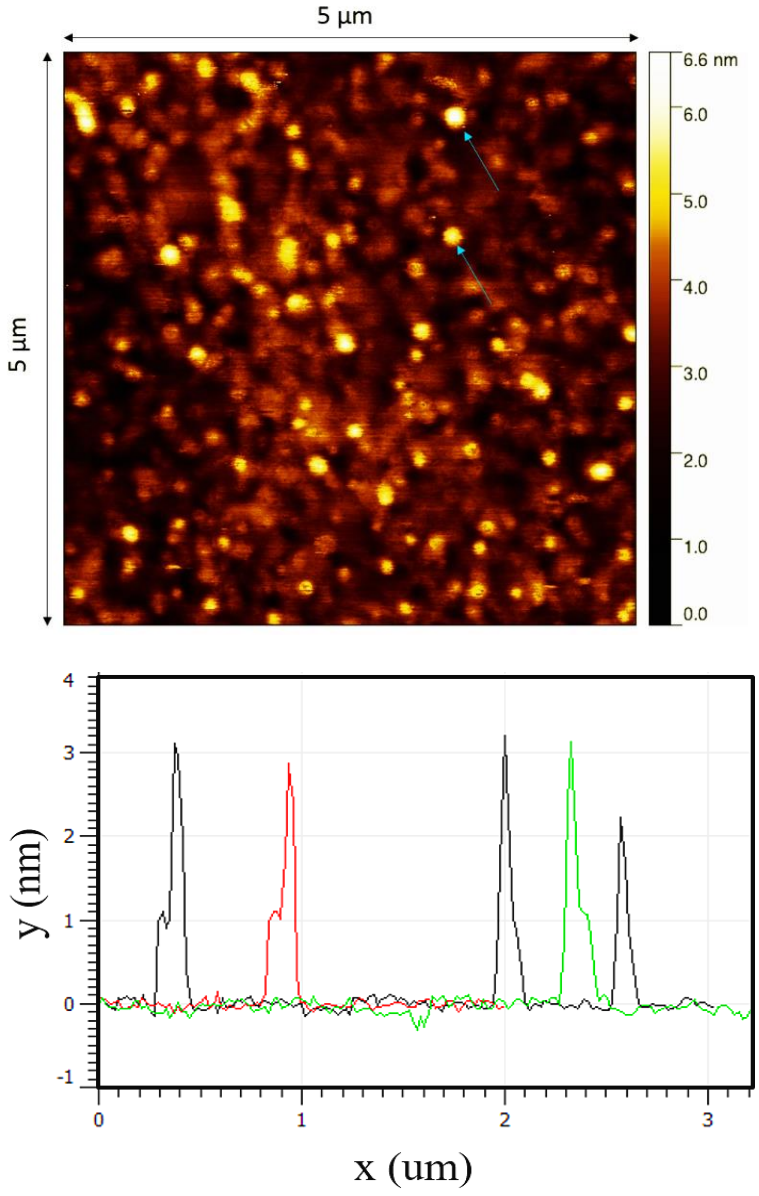

Figure S 2.1. AFM Image and Cross Section Profile.

XPS:

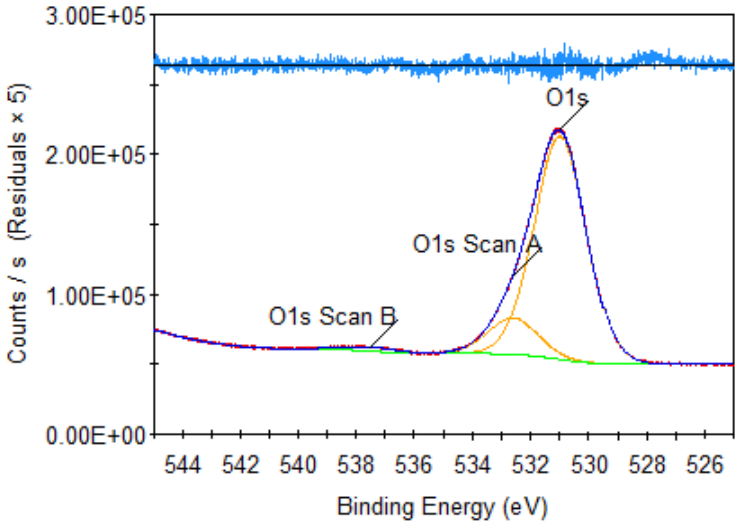

Figure S 2.2. High Resolution O XPS Spectrum and Its Simulated Peak Fit.

Table S 2.1. High Resolution O XPS Spectrum Analysis

Name	Start BE	Peak BE	End BE	Height CPS	FWHM eV	Area (P) CPS.eV	Area (N) TPP-2M	Atomic %
O1s	544.99	530.95	525.01	159349.07	2.07	357909.21	0.86	84.81
O1s Scan A	544.99	532.59	525.01	26334.66	2.01	57238.62	0.14	13.57
O1s Scan B	544.99	537.53	525.01	3017.5	2.08	6788	0.02	1.61

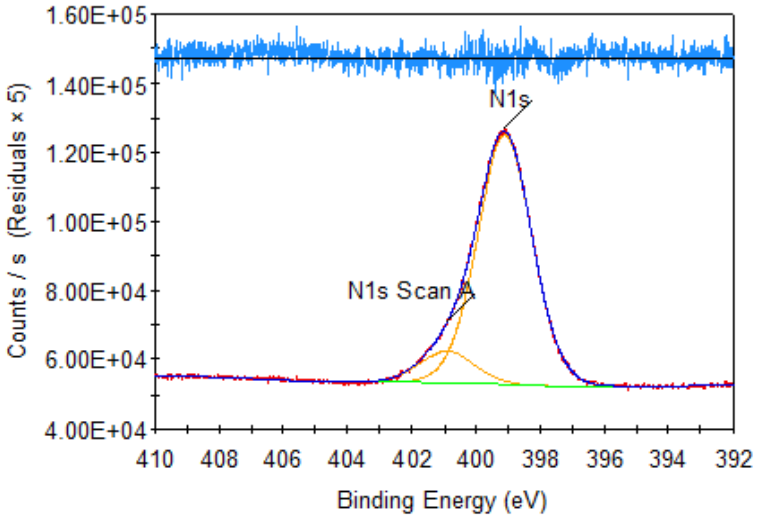

Figure S 2.3. High Resolution N XPS Spectrum and Its Simulated Peak Fit.

Table S 2.2. High Resolution N XPS Spectrum Analysis

Name	Start BE	Peak BE	End BE	Height CPS	FWHM eV	Area (P) CPS.eV	Area (N) TPP-2M	Atomic %
N1s	409.99	399.11	392.01	72523.1	1.98	155646.87	0.61	88.8
N1s Scan A	409.99	400.9	392.01	9222.81	1.96	19610.83	0.08	11.2

Table S 2.3. Survey XPS Spectrum Analysis

Name	Start BE	Peak BE	End BE	Height CPS	FWHM eV	Area (P) CPS.eV	Area (N) TPP-2M	Atomic %
O1s	541.5	531.65	523	315606.48	3.92	1336206.35	0.85	27.1116
N1s	406	399.8	394.5	133751.39	3.68	527094.38	0.53	17.0188
C1s	293	286.14	278	184033.28	5.79	1065537.72	1.7	54.3737

Zeta potential:

Table S 2.4. Zeta Potential Measurement of CNDs

pH	Dispersion name	Dispersion refractive index	Temperature	Zeta runs	Zeta Potential
5.86	Water	1.330	25 ˚C	12	-22.3 mV

Quantum yield:

Table S 2.5. Quantum Yield Measurement of CNDs

Sample	Refractive index(η)	Quantum yield(Q)
Quinine sulfate	1.33	0.54
CNDs	1.33	0.085

Quinine sulfate (quantum yield 0.54 at 360 nm) dissolved in 0.1 M H_2SO_4 (refractive index(η_R) =1.33) was chosen as reference. As-prepared CNDs were dispersed in deionized water (η_x=1.33). All samples were tested to obtain absorption intensities by UV-Vis spectrometer (Varian Cary 6000i). In order to minimize re-absorption effects, the UV-Vis absorbance was kept under 0.1 OD, and the photoluminescence (PL) was measured at an excitation wavelength of 360 nm (Varian Cary Eclipse). The quantum yield was calculated based on the following equation:

$$Q_x = Q_R \times \frac{I_x}{I_R} \times \frac{A_R}{A_x} \times \frac{\eta_x^2}{\eta_R^2} \quad \text{(S1)}$$

where Q is quantum yield, *I* is integrated PL intensity of the sample, A is the absorbance intensity, η is the refractive index for the solvent, X means as-prepared CNDs, and R refers to quinine sulfate as reference fluorophore.

Bioimaging:

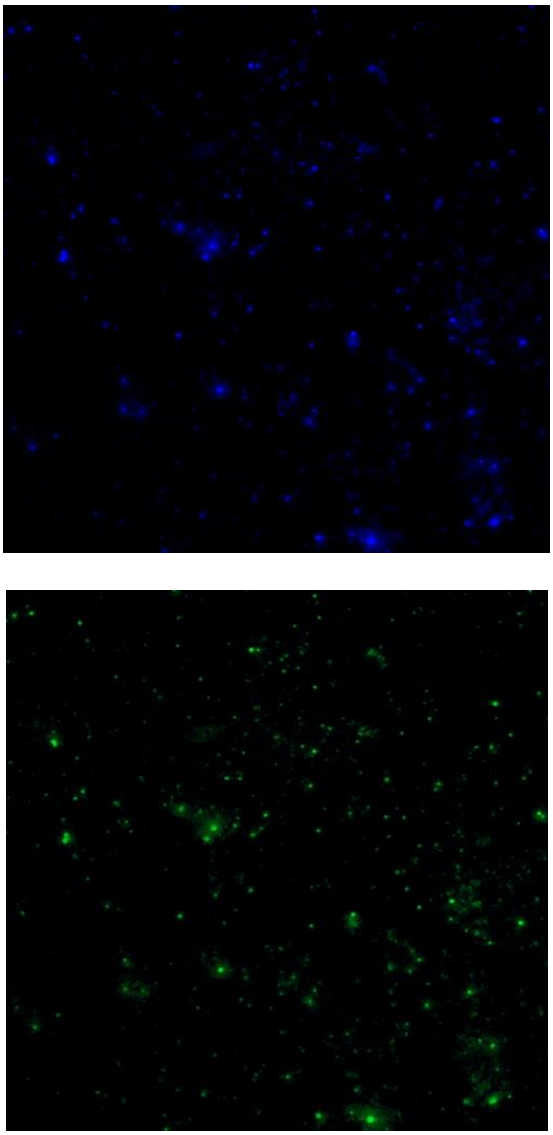

Figure S 2.4. Confocal Images of HepG2 Cells. Cells culture treated with CNDs (0.3 mg/mL) for 72 hours.

Electrochemistry causes fluorescence of CNDs to change

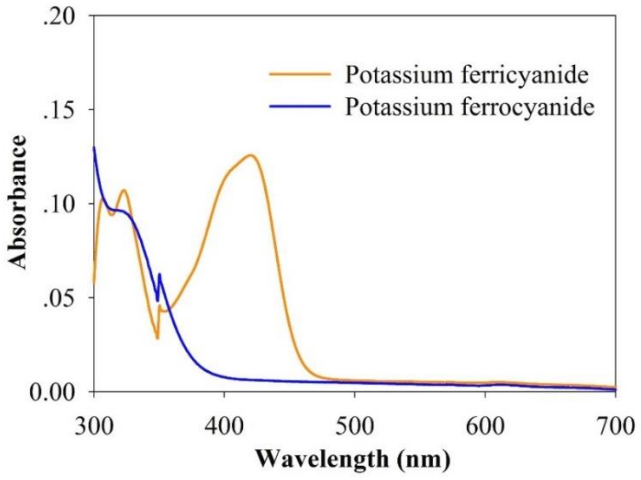

Figure S 2.5. UV-Vis Absorption Spectrum of CNDs. Potassium ferricyanide and potassium ferrocyanide.

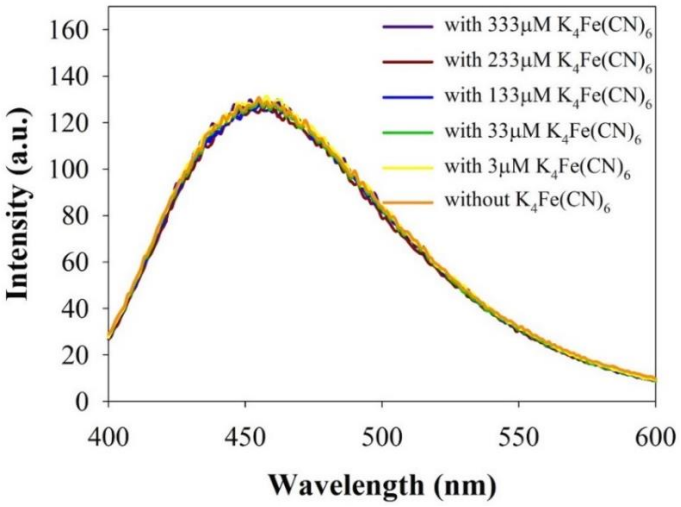

Figure S 2.6. Fluorescence Spectrum. Fluorescence spectrum of solution including 50 μg/mL CNDs and 0.1 M KCl after addition of $K_4Fe(CN)_6$ with different concentrations (3, 33, 133, 233, and 333 μM).

Light from the fluorescence spectrophotometer causes CNDs to generate photocurrent

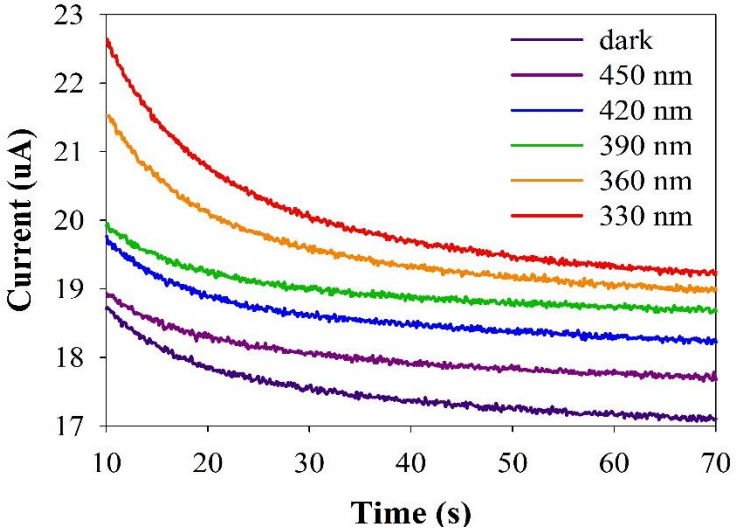

Figure S 2.7. Chronoamperometry (CA). CA measurements with an applied voltage of 0.8 V of the gold slide electrode with CNDs immobilization before and after light irradiation with different incident wavelength (330-450 nm).

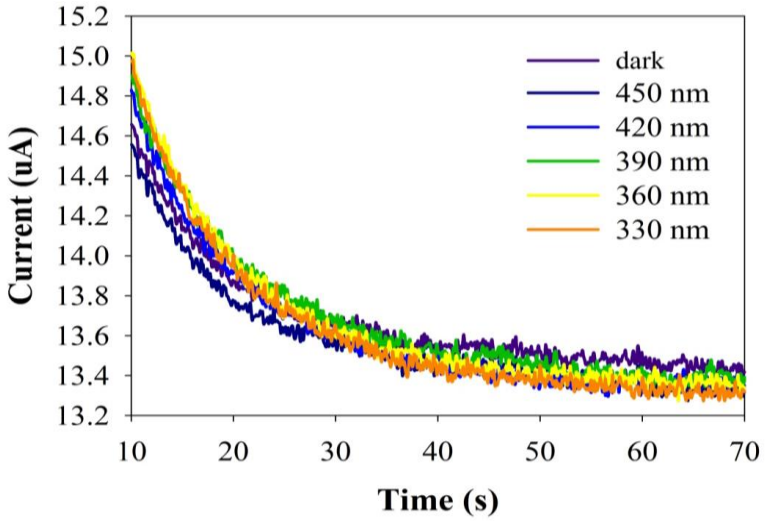

(a)

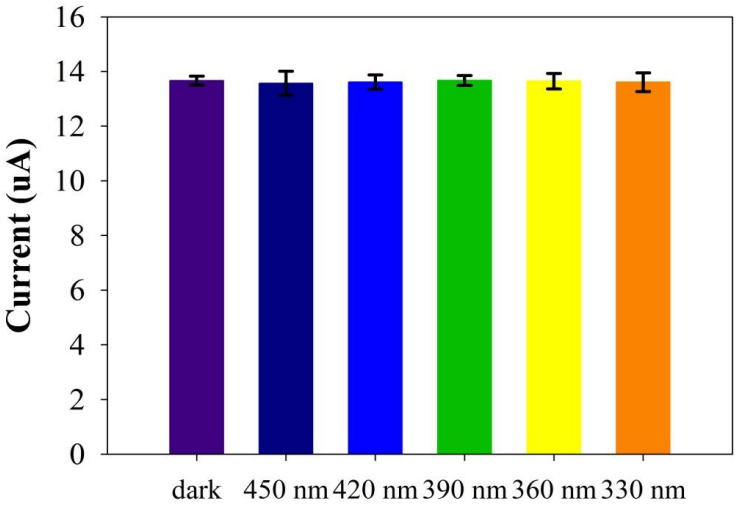

(b)

Figure S 2.8. Chronoamperometry (CA). CA measurements with an applied voltage of 0.8 V of the gold slide electrode without CNDs immobilization before and after light irradiation with different incident wavelength (330-450 nm).

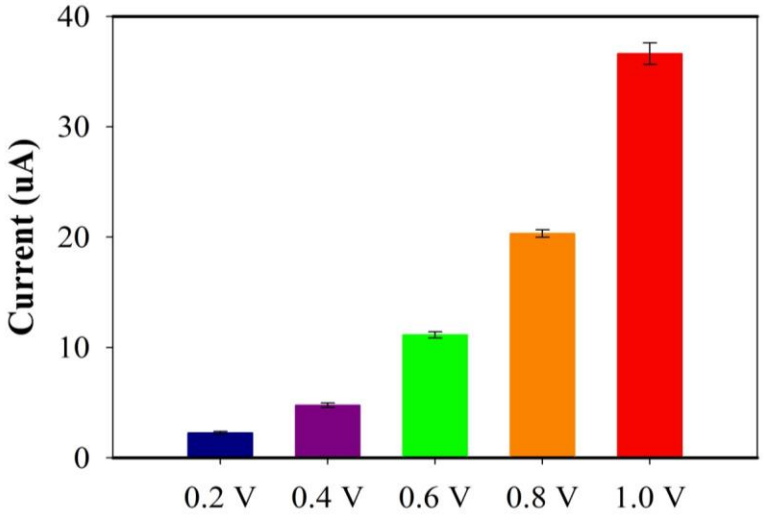

Figure S 2.9. CA Measurement. CA measurement with different applied potentials of the gold slide electrode with CNDs immobization under incident wavelength of 330 nm.

Band energy and molecular orbital energy level

Method 1. Optical band gap and exciton binding energy calculation

The indirect band gap formula in the semiconductor system could be used as:

$$\alpha h\nu = C(h\nu - E_o)^2 \quad \text{(S2)}$$

where α is the absorption coefficient, h is the Plank constant, ν is the frequency, C is the coefficient, and E_o is the optical band gap, $(\alpha h\nu)^{1/2}$ has a linear relationship with hν, which could be used to estimate E_o. The Beer-Lambert law states that

$$A = \alpha bc, \quad \text{(S3)}$$

where A is the measured absorbance, b is the path length, and c is the analyte concentration. Among them, b and c are fixed values, so the E_o could be calculated as the following equation:

$$(Ahν/bc)^{1/2}=D(hν-E_o), \quad \text{(S4)}$$

where $(Ahν/bc)^{1/2}$ has a linear relationship with hν with a slope of D and E_o is the x-intercept. Note that hν is equal to 1240/λ in units of eV. In addition, changing the path length and concentration did not affect the result of x-intercept (E_o). With the UV-Vis absorption spectrum results, the relationship $(Ahν)^{1/2}$ vs. hν could be used to estimate E_o as 2.13 eV.

Moreover, the exciton binding energy (E_b) can be estimated by the hydrogenic model:

$$E_b = \mu R_H / m_0 \varepsilon^2, \quad \text{(S5)}$$

where μ is the effective reduced mass of the exciton, R_H is the Rydberg constant of the hydrogen atom (13.6 eV), m_0 is the free electron mass, and ε is the dielectric constant. With the assumption of $\mu=0.1\ m_0$, depending on the value used for ε, estimated values for E_b range from 6.1 meV to 13.6 meV.

Method 2. Electrochemical measurement energy gap calculation

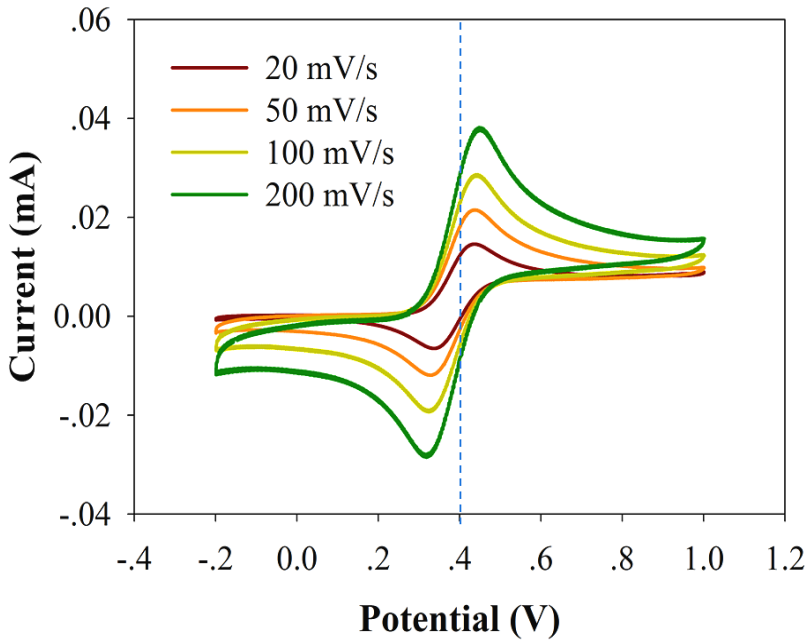

Figure S 2.10. Cyclic Voltammetry (CV). CV of 1mg/mL ferrocene at scan rates of 20, 50, 100, 200 mV/s. CV was recorded in 5 mL acetonitrile containing 0.1M tetrabutylammonium hexafluorophosphate as the supporting electrolyte with a working gold electrode, a reference silver (Ag/AgCl) electrode and a counter platinum electrode. According to the figure, the formal potential of the Fc^{+}/Fc redox couple should be approximately 0.40V versus Ag/AgCl.

Cyclic voltammetry (CV) was used to determine the HOMO and LUMO energy levels of the CNDs. A three-electrode cell with a gold working electrode, a silver reference (Ag/AgCl) electrode and a platinum counter electrode in 4 mL acetonitrile containing 0.1 M tetrabutylammonium hexafluorophosphate as the supporting electrolyte and 1 mL H_2O containing 0.3 mg CNDs as the sample at a scan rate of 100 mV/s under room temperature was used. All the potentials were compared with a standard fc^{+}/fc couple measured in the same solution. Since the potential of SCE is 44 mV more positive

than the potential of Ag/AgCl, and the formal potential of the Fc^+/Fc redox couple should be approximately -5.1 eV in the Fermi scale when its value is 0.40 V versus SCE in acetonitrile, the formal potential of the Fc^+/Fc redox couple could be estimated as -5.06 eV in the Fermi scale when the formal potential of the Fc^+/Fc redox is 0.40 V versus Ag/AgCl.

The HOMO and LUMO energy levels as well as the electrochemical energy gap in eV of the sample could be calculated according to the following equation:

$$E_{HOMO}=-(E_{onset,ox}-0.4+5.06)eV=-(E_{onset,ox}+4.66)eV, \quad (S6)$$

$$E_{LUMO}=-(E_{onset,red}-0.4+5.06)eV=-(E_{onset,red}+4.66)eV, \quad (S7)$$

$$E_{gap}= (E_{onset,ox}-E_{onset,red})eV, \quad (S8)$$

where $E_{onset,ox}$ and $E_{onset,red}$ are the onset of oxidation and reduction potential, respectively.

By applying tangent method, on the basis of the onset of oxidation and reduction potential as 1.18 and -0.91 V, the energy levels of the HOMO and LUMO were estimated to be–5.84 and -3.75 eV, respectively. Moreover, the electrochemical band gap was estimated to be 2.09 eV, which is consistent with the optical band gap.

Method 3. Hückel method energy gap calculation

The Hückel method is a linear combination of atomic orbitals molecular orbitals method for the determination of energies of molecular orbitals in conjugated hydrocarbon systems. Then it could be extended to heteroatoms by adjusting the coulomb and

resonance integral values. Note that the coulomb integral for an electron on a carbon was defined as α and the resonance integral for two bonded carbons in conjugation was defined as β. In our CQDs system, according to the equations (α'=α+hβ, and β'=kβ) and table S6, α and β were adjusted to α' and β'.

Table S 2.6. Adjustment of the Coulomb and Resonance Integral Values

Heteroatom	h	Heteroatom Bond	k	Bond Lengths (Å)
C	0	C-C	0.9	1.54
N	1.5	C=C	1.1	1.35
O	2.0	C-O	0.8	1.43
		C=O	1.0	1.22
		C-N	0.8	1.47

Then by solving the following determinant, the Hückel values for our CNDs can be determined following the order of heteroatoms and heteroatom bonds as the assumed molecular structure of CNDs shown (Fig. S 2.11). After that, we can use $E_i = \alpha' + x_i\beta'$ to calculate L+1, L+2, LUMO, HOMO, H-1, and H-2 energy levels. And the magnitudes of the transition moment for different bonds were calculated. Note that many computer programs like SHMO or Matlab software can help to solve the determinants.

$$
\begin{vmatrix}
\alpha_1'-E & \beta_{1,2}' & \beta_{1,3}' & \beta_{1,4}' & \cdots\cdots & \beta_{1,n-2}' & \beta_{1,n-1}' & \beta_{1,n}' \\
\beta_{2,1}' & \alpha_2'-E & \beta_{2,3}' & \beta_{2,4}' & \cdots\cdots & \beta_{2,n-2}' & \beta_{2,n-1}' & \beta_{2,n}' \\
\beta_{3,1}' & \beta_{3,2}' & \alpha_3'-E & \beta_{3,4}' & \cdots\cdots & \beta_{3,n-2}' & \beta_{3,n-1}' & \beta_{3,n}' \\
\beta_{4,1}' & \beta_{4,2}' & \beta_{4,3}' & \alpha_4'-E & \cdots\cdots & \beta_{4,n-2}' & \beta_{4,n-1}' & \beta_{4,n}' \\
\cdots\cdots & & & & & & & \\
\beta_{n-2,1}' & \beta_{n-2,2}' & \beta_{n-2,3}' & \beta_{n-2,4}' & \cdots\cdots & \alpha_{n-2}'-E & \beta_{n-2,n-1}' & \beta_{n-2,n}' \\
\beta_{n-1,1}' & \beta_{n-1,2}' & \beta_{n-1,3}' & \beta_{n-1,4}' & \cdots\cdots & \beta_{n-1,n-2}' & \alpha_{n-1}'-E & \beta_{n-1,n}' \\
\beta_{n,1}' & \beta_{n,2}' & \beta_{n,3}' & \beta_{n,4}' & \cdots\cdots & \beta_{n,n-2}' & \beta n,_{n-1}' & \alpha_n'-E
\end{vmatrix} = 0
$$

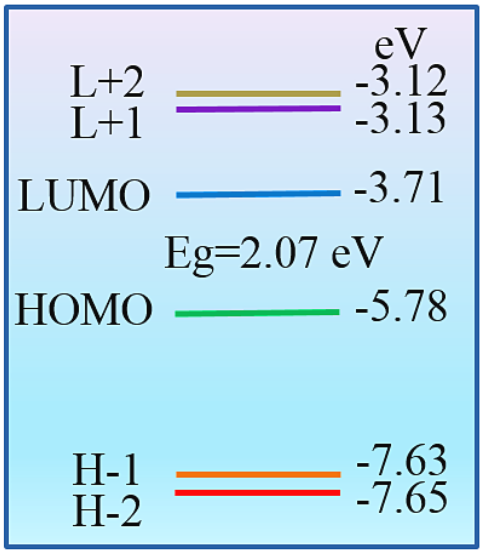

Figure S 2.11. Molecular Orbital Energy Levels. Molecular orbital energy levels of CNDs calculated by Hückel method.

Table S 2.7. Transition Moments for Different Bonds

Bond	Bond Lengths (Å)	Transition Moment (D)
C=C	1.35	3.24
C=O	1.22	2.93
C-O	1.43	3.43
O-H	0.96	2.30

APPENDIX B

AN ELECTROCHEMICAL STUDY OF CNDS ANTIOXIDATION

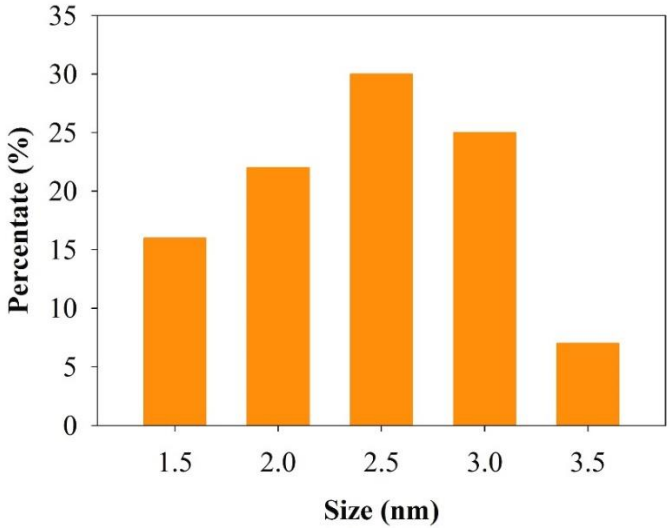

Figure S 3.1. TEM Size Distribution.

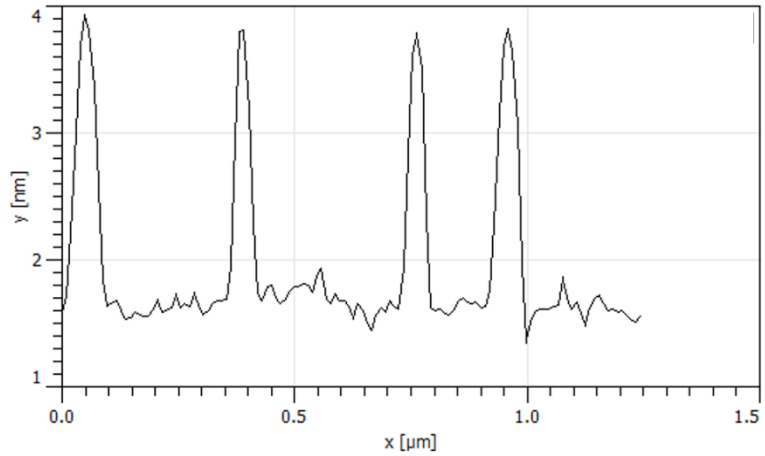

Figure S 3.2. AFM Cross Section Profile.

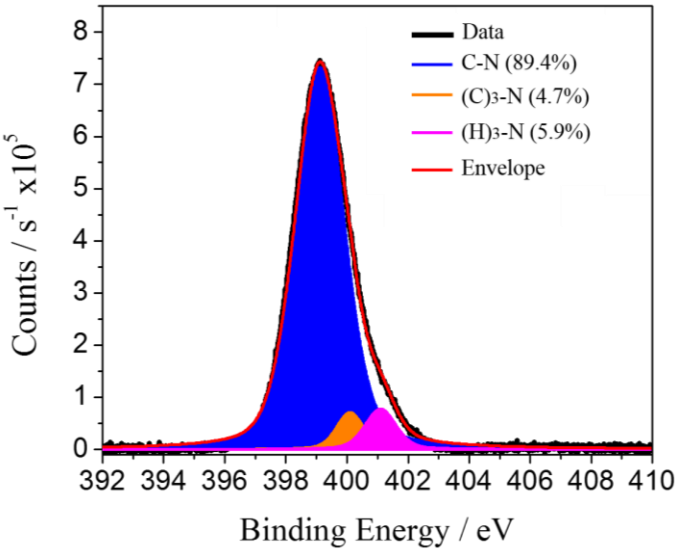

Figure S 3.3. X-Ray Photoelectron Spectrum of U-Dots (N Signal).

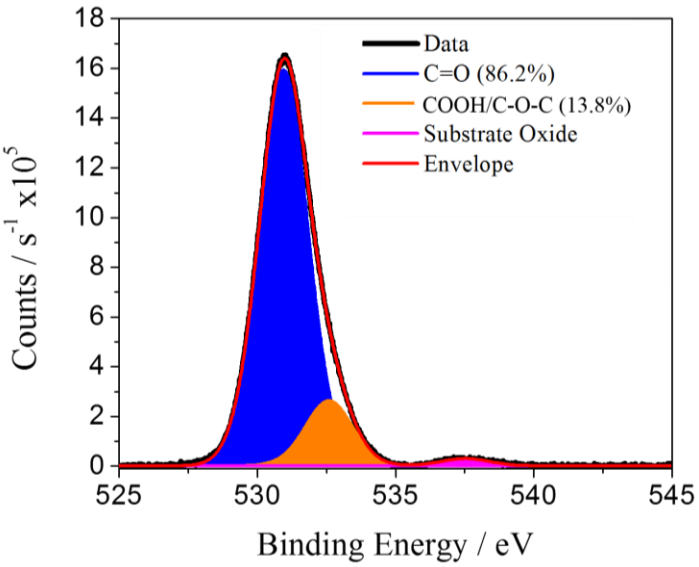

Figure S 3.4. X-Ray Photoelectron Spectrum of U-Dots (O Signal).

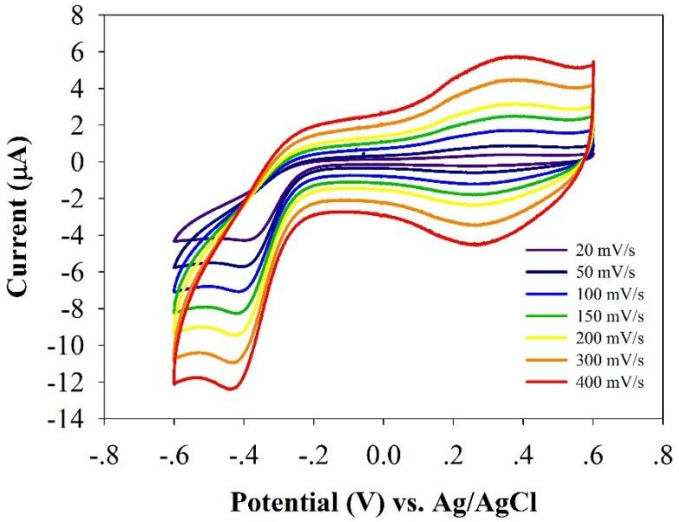

Figure S 3.5. Cyclic Voltammograms. The 0.02 mg/mL of DPPH• in a 5.0 mL methanolic phosphate buffer at scan rates of 20, 50, 100, 150, 200, 300 and 400 mV/s without U-dots incubation.

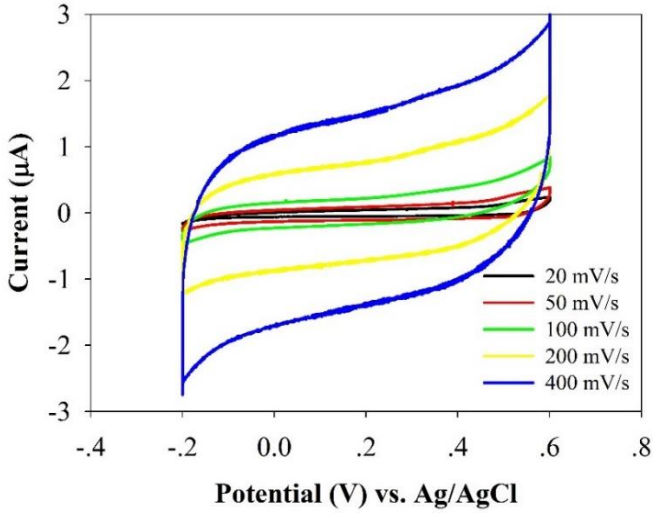

Figure S 3.6. Cyclic Voltammograms. The 0.05 mg/mL of U-dots in a 5.0 mL methanolic phosphate buffer at scan rates of 20, 50, 100, 200 and 400 mV/s (as a control without DPPH•).

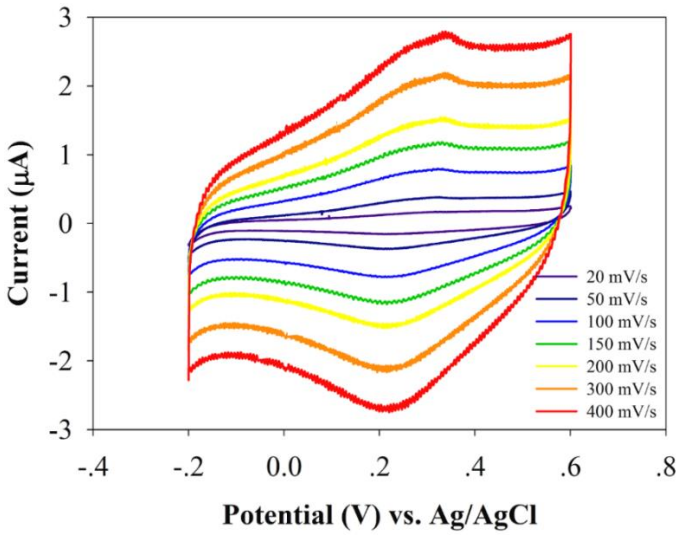

Figure S 3.7. Cyclic Voltammograms. The 0.01 mg/mL of DPPH• in a 5.0 mL methanolic phosphate buffer at scan rates of 20, 50, 100, 150, 200, 300 and 400 mV/s (as a control without U-dots incubation).

APPENDIX C

ANTIOXIDATION CAPACITY OF NITROGEN, SULFER CO-DOPED CNDS

Table S 4.1. Quantum Yield Measurement of N, S Co-doped CNDs

Sample	Refractive index(η)	Quantum yield(Q)
Quinine sulfate	1.33	0.54
N, S co-doped CNDs	1.33	0.11

Quinine sulfate (quantum yield 0.54 at 360 nm) dissolved in 0.1 M H_2SO_4 (refractive index(η_R) =1.33) was chosen as a reference. As-prepared N, S co-doped CNDs were dispersed in deionized water (η_x=1.33). All samples were tested to obtain absorption intensities by a UV-Vis spectrometer (Varian Cary 6000i). In order to minimize re-absorption effects, the UV-Vis absorbance was kept under 0.1 OD, and the photoluminescence (PL) was measured at an excitation wavelength of 360 nm (Varian Cary Eclipse). The quantum yield was calculated based on the following equation:

$$Q_x = Q_R \times \frac{I_x}{I_R} \times \frac{A_R}{A_x} \times \frac{\eta_x^2}{\eta_R^2} \quad \text{(S1)}$$

where *Q* is the quantum yield, *I* is the integrated PL intensity of the sample, *A* is the absorbance intensity, and η is the refractive index for the solvent. The subscript *X* means as-prepared N, S co-doped CNDs, and the subscript *R* refers to quinine sulfate as a reference fluorophore.

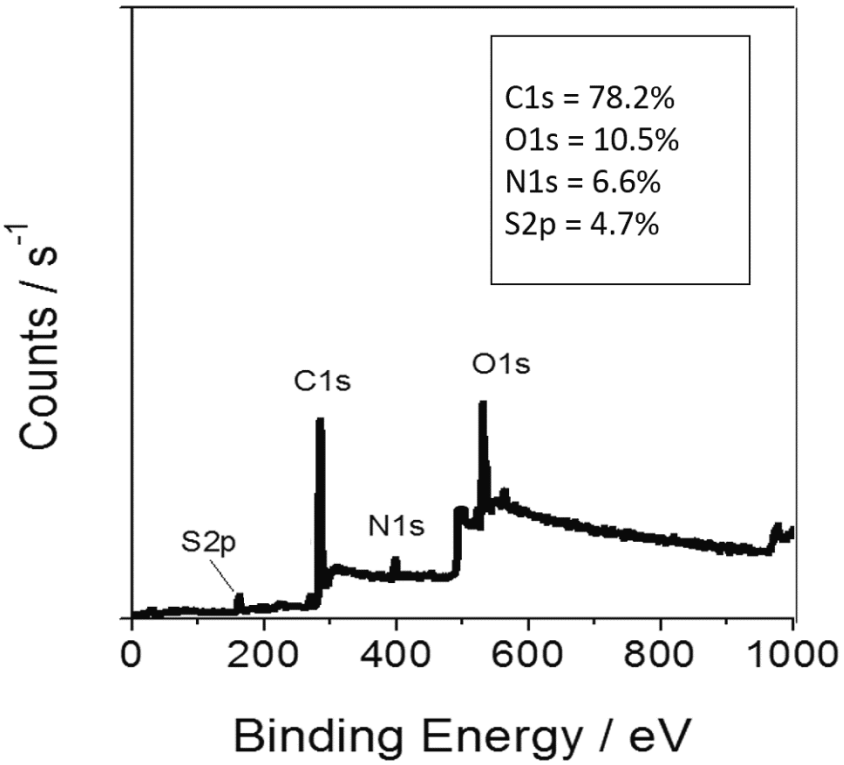

Figure S 4.1. Survey XPS Spectrum Analysis of N, S Co-Doped CNDs.

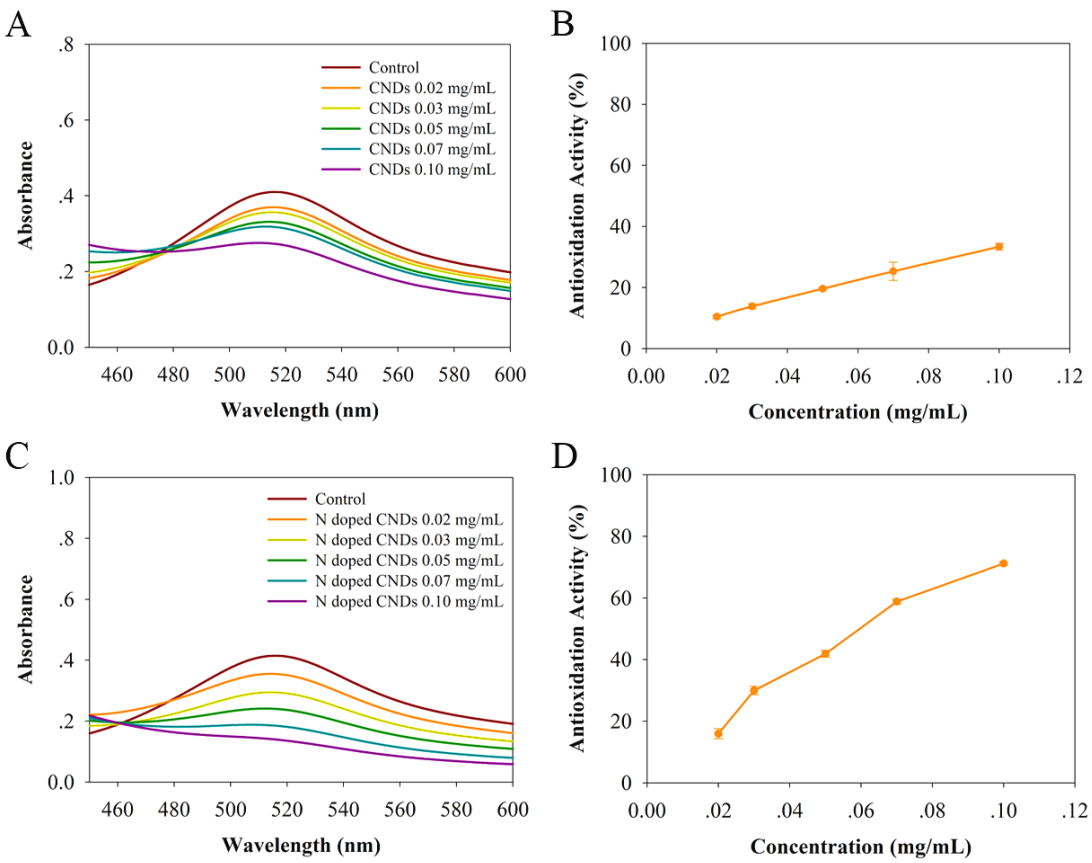

Figure S 4.2. Absorption Spectra and Calculated Antioxidation. (A) Absorption spectra of 0.02 mg/mL DPPH• methanol solutions with increasing the concentration of CNDs without N, S doping from 0 to 0.10 mg/mL measured after incubation for 2 hours under dark environment. (B) The calculated antioxidation activity versus the concentration of CNDs without N, S doping. (C) Absorption spectra of 0.02 mg/mL DPPH• methanol solutions with increasing N doped CNDs concentration from 0 to 0.10 mg/mL measured after incubation for 2 hours under dark environment. (D) The calculated antioxidation activity versus N doped CNDs concentration. Note that the synthesis processes are the same with that for the N, S co-doped CNDs except using different precursors: citric acid for CNDs without N, S doping and urea + citric acid for N doped CNDs.

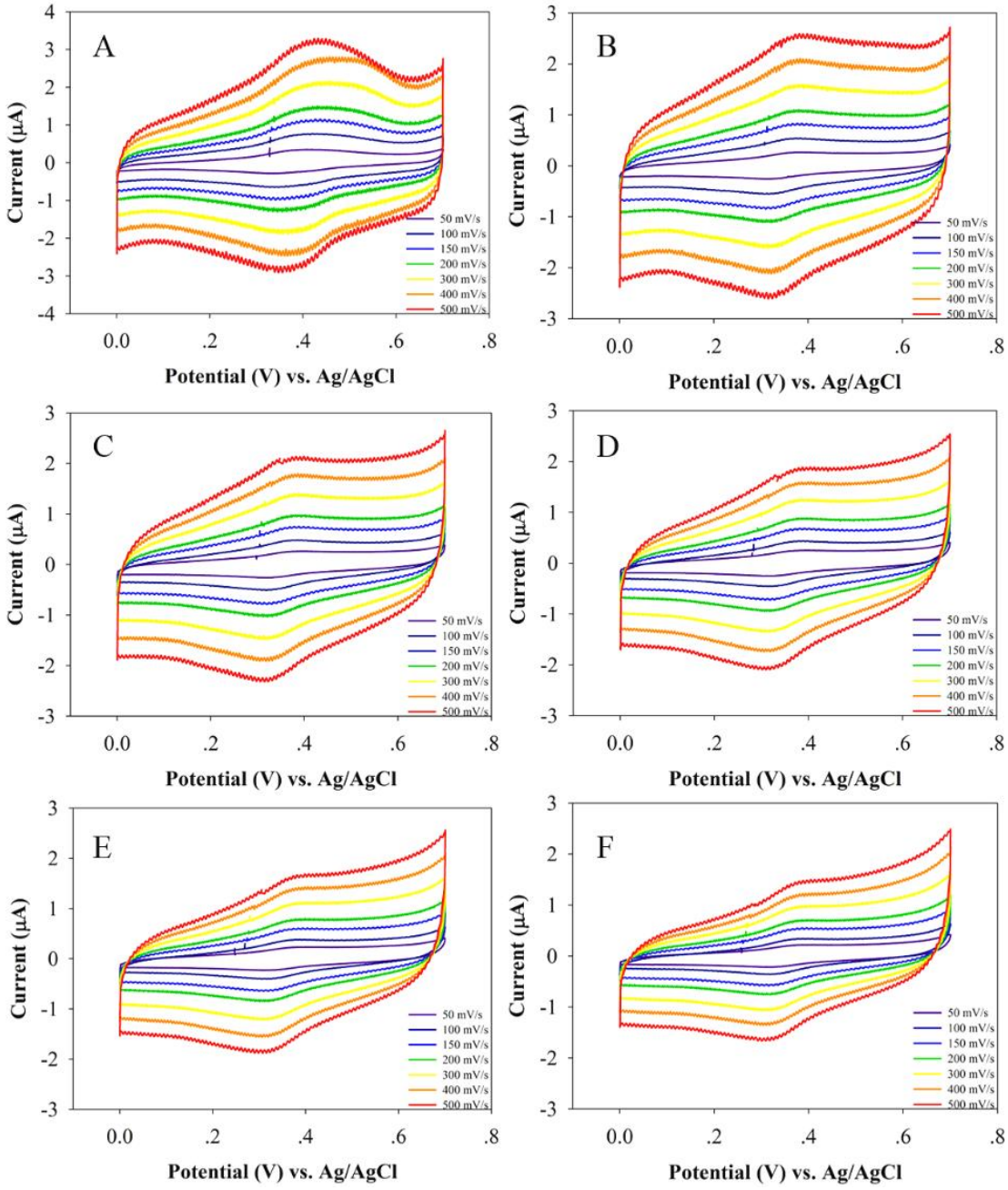

Figure S 4.3. Cyclic Voltammograms. The DPPH•-gold electrode system are shown as a function of scan rate (50, 100, 150, 200, 300, 400 and 500 mV/s scan rates) for different concentrations of N, S co-doped CNDs: 0.00 mg/mL (A), 0.02 mg/mL (B), 0.03 mg/mL (C), 0.05 mg/mL (D), 0.07 mg/mL (E), and 0.10 mg/mL (F).

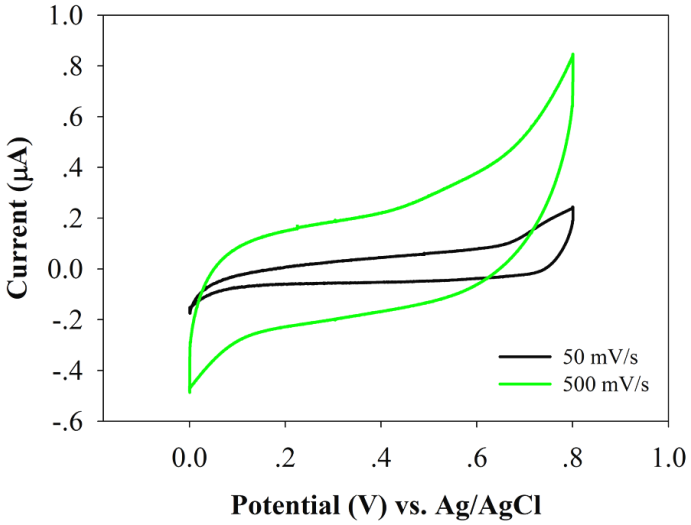

Figure S 4.4. Cyclic Voltammograms. The 0.05 mg/mL of N, S co-doped CNDs in a 5.0 mL methanolic phosphate buffer at scan rates of 50 and 500 mV/s (as a control without DPPH•).

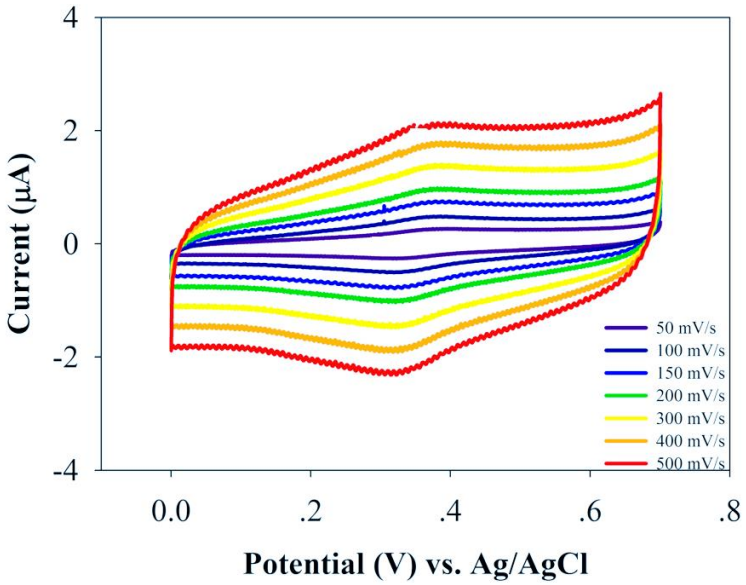

Figure S 4.5. Cyclic Voltammograms. The 0.01 mg/mL of DPPH• in a 5.0 mL methanolic phosphate buffer at scan rates of 50, 100, 150, 200, 300, 400 and 500 mV/s (as a control without CNDs incubation).

Table S 4.2. R-Squared Results for the Linearization

Concentration	Anodic/Cathodic	R^2
0.00 mg/mL	Anodic	0.9875
	Cathodic	0.9869
0.02 mg/mL	Anodic	0.9823
	Cathodic	0.9846
0.03 mg/mL	Anodic	0.9775
	Cathodic	0.9792
0.05 mg/mL	Anodic	0.9919
	Cathodic	0.9926
0.07 mg/mL	Anodic	0.9892
	Cathodic	0.9901
0.10 mg/mL	Anodic	0.9781
	Cathodic	0.9827

APPENDIX D

CNDS CELLULAR UPTAKE

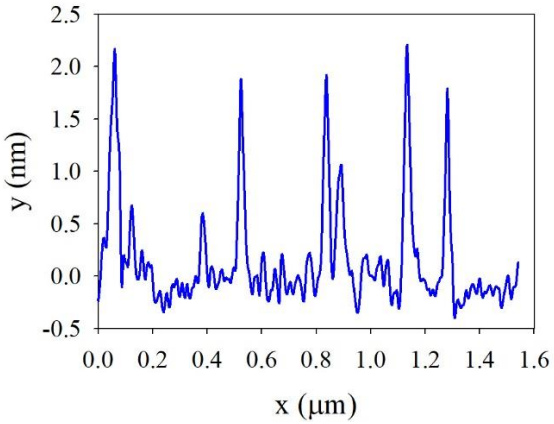

Figure S 5.1. A Representative Height Profile from The AFM Image.

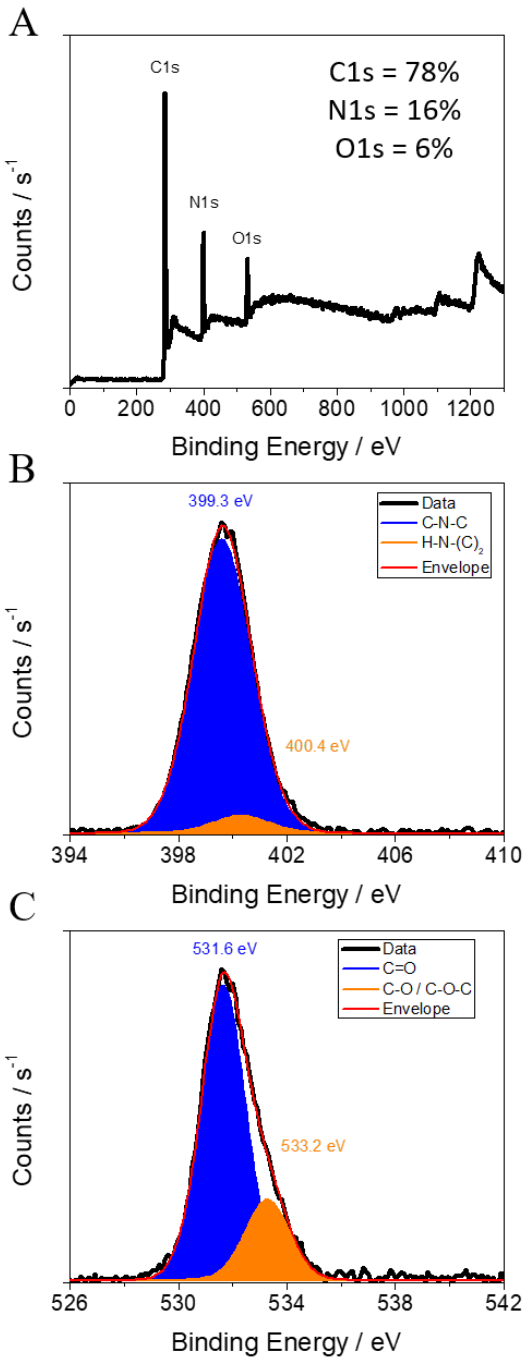

Figure S 5.2. Survey XPS Spectrum Analysis. (A) and XPS spectra of N 1s (B) and O 1s (C).

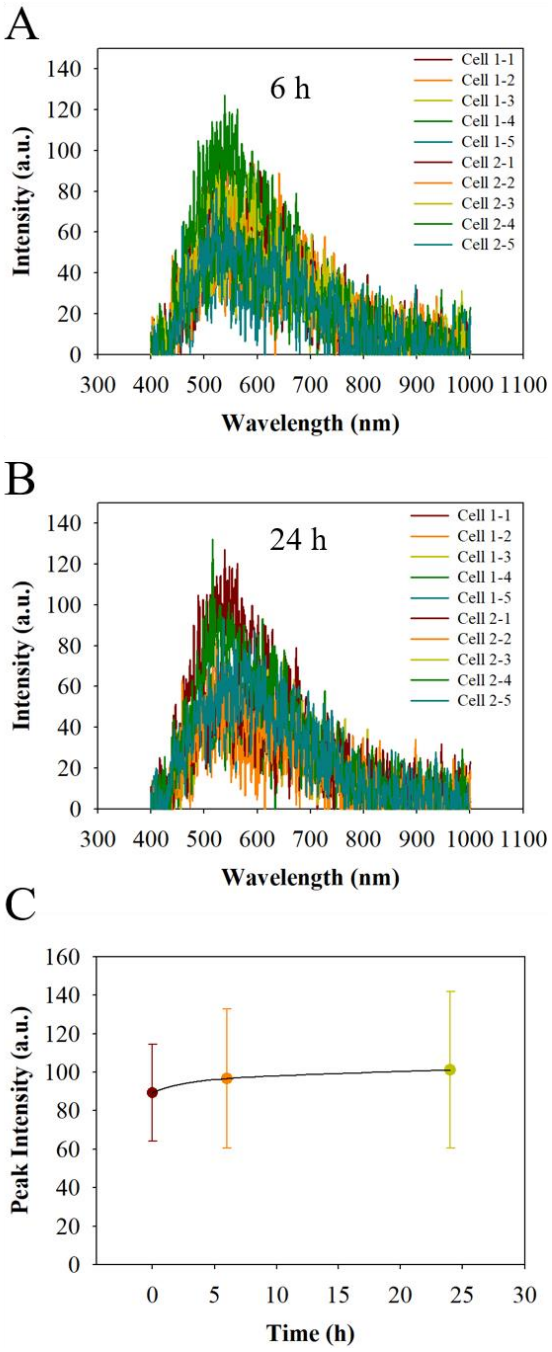

Figure S 5.3. Light Intensity Measurements of Cells. Cells measured without CNDs for different times: 6 h (A) and 24 h (B) and data analysis (C).